NTNU – Trondheim
Norwegian University of
Science and Technology

AC Induced Corrosion of Carbon Steel in 3.5wt% NaCl Electrolyte

Espen Oldeide Strandheim

Materials Science and Engineering	
Submission date:	June 2012
Supervisor:	Kemal Nisancioglu, IMTE
Co-supervisor:	Sven Morten Hesjevik, Statoil

Norwegian University of Science and Technology
Department of Materials Science and Engineering

Abstract

This paper deals with alternating current (AC) corrosion of low alloy carbon steel in 3.5 wt% NaCl electrolyte. Accelerated corrosion rates have been reported when exposed to AC and the corrosion mechanism is not well understood. Electrical heating of subsea pipelines, applied to avoid hydrate formation and waxing of multiphase hydrocarbon well streams has made this topic increasingly relevant in recent years. To study the effect of AC on corrosion rates, weight loss experiments under a wide range of experimental conditions were performed. The experiments may be divided into three categories: **1.** Weight loss experiments at open circuit with applied AC densities of 100, 250, 500 and 700 A/m^2 in combination with surveillance of i_{corr} on an hourly basis by the use of the linear polarization resistance (LPR) technique. Subsequent surface characterization by the use of a scanning electron microscope (SEM). **2.** Weight loss experiments at fixed potentials [-600, -800, -1000 and -1200 mV_{SCE}] with applied AC densities of 250, 500 and 700 A/m^2. Subsequent surface characterization by the use of SEM. **3.** Weight loss experiments using a rotating working electrode at open circuit with applied AC densities 100, 250, 500 and 700 A/m^2.

Results show that AC strongly influence corrosion kinetics of the system studied. Once AC is applied, a drop in corrosion potential and the formation of a passive iron oxide surface layer is observed. This layer is porous and believed to be the result of a rapid surface alkalization. Pitting corrosion is observed for all applied AC densities at open circuit. After an induction period of 10h, pit propagation initiates and the severity of pitting (measured in mass loss) increases with increasing levels of applied AC. Weight loss- and LPR measurements conform well and the use of this technique in the presence of AC is on this basis considered valid. Corrosion rates increase as applied level of AC is increased and an approximately linear relationship has been established between i_{AC} and i_{corr}. For samples polarized to -1200mV_{SCE} and subjected to $i_{AC} > 250A/m^2$, alkaline corrosion was observed. This is believed to be caused by the highly alkaline environment which develops when combining cathodic polarization with high AC densities. Under turbulent conditions, the system switches completely from mixed control to activation control for $i_{AC} > 250A/m^2$. The diffusion rate of oxygen towards the surface becomes too slow and hydrogen reduction becomes the dominating cathodic reaction.

Sammendrag (NO)

Denne rapporten omhandler vekselstrømskorrosjon (AC-korrosjon) av lavlegert karbonstål i 3.5 wt% NaCl elektrolytt. Akselererte korrosjonsrater har blitt rapportert under innflytelse av AC og korrosjonsmekanismen er ikke godt forstått. Elektrisk oppvarming av rør subsea for å unngå hydrat- og voksdannelse i rørstrømmer bestående av flerfase hydrokarbonblandinger har i de senere årene gjort dette temaet mer og mer relevant. For å studere effekten av AC på korrosjonsraten, ble flere ulike vekttapsforsøk utført. Eksperimentene kan deles i tre hovedkategorier: **1.** Vekttapsforsøk ved åpen krets med påtrykte AC strømtettheter 100, 250, 500 og 700 A/m^2 i kombinasjon med overvåkning av i_{corr} hver time ved bruk av lineær polarisasjonsmotstand-målinger (LPR). Påfølgende overflateundersøkelser utført i SEM. **2.** Vekttapsforsøk ved forhåndsbestemte potensialer [-600, -800, -1000 og -1200 mV_{SCE}] med påtrykte AC-strømtettheter 250, 500 og 700 A/m^2. Påfølgende overflateundersøkelser utført i SEM. **3.** Vekttapsforsøk med bruk av en roterende arbeidselektrode ved åpen krets med påtrykte AC-strømtettheter 100, 250, 500 og 700 A/m^2. Resultater fra forsøk gjør det klart at ved å påtrykke AC, blir korrosjonskinetikken i det aktuelle systemet betydelig påvirket. Umiddelbart etter påsats av AC faller korrosjonspotensialet og et passivt jernoksid dannes på overflaten av prøvene. Dette oksidet er porøst og antas å være resultatet av en hurtig overflate-alkalisering knyttet til fallet i korrosjonspotensiale. Gropkorrosjon ble observert for alle AC-strømtettheter ved åpen krets. Etter en induksjonsperiode på 10 timer, begynner gropene å propagere. Alvorligheten av korrosjonsangrepet (målt i vekttap) øker med økende størrelse på det påtrykte AC-signalet. Vekttaps- og LPR-målinger sammensvarer bra med hverandre og bruken av denne teknikken under påvirkning av AC regnes som gyldig. Korrosjonsrater øker med økende størrelse på det påtrykte AC-signalet og en tilnærmet lineær sammenheng har blitt påvist mellom i_{AC} og i_{corr}. For prøver som ble polarisert til -1200mV_{SCE} og utsatt for $i_{AC} > 250A/m^2$, ble alkalisk korrosjon observert. Det anntas at dette skyldes det sterkt alkaliske mijøet som utvikles ved å kombinere katodisk polarisering og høye AC-strømtettheter. Under turbulente forhold, skifter systemet fra blandet kontroll til å bli fullstendig aktiveringskontrollert for $i_{AC} > 250A/m^2$. Diffusjonsraten for oksygen mot overflaten blir for langsom og hydrogenreduksjon tar over som den dominerende katodiske reaksjonen.

Aknowledgements

The author would like to thank:

Supervisor **Kemal Nisancioglu** (K2, NTNU), co-supervisor **Sven Morten Hesjevik** (Statoil) and staff engineer **Kjell Røkke** (K2, NTNU) for guidance and helpful assistance throughout the project.

Contents

1 **Introduction** **1**

2 **Theory** **5**
- 2.1 Effect of AC on electrochemical properties of metals . . . 5
  - 2.1.1 AC frequency . . . 6
  - 2.1.2 Potential . . . 8
  - 2.1.3 Mathematically modelled polarization curves . . . 9
  - 2.1.4 Experimental polarization curves . . . 10
  - 2.1.5 Corrosion rate . . . 13
- 2.2 Corrosion mechanism . . . 14

3 **Experimental** **19**
- 3.1 Material specification . . . 19
- 3.2 Stationary working electrode . . . 20
  - 3.2.1 Sample geometry . . . 20
  - 3.2.2 Pre-treatment . . . 20
- 3.3 Rotating working electrode . . . 21
  - 3.3.1 Sample geometry . . . 21
  - 3.3.2 Pre-treatment . . . 21
- 3.4 Apparatus . . . 22
  - 3.4.1 Weight loss experiments (stationary working electrode) . . . 24
  - 3.4.2 Weight loss experiments (rotating working electrode) . . . 25
- 3.5 Test procedure . . . 27
  - 3.5.1 Weight loss experiments - stationary working electrode . . . 27
  - 3.5.2 Weight loss experiments - rotating working electrode . . . 30
- 3.6 Surface characterization . . . 31

4 **Results** **33**
- 4.1 Weight loss experiments - stationary WE at open circuit . . . 34
  - 4.1.1 Corrosion rate . . . 34
  - 4.1.2 Weight loss measurements . . . 35

4.1.3 LPR measurements 36
4.1.4 Time dependency of i_{corr} 38
4.1.5 Corrosion potential 38
4.1.6 Surface characterization 39
4.2 Weight loss experiments - stationary WE at fixed potentials 44
4.2.1 Corrosion rate 44
4.2.2 Surface characterization 45
4.3 Weight loss experiments - rotating WE 49
4.3.1 Corrosion current 49
4.4 Summary of results 51

5 Discussion 53
5.1 AC corrosion 53
5.2 Corrosion mechanism 54
5.2.1 Iron oxide surface layer 54
5.2.2 Corrosion current 54
5.2.3 Limiting current 58
5.2.4 Polarized working electrode 62

6 Conclusions 65

7 Further work 67

References 68

List of appendices 71

Appendix A Weight loss/ LPR - measurements A.1

Appendix B Surface characterization B.3

Appendix C Sources of error D.1
C.1 VariAC D.1
C.2 Electrolyte D.1
C.3 Electrode position D.2

Appendix D Previous Work D.1
D.1 Correction for IR-drop - polarization curves D.5

List of Figures

Figure 1.1 DEH system 2

Figure 2.1 CR vs. frequency 6
Figure 2.2 Superpositioning AC- onto DC-signal 8
Figure 2.3 E_{corr} vs. time 8
Figure 2.4 Simulated polarization curves 9
Figure 2.5 Polarization curves 1, I. Stamnes 10
Figure 2.6 Polarization curves 2, I. Stamnes 11
Figure 2.7 General corrosion kinetics under the influence of AC. 12
Figure 2.8 Theoretical impact of AC on polarization curves 13
Figure 2.9 CR vs. i_{AC}, I. Stamnes 13
Figure 2.10 Corrosion mechanism (NACE) 14
Figure 2.11 Potential/current characteristics (NACE) 15
Figure 2.12 Instant/cumulative metal loss (NACE) 15
Figure 2.13 CR vs. time 16
Figure 2.14 (a)Pourbaix (b) Pitting potential 17

Figure 3.1 Principal sketch - sample (stationary WE) 20
Figure 3.2 Principal sketch - sample (rotating WE) 21
Figure 3.3 Sample holder for pre treatment 22
Figure 3.4 Overview - weight loss setup 22
Figure 3.5 Basic circuit structure 23
Figure 3.6 Overview - setup 24
Figure 3.8 Overview - experiment cell 26
Figure 3.10 Gamry software - input window 27
Figure 3.11 Zeiss Ultra 55 limited edition (FESEM) 31

Figure 4.1 i_{AC} vs. CR 34
Figure 4.2 Measured added weight loss, ASTM G1-03, C.3.5 35
Figure 4.3 R_p vs time 36
Figure 4.4 Polarization curves - Stationary working electrode, E_{OC} 37
Figure 4.5 i_{corr} vs. time 38

Figure 4.6 E_{corr} vs time 39
Figure 4.7 Photos from experiments 40
Figure 4.8 SEM, $i_{AC} = 0, 100, 250$ and $500 A/m^2$ 41
Figure 4.9 SEM, $i_{AC} = 500 A/m^2$, oxide 42
Figure 4.10 Microanalysis (EDS) 43
Figure 4.11 E_x vs. CR. 44
Figure 4.15 SEM images (-1000 and -1200 mV_{SCE}) 48
Figure 4.16 i_{AC} vs. i_{corr}. Rotating WE 49
Figure 4.17 Polarization curves, 250 rpm 50

Figure 5.1 i_{AC} vs. i_{corr} - 2011 and 2012 54
Figure 5.2 Stages of pitting 57
Figure 5.3 i_{corr} vs. time 57
Figure 5.4 Polarization curve - Stationary working electrode, $i_{AC} = 700 A/m^2$ . . 59
Figure 5.5 Potential development 60
Figure 5.6 AC effect on polarization curves 61
Figure 5.7 Polarization stages 63

Figure A.1 R_p vs. time. A.2
Figure A.2 R_p vs. time. B.1

Figure B.1 SEM, $i_{AC} = 0 A/m^2$ B.4
Figure B.2 SEM, $i_{AC} = 100 A/m^2$ B.5
Figure B.3 SEM, $i_{AC} = 250 A/m^2$ B.6
Figure B.4 SEM, $i_{AC} = 500 A/m^2$ B.7
Figure B.5 SEM, $i_{AC} = 700 A/m^2$ B.8
Figure B.6 SEM, $i_{AC} = 250 A/m^2$ B.9
Figure B.7 SEM, $i_{AC} = 250 A/m^2$ B.10
Figure B.8 SEM, $i_{AC} = 500 A/m^2$ B.11
Figure B.9 SEM, $i_{AC} = 500 A/m^2$ B.12
Figure B.10 SEM, $i_{AC} = 700 A/m^2$ B.13
Figure B.11 SEM, $i_{AC} = 700 A/m^2$ B.14

Figure D.1 Measured i_{corr} and CR vs. i_{AC} - Weight Loss Experiments D.2
Figure D.2 Polarization curves, 250 rpm D.3
Figure D.3 Polarization curves, 500 rpm D.4
Figure D.4 Correction for IR-drop and i_{lim} D.5

List of Tables

Table 2.1 Cathodic Tafel slope reduction 11

Table 3.1 Composition of C-steel 19
Table 3.2 Dimensions - Weight loss experiment samples 20
Table 3.3 Dimensions - sample (rotating WE) 21
Table 3.4 Test matrix - Weight loss experiments at open circuit 29
Table 3.5 Test matrix - Weight loss experiments at fixed potentials 29
Table 3.6 Test matrix - Weight loss (rotating WE) 30

Table 4.1 Results - LPR and weight loss at open circuit 34
Table 4.2 Weight loss measurements 35
Table 4.3 Quantitative analysis (EDS) 43
Table 4.4 Results - weight loss under polarization 44
Table 4.5 Key values 49
Table 4.6 Polarization data, 250 rpm 50

Table 5.1 Regression analysis 58

Table A.1 Experiment data A.1

Table C.1 VariAC instability - stationary WE D.2
Table C.2 VariAC instability - rotating WE D.2

Table D.1 Results - Weight loss experiments D.2
Table D.2 Polarization data, 250 rpm D.3
Table D.3 Polarization data, 500 rpm D.4

Glossary

Abbreviations	
AC	Alternating Current
AV	Alternating Voltage
DC	Direct Current
RT	Room Temperature
CR	Corrosion Rate
CE	Counter Electrode
WE	Working Electrode
DEH	Direct Electrical Heating
SCE	Standard Calomel Electrode
FESEM	Field Emission Scanning Electron Microscope
EDS	Energy Dispersive X-ray Spectroscopy

Parameters		
Symbol	**Description**	**SI unit**
E_{OC}	Open circuit potential	[V]
E_{corr}	Corrosion potential	[V]
i_{AC}	Alternating current density	$[A/m^2]$
i_{corr}	Corrosion current density	$[A/m^2]$
i_{lim}	Limiting current density	$[A/m^2]$

Chapter 1

Introduction

Background

The offshore production of oil and gas on the Norwegian continental shelf, in most cases rely on subsea installations. Petroleum wells at these installations are either connected to neighboring platforms or onshore processing sites through pipelines. Well streams containing pure oil or pure gas are rarely encountered as they usually consist of a multiphase mixture of oil, gas and water. Flow assurance in these pipelines is an ongoing challenge in the oil and gas industry, especially in colder parts of the world. The well stream, depending on composition and pressure, keeps an elevated temperature. When production is shut down, which periodically happens due to maintenance or other operational interventions, conditions become stagnant and temperatures decrease. Under such circumstances there is a danger of clogging. Natural gas and water form hydrates and will solidify if the temperature falls below a certain level. Together with wax formation, this may restrict the flow inside the pipe. Once solidified, such clogs are difficult and potentially hazardous to remove.

DEH system

Traditionally, flow assurance has been kept by the use of chemicals like ethylene glycol (MEG) which depresses the temperature at which hydrates are formed. This is an effective but costly option and may offer a risk to the environment. In later years, direct electrical heating (DEH) has been looked towards as a valid alternative solution (illustrated in figure 1.1). Controlling the thermal conditions directly has proven effective as well as cost reducing. Alternating current (AC) is transferred through the pipe wall ensuring temperatures above the wax and hydrate formation temperature. This will cause transfer of electrical current from the pipe to the sea which in turn potentially may lead to a form of corrosion to the pipe exterior called AC corrosion. The mechanism of AC corrosion is not well understood, but corrosion rates are reported to increase, posing a threat to the pipeline integrity at coating holidays[1].

In Norwegian waters, multiple oil fields have been installed with DEH systems on their flow lines since 2000. Examples are Åsgard and Tyrihans for Statoil and the Skarv field for British Petroleum. Understanding the range of effects these systems may have on corrosion properties is important and the motivation behind this experimental work.

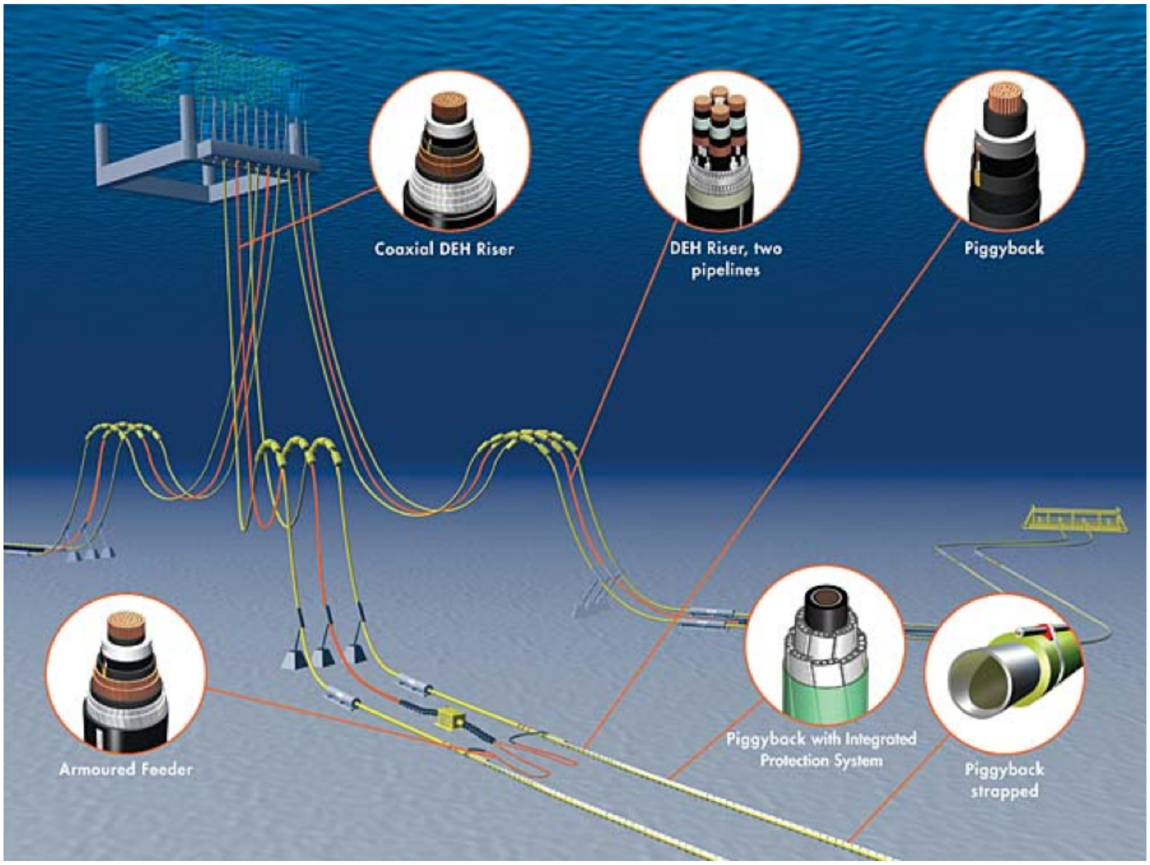
Coaxial DEH Riser
DEH Riser, two pipelines
Piggyback
Armoured Feeder
Piggyback with Integrated Protection System
Piggyback strapped

Figure 1.1: *Illustrative graphics from Nexans describing a typical DEH system. In this example the production unit is a semi submersible platform. A DEH riser cable supplies power from the platform and the "piggyback" cable conducts AC current in a loop to the pipeline destination and back. This cable is protected against potential harmful loads like fishing trawlers etc. through an integrated protection system [1].*

---

[1] Coating holiday: puncture/ discontinuity of protective coating.

Previous work

As a part of a research initiative within the corrosion group at the Institute of Materials Technology (IMT) at NTNU, a project work was initiated by the author [2] in the autumn of 2011. The purpose of this specialization project was to study the mechanism of AC corrosion in 3.5wt% NaCl electrolyte. Several experiments were performed on carbon steel under both stagnant and turbulent conditions at different levels of applied AC. Results from these experiments confirmed the pre-assumed correlation between applied AC density and the corrosion rate of the exposed carbon steel samples. As AC densities were increased above a threshold value of approximately $100A/m^2$ under stagnant conditions, measured corrosion rates increased significantly relative to the case at no AC. The effect of AC on parameters such as the Tafel slopes for both the cathodic and the anodic reactions, the limiting current for oxygen reduction, the corrosion current and the corrosion potential were evaluated. Results from this investigation are mentioned throughout this masters thesis while a collection of the most significant results are given in appendix D.

Aims/ scope of the work

This masters thesis is a continuation of the mentioned specialization project. It contains an electrochemical investigation of AC corrosion on low alloy carbon steel in 3.5wt% NaCl electrolyte. Weight loss experiments will be performed under a wide range of experimental conditions in an attempt to further understand the mechanism of AC corrosion.

To supplement results already obtained in previous work under stationary working electrode (WE) conditions, weight loss experiments at different levels of applied AC will be performed at open circuit. An in-PC Gamry potentiostat will be implemented into the circuit in an attempt to enable accurate linear polarization resistance (LPR) measurements. This will also enable the ability to record polarization curves. The weight loss measurements are performed to attain accurate corrosion rates based on the total time of exposure while LPR measurements will enable monitoring of the polarization resistance (R_p) on an hourly basis throughout the experiment. Being inversely proportional to the corrosion current via the Stern Geary equation, mapping of R_p may answer questions regarding the development of the corrosion rate during the experiment. Polarization data from potentiodynamic scans will be used to determine Tafel slopes necessary for calculation of such corrosion rates. Attention will be given to whether or not the LPR technique qualifies as a valid technique for monitoring corrosion kinetics under the influence of AC. Separate weight loss experiments where the working electrode is polarized to fixed potentials and exposed to different levels of AC will as well be performed. The main objective here is to investigate how cathodically protected carbon steel reacts when exposed to AC.

Weight loss experiments using a rotating working electrode setup are as well to be carried out to investigate the correlation between the corrosion current and the limiting current for oxygen reduction. This is done in light of the drastic effect high levels of AC has on polarization data and the apparent disappearance of the potential range where the limiting current for oxygen reduction is active.

In the analysis, results from experiments will be combined with surface characterization images captured by the use of a scanning electron microscope (SEM) in order to further understand the corrosion mechanism behind AC corrosion.

Thesis outline

Chapter 2 - Theory In this chapter a theoretical foundation which describes the known effects of AC on corrosion properties will be established. Articles considered relevant produced by published authors will be combined with the previous work performed within the Institute of Materials Technology at NTNU to establish such a foundation. Elementary electrochemistry will not be reviewed.

Chapter 3 - Experimental Thorough characterizations of equipment and methods used throughout the experimental stage of this thesis. Text and tables are combined with illustrative figures.

Chapter 4 - Results In this chapter, results from the experiments will be presented. Seeing as the performed experiments may be divided into different categories, one section will be devoted to each category.

Chapter 5 - Discussion The results will be analyzed and a corrosion mechanism will be proposed.

Chapter 6 - Conclusions The most important conclusions which could be made from the analysis will in short terms be presented.

Chapter 7 - Further Work In this chapter, the author will propose what should be further researched within the topic AC corrosion. This is based on observations made during the experiments, trends from the results as well as personal opinion.

Chapter 2

Theory

2.1 Effect of AC on electrochemical properties of metals

Application of alternating current (AC) into a direct current (DC) system changes the electrochemical properties of metals in ways that are not fully understood. Since the discovery of AC corrosion on land based pipelines subjected to stray alternating currents from crossing power lines more than half a decade ago, multiple studies have been performed in an attempt to explain and quantify the corrosion type. In general, corrosion rates are reported to increase in the presence of AC. These studies are though mainly focused on acidic and sulfate (soil) solutions and few studies have been performed on AC corrosion in a marine environment. The following sections contain a review of what literature is available relevant to the AC corrosion of low alloy carbon steel in a 3,5 wt% NaCl electrolyte[1].

---

[1] The salinity of seawater is on average 3,5% around the world. NaCl is the main component.

2.1.1 AC frequency

There is a strong correlation between the frequency of the applied AC signal and the resulting corrosion rate (CR) for metals in general. Pagano and Lalvani [3] conducted experiments in an attempt to map the behavior of the two parameters at different applied alternating voltages (AV)[2].

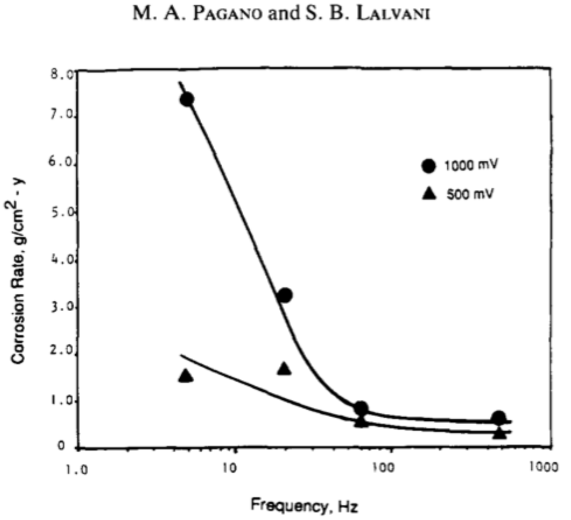

Figure 2.1: *Relationship between the CR of carbon steel and the frequency of applied AV signal for voltages of 1000mV and 500mV respectively. Experiments were carried out at room temperature (RT) in oxygen free artificial seawater. [3]*

Figure 2.1 depicts results achieved through these experiments on carbon steel. What their findings document is as frequencies increase, the corresponding CR decreases. At about 60 Hz and above, there is a stabilization of the CR.

In explaining this behavior, Pagano and Lalvani looks to the fact that at higher frequencies, the double layer impedance (Z_{Cdl}) decrease according to equation 2.2. This results in only small fractions of current flowing through the polarization resistance since most of the current is spent recharging the double layer. Hence, material degradation will be limited. At lower frequencies the situation is the opposite and Z_{Cdl} is high relative to the previous case. In other words; at high levels of frequency ($\geq$ 60 Hz), the CR gradually becomes less dependent of applied AV magnitude and its effect becomes negligible.

---

[2] "AC" and "AV" are both abbreviations used regularly throughout this report. Which one is used in each situation depends upon the practicality of context (ref. Ohms Law, equation 2.1).

$$U = R \cdot I \tag{2.1}$$

$$Z_{Cdl} = \frac{1}{2\pi \cdot f \cdot C} \tag{2.2}$$

Fernandez et al. [4] further explains this behavior through experiments with alternating frequencies of the applied AC density. The corrosion process is, as figure 2.2 illustrates, divided into anodic and cathodic half-cycles due to the sinusoidal voltage. The potential will alternate according to equation 2.3 where E is the potential at any moment and E_{corr} is the corrosion potential [5],

$$\Delta E = E - E_{corr} \tag{2.3}$$

Then we have,

$$\Delta E = \Delta E_0 \sin \omega t \tag{2.4}$$

Where ω is the angular frequency and t is the time. Under somewhat simplified conditions where the anodic reactions are $Fe \rightarrow Fe^{2+} + 2e^-$ and $Fe^{2+} \rightarrow Fe^{3+} + e^-$ and the cathodic reaction is dominated by hydrogen evolution $2H^+ + 2e^- \rightarrow H_2$, the authors documented the following behavior from their experiments. At lower frequencies the metal dissolution is more effective than at higher ones. In the anodic half-cycles the cathodic reaction is less likely to happen due to potential considerations. Vice Versa, in the cathodic half-cycles, hydrogen evolution is more likely than metal dissolution. When the AC frequency increases, the interval between anodic and cathodic half cycles becomes smaller. As these time intervals decrease, the metal ions generated in anodic cycles are available for immediate redeposition in the subsequent cathodic cycles. Hence, less metal will dissolve. Furthermore, at these high frequencies, the hydrogen atoms generated in cathodic cycles will not have enough time to form hydrogen gas. So for the subsequent anodic cycle, a layer of hydrogen atoms will be located on the electrode surface. This is believed, at least to some extent, to inhibit metal dissolution from happening, promoting hydrogen ionization in its place. At very high frequencies, the authors coincides with Pagano and Lalvani, stating that more or less all current would pass via the double layer.

2.1.2 Potential

The superpositioning of an AC-signal onto a DC-signal leads to a resultant signal which alternates in anodic and cathodic half cycles relative to the initial DC potential. An illustration of this is given in figure 2.2. This behavior is well documented and the cause of electrochemical complications for metals exposed. [3, 6]

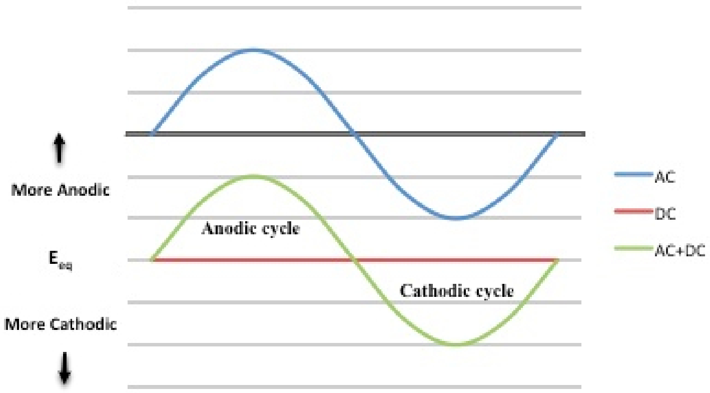

Figure 2.2: *A principal sketch of the superpositioning of an AC voltage onto a DC voltage. The resultant (AC+ DC) alternates between more anodic/more cathodic potentials relative to the initial DC voltage.*

When exposed to AC in 3,5wt% NaCl electrolytes, a general lowering of E_{corr} for carbon steel has been reported in multiple studies [3, 6, 7, 8, 9, 10]. Figure 2.3 illustrates this. An initial potential drop immediately after AC is applied followed by a stabilization towards less negative values, though still cathodic relative to the potential registered at no AC.

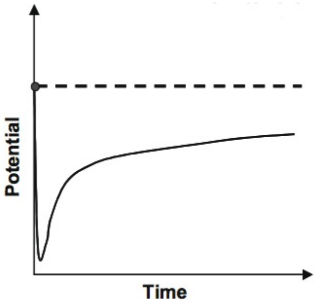

Figure 2.3: *Potential trend for carbon steel in 3,5% NaCl electrolyte under the influence of AC. Documented by Goidanich et al. [8]. Dotted line represents E_{corr} before AC is applied.*

2.1.3 Mathematically modelled polarization curves

Bosch and Bogaerts [11] attempted to model the effects of AC on polarization curves mathematically. More specifically, they looked at the behavior of corrosion kinetics for different Tafel parameter values at different applied AV magnitudes. Figure 2.4 presents simulated Tafel plots for three different cases from their investigation. The ratio $r = \frac{b_a}{b_c}$ between the anodic and cathodic Tafel parameters plays a significant role in their analysis. The following relations were determined to be true when AC was applied:

$r < 1$, E_{corr} will decrease.

$r = 1$, E_{corr} will be left unchanged.

$r > 1$, E_{corr} will increase.

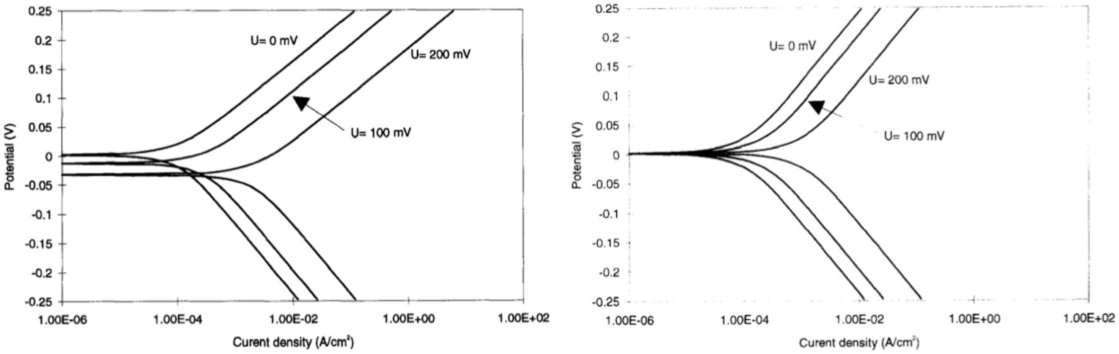

(a) $b_a = 60mV/dec, b_c = 120mV/dec$ (b) $b_a = 120mV/dec, b_c = 120mV/dec$

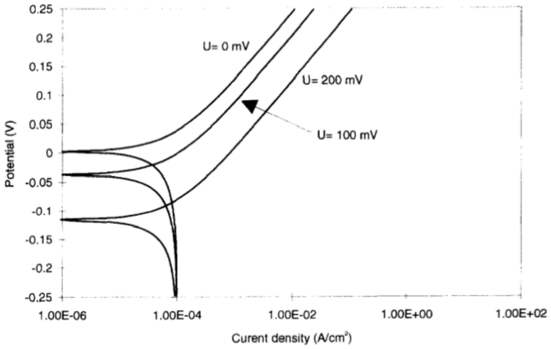

(c) $b_a = 40mV/dec, b_c \rightarrow \infty mV/dec$

Figure 2.4: *Simulated polarization curves for three different cases. (a) $r < 1$, (b) $r = 1$, (c) $r \rightarrow 0$*

In the case of carbon steel ($r < 1$) a decline in E_{corr} is expected. Figure 2.4(a) illustrates a polarization curve similar to what one would expect for carbon steel in an oxygen free environment (activation control). With increasing applied AV amplitudes, E_{corr} shifts to a more negative region. An increase of i_{corr} is also to be expected. Figure 2.4(b) depicts a case where the two Tafel slopes are equal ($r = 1$). Here the applied AV does not influence E_{corr}, only i_{corr} which increases. Finally, in figure 2.4(c) the cathodic reaction is completely under diffusion control, hence $b_c \rightarrow \infty$ ($r < 1$). Under these circumstances there is a negative shift in E_{corr} but no change of i_{corr}. The magnitude of the shift in potential is determined by the ratio between i_{corr} and i_{lim} (ΔE increases when $i_{corr} \rightarrow i_{lim}$).

Figure 2.4 gives valuable insight on the modeled effect applied AC will have on polarization curves, but these are simplified and simulated cases were experiment trends are easily inserted. In the end, the anodic and cathodic reactions are what decides the value of E_{corr} and i_{corr}. Intuitively, the rate at which these reactions increase or decrease will affect such parameters. In the above mentioned model, it is assumed that Tafel slopes are not affected by applied AC. This may be an oversimplification.

2.1.4 Experimental polarization curves

Stamnes [6] conducted polarization experiments on carbon steel in a 3.5wt% NaCl electrolyte. Results from these experiments are given in figure 2.5.

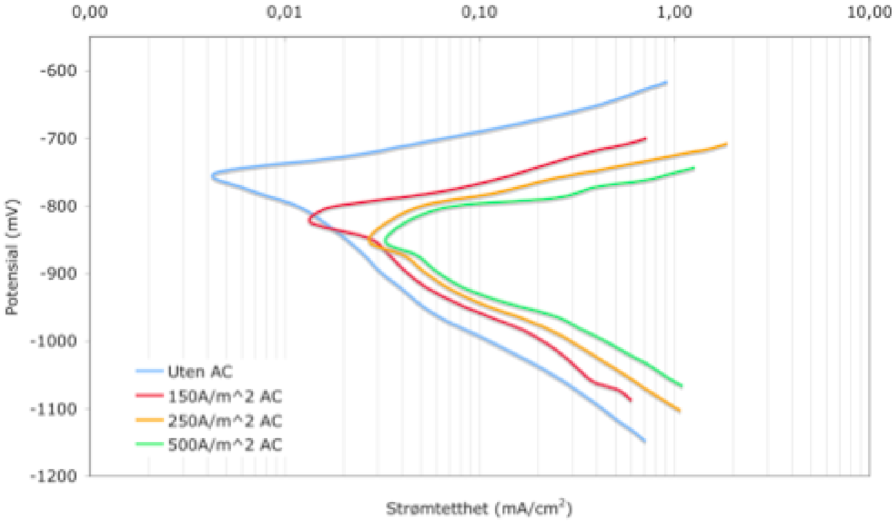

Figure 2.5: *Polarization curves, I. Stamnes. The electrolyte was 3.5wt% NaCl purged with N_2 gas, eliminating the oxygen contribution to the cathodic reaction. Working electrode was rotated at 500rpm.*

If these results are to be rated according to the mathematical model from the previous section, a drop in E_{corr} and an increase in i_{corr} would be expected as i_{AC} increases ($r < 1$). The results are in good accordance with these criteria. What is also visible from figure 2.5 is a reduction of cathodic Tafel slope, in this case solely including hydrogen reduction.

This contradicts the same model.

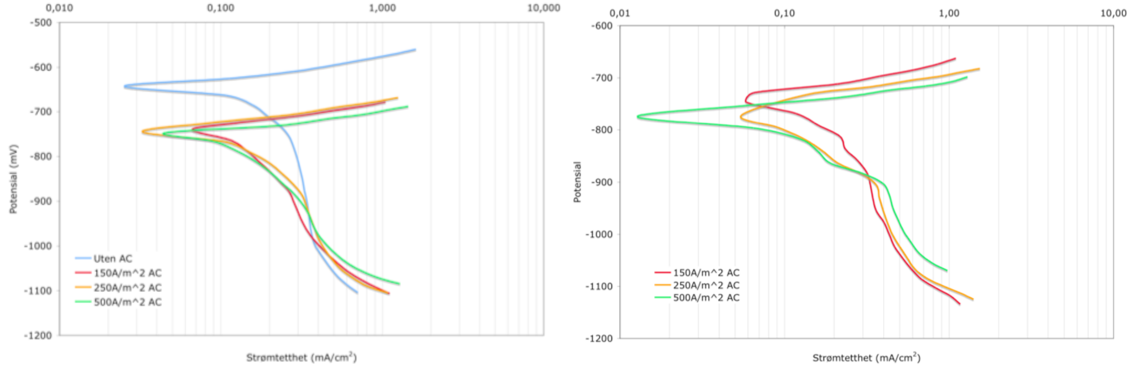

(a) 3.5wt% NaCl electrolyte purged with air, 500rpm, potential stabilized before application of AC.

(b) 3.5wt% NaCl electrolyte purged with air, 500rpm, no potential stabilization before application of AC.

Figure 2.6: *Polarization curves under various conditions.*

Figure 2.6 illustrates another two cases from the same study. In 2.6(a), the electrolyte is purged with air enabling oxygen reduction to contribute to the cathodic reaction. The Tafel slope for hydrogen reduction, also here, decrease significantly. After correction for IR-drop and i_{lim}, these Tafel slopes differ from 120 mV/dec at $i_{AC} = 0A/m^2$ to 80 mV/dec at $i_{AC} = 500A/m^2$. Furthermore, Stamnes observed that the hydrogen reduction becomes the dominating cathodic reaction again at roughly the same potential value for all i_{AC}. As a consequence, since E_{corr} decreases, the span at which i_{lim} is active becomes smaller. This has also been documented in a study performed by Hesjevik at Statoil, Rotvoll [9]. The same study resulted in values given in table 2.1 further illustrating the effect AC has on Tafel slopes.

Table 2.1: *Cathodic Tafel slope reduction for low alloy carbon steel and super martensitic stainless steel. Values were corrected for IR drop and adjusted to represent only the hydrogen reduction. Experiments were carried out in a 3,5wt% NaCl electrolyte purged with air. A rotating electrode setup tuned at 500 rpm constituted the working electrode. Pt counter electrodes were used.*

AC influence on cathodic Tafel slope		
i_{AC} $[A/m^2]$	C-steel, $\lvert b_c \rvert$ $[mV/dec]$	SMSS, $\lvert b_c \rvert$ $[mV/dec]$
0	**183**	112
500	**82**	106

It is further suggested that induced AC may give an added work to the reversible potential (E_{rev}) of the hydrogen reduction. The proposed adjusted value is given in equation 2.5.

$$E^{rev} = -\frac{RT}{nF}\ln a^2_{H+} + \frac{W_{AC}}{nF} \tag{2.5}$$

The added work (W_{AC}) is believed to increase the reversible potential to a more positive region, illustrated in figure 2.8.

Figure 2.7 shows results of experiments conducted by Goidanich et. al. [8] on, among others, carbon steel. Previously mentioned effects on E_{corr}, i_{corr} and β_c are observed also here. The anodic Tafel slope β_a however, shows an oscillating behavior between the different AC densities. This behavior is not expected and contradicts mathematical models [11].

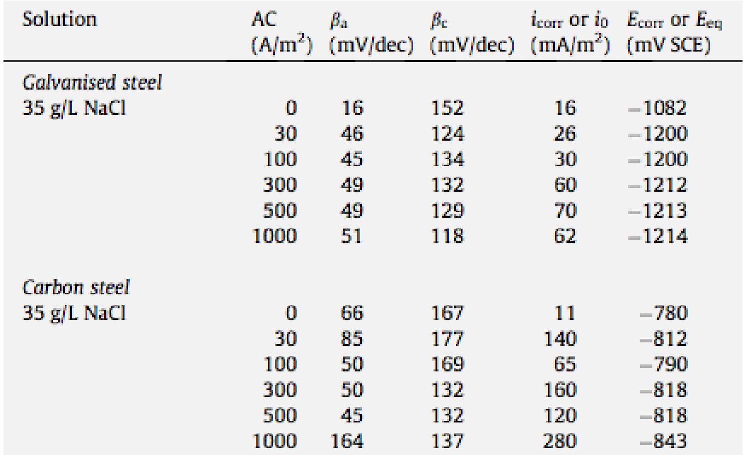

Solution	AC (A/m^2)	β_a (mV/dec)	β_c (mV/dec)	i_{corr} or i_0 (mA/m^2)	E_{corr} or E_{eq} (mV SCE)
Galvanised steel					
35 g/L NaCl	0	16	152	16	−1082
	30	46	124	26	−1200
	100	45	134	30	−1200
	300	49	132	60	−1212
	500	49	129	70	−1213
	1000	51	118	62	−1214
Carbon steel					
35 g/L NaCl	0	66	167	11	−780
	30	85	177	140	−812
	100	50	169	65	−790
	300	50	132	160	−818
	500	45	132	120	−818
	1000	164	137	280	−843

Figure 2.7: *Tafel slopes, corrosion potentials/ currents under the influence of AC [8]. Parameters extracted from polarization curves. Experiments were performed under oxygen free conditions at RT.*

Figure 2.8 graphically summarizes mentioned effects AC has on corrosion kinetics of carbon steel in a 3,5wt% NaCl electrolyte. 2.8(a) shows how a fluctuation in the anodic Tafel slope will impact corrosion parameters (in this case, a decreased b_a). A substantial increase in i_{corr} is visible and is amplified by the suggested added work on E^{rev}_{red}.

2.8(b) illustrates the significance of a decrease in the cathodic Tafel slope. Corrosion current densities are further increased.

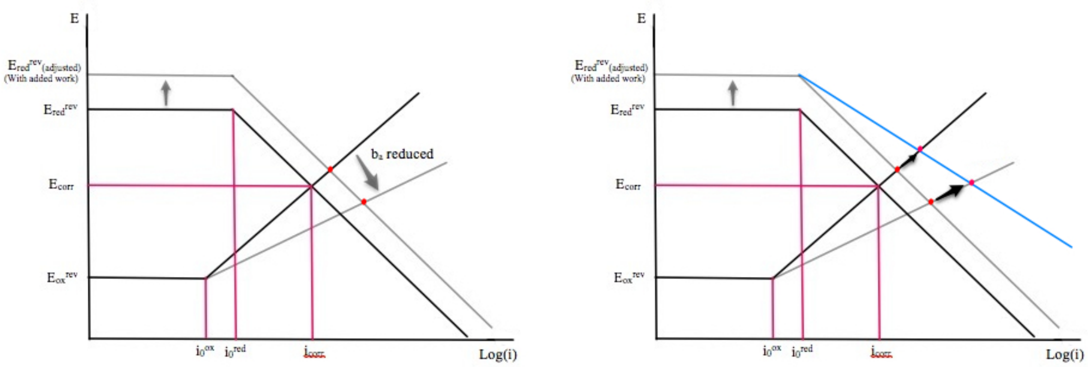
E
Ered rev (adjusted)
(With added work)
Ered rev
Ecorr
Eox rev
i0 ox
i0 red
icorr
Log(i)
ba reduced
E
Ered rev (adjusted)
(With added work)
Ered rev
Ecorr
Eox rev
i0 ox
i0 red
icorr
Log(i)

(a) Effect of reduced anodic Tafel slope b_a and increased reversible potential of hydrogen reduction on E_{corr} and i_{corr}.

(b) Added effect of reduced cathodic Tafel slope, b_c.

Figure 2.8: *Theoretical impact of AC on polarization curves based on trends seen in mentioned studies. In this case the electrolyte is Oxygen free, making Hydrogen reduction the cathodic reaction.*

2.1.5 Corrosion rate

Corrosion rates (CR) are reported to increase in the presence of AC as discussed in previous sections. I. Stamnes [6] conducted weight loss experiments with applied AC in an attempt to quantify this trend. The results of these experiments are given in figure 2.9.

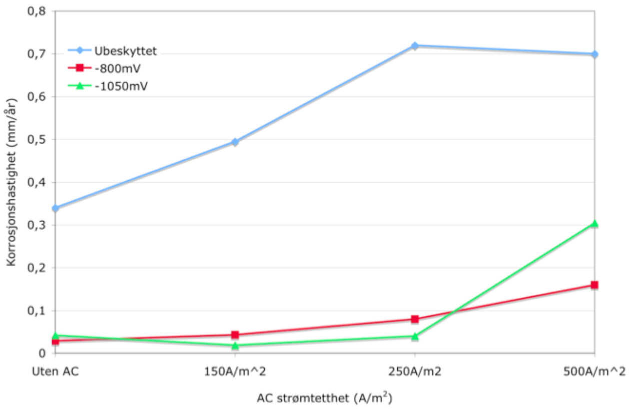

Figure 2.9: *CR vs.* i_{AC}*. A 3.5wt% NaCl electrolyte, constantly stirred, was used. Carbon steel type X65 was the test material. The blue line represents unprotected samples exposed for 24h. Red and green lines represent polarized samples exposed for 48h. CR given in [mmy].*

A significant increase in CR for the unprotected sample is visible. At $i_{AC} = 250A/m^2$ and above, the increasing trend stagnates and the CR stabilize.

2.2 Corrosion mechanism

A recent publication by NACE International on AC corrosion, includes a proposed explanation for the behavior of metals in the presence of AC. This proposal was a result of modeling and laboratory work. It is argued in this publication that only small amounts of the total applied AC discharge passes through the resistive component in a circuit equivalent to what one would find in the field. The AC passing through this resistive component will produce both anodic and cathodic polarization shifts.

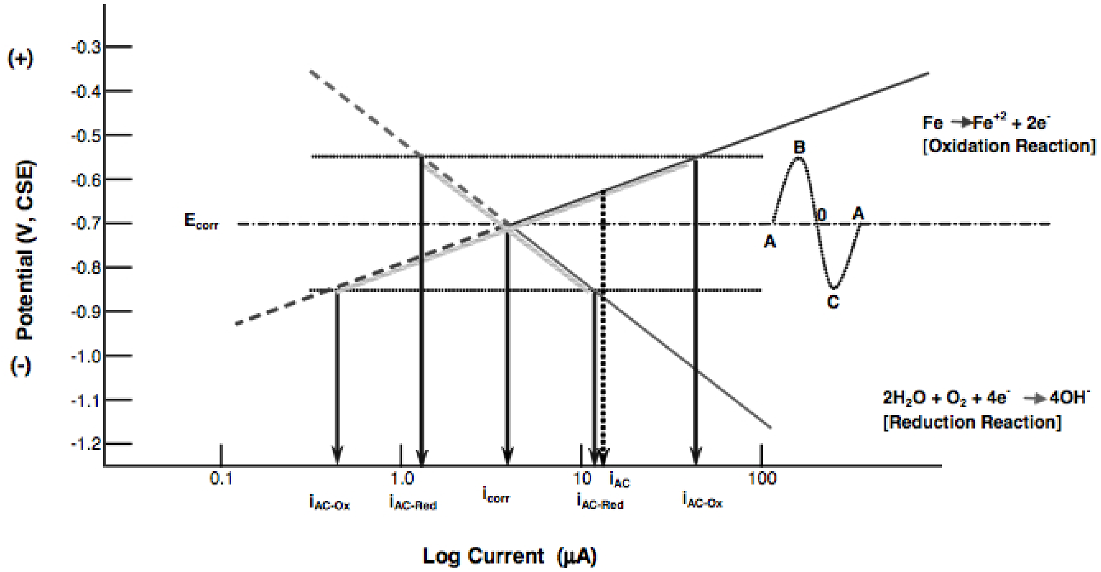

Figure 2.10: *Suggested corrosion mechanism for AC corrosion. NACE state-of-the-art [12]*

Figure 2.10 illustrates a simplified situation where the only available cathodic reaction is the conventional oxygen-water reduction and the only available anodic reaction is oxidation of iron. The AC signal has a frequency of 60Hz and the absolute value of the potential shift is 150 mV (sine wave A-B-0-C-A in figure 2.10). Since the relationship between the potential and current is semi-logarithmic, the anodic potentials (E_a) may be approximated by the equation: $E_a = \beta log i_a + b$, where β is the anodic Tafel slope and i_a is the anodic reaction current. It is further reasoned that during an anodic cycle of the sine wave (A-B-0), the anodic reaction current will increase to the value i_{AC-ox} on the right hand side in the graph. During the cathodic cycle (0-C-A) this current will decrease to the value i_{AC-ox} on the left hand side. Due to the mentioned semi-logarithmic dependence between potential and current, the average value of the anodic current for one AC sine wave period (denoted i_{AC} in graph) will be greater than i_{corr} for a freely corroding sample.

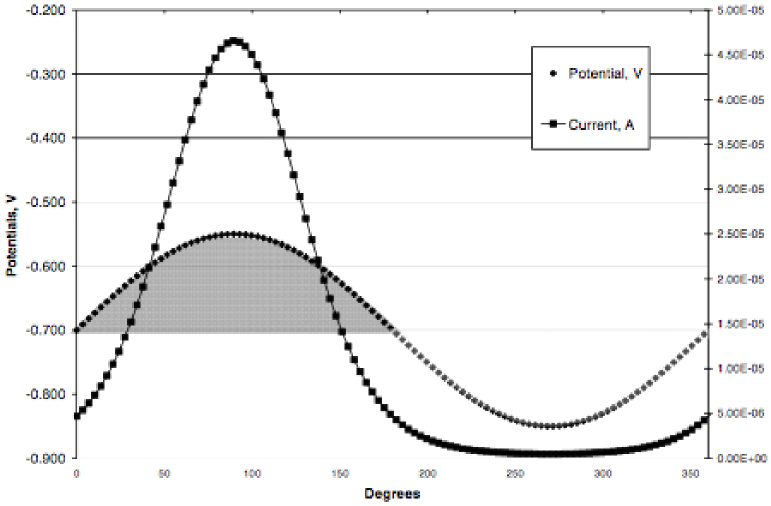

Figure 2.11: *Sinusoidal potential/ current characteristics. NACE state-of-the-art [12]*

Figure 2.11 illustrates the change in E_{AC} during one period of a sine wave. The resultant anodic oxidation current for this period is considerably larger during the anodic half cycle relative to the cathodic cycle. During the cathodic cycle, the current still decreases compared to the free corrosion current but it does not match the magnitude at which it increases during the anodic cycle. This is in line with the reasoning made in figure 2.10. The authors conclude with a net increase of the oxidation current during one AC period. Figure 2.12 sums up the effects this has in terms of metal loss.

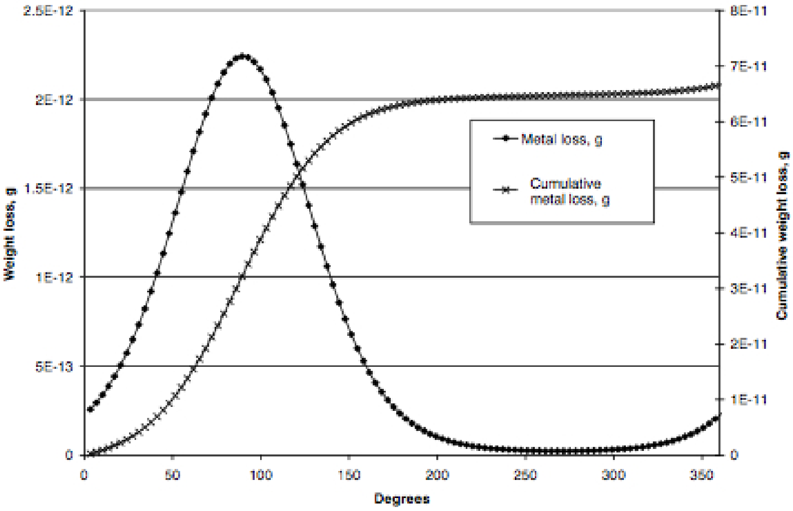

Figure 2.12: *Instant and cumulative metal loss during a single period. NACE state-of-the-art [12]*

Studies performed on carbon steel in seawater salinity solutions (and chloride containing solutions in general) [6, 13, 14, 15, 10] report the development of pits in the presence of AC. The formation of a porous passive oxide layer with no good protective properties is suggested to be the detrimental reason. Lalvani and Zhang [13, 14] conducted experiments in a 3,5wt% NaCl solution purged with nitrogen at different applied sinusoidal AV signals super positioned at fixed potentials. Results indicated an increase in corrosion rates with time.

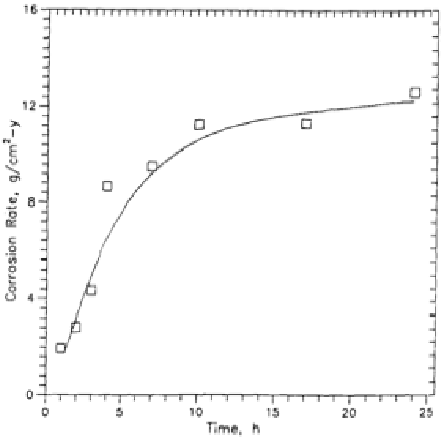

Figure 2.13: *CR vs. time. DC potential of specimen was held at -580m*V_{SCE} *while an AV signal at 60Hz with peak potential at 180m*V_{SCE} *was applied [13].*

According to figure 2.13, a sudden increase in the CR is followed by a stabilization as time passes. The authors explain the observed behavior by the auto-catalytic nature of pits. Inside a defect in the mentioned passive oxide layer, somewhat separated from the bulk solution, there will be an excess concentration of positive charge due to metal dissolution ($Fe \rightarrow Fe^{2+} + 2e^{-}$). Negatively charged chloride ions (Cl^{-}) will migrate into the defect to maintain electroneutrality. Metal ions and chloride ions will combine, resulting in large quantities of $FeCl_2$. Through hydrolysis, a high concentration of H^{+} ions will be present as well. Through aggressive Cl^{-} and H^{+} ions, an acidic environment develops. Locally in this defect, the CR will be high and a self propagating pit will be formed. Initially, the CR will be high. As corrosion products deposits on the surface, ion migration will be limited and the CR stabilizes. Had the electrolyte in the above mentioned case included large amounts of oxygen, it may be argued that this would contribute to the maintenance of electroneutrality, reducing the severity of the pitting.

The porous passive oxide layer formed in the presence of AC is suggested by I. Stamnes [6] to be magnetite (Fe_3O_4). Figure 2.14(a) shows a Pourbaix diagram for Fe. In order to achieve passivation and thereby the formation of a passive oxide layer, high values of PH are necessary. It is therefore suggested by Stamnes that the application of AC may lead to an immediate alkalization of the steel surface.

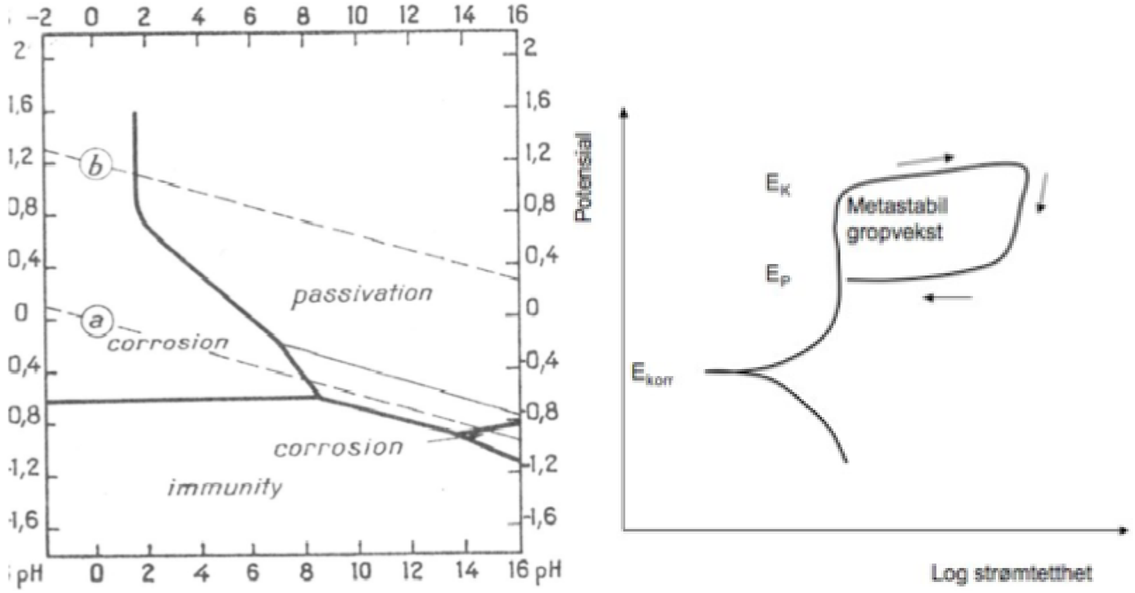

(a) Simplified Pourbaix diagram for Fe.

(b) Polarization curve illustrating the process of pitting. E_K is the critical potential for pitting. E_P is the passivation potential. Potential along the y-axis and current density along the x-axis.

Figure 2.14: *(a) Pourbaix. (b) Pitting potential. The potential values on the y-axis in figures are not equal and should not be compared. Figures from I. Stamnes [6].*

The potential drop experienced in the presence of AC (figure 2.3) is believed to further explain the mentioned effects. An activation of the steel surface when AC is applied followed by a gradual passivation by the formation of an oxide layer is suggested to explain this potential-trend. The activation of the surface is suggested to be caused by pitting. The potential will alternate between anodic and cathodic potentials and is believed to be well within the area of metastable pitting in anodic half cycles (figure 2.14(b)).

Chapter 3

Experimental

This chapter contains thorough characterizations of test equipment and experiment procedures. Two different working electrode (WE) geometries were utilized in the experiments (stationary WE: rectangular geometry, rotating WE: cylindrical geometry). These will be described initially in sections 3.2 and 3.3. In subsequent sections, the apparatus and the different test procedures will be described in detail.

3.1 Material specification

The material used for all experiments was micro alloyed carbon steel. The chemical composition is given in table 3.1[1].

Table 3.1: *Chemical composition of the carbon steel used throughout the experiments*

Chemical composition			
C [wt%]	Mn [wt%]	V [wt%]	Ti [wt%]
0.0108	0.2540	0.0029	0.0007

The steel is of similar quality as X65 grade pipeline steel. Its microstructure is ferritic/pearlitic and its main alloying element beside carbon is manganese. Low weight fractions of vanadium and titanium are present for added toughness. The yield strength is roughly 420 Mpa. Due to its low carbon content, this steel grade is often the preferred material for applications demanding high weldability.

---

[1] Composition was determined in an earlier project [10] by optical emission spectroscopy at Statoil - Rotvoll

3.2 Stationary working electrode

3.2.1 Sample geometry

The samples used in experiments requiring a stationary working electrode were all rectangular with dimensions given in table 3.2. An exposed area of 6.5 cm^2 was used for all experiments except those above $i_{AC} = 500A/m^2$. Due to limited effect from the variAC, the exposed area of samples tested above this value needed to be smaller. Resulting dimensions are given in table 3.2.

Table 3.2: *Dimensions of samples. Stationary working electrode.*

	Dimensions		
Parameter	Height [cm]	Width [cm]	Thickness [cm]
Sample	8	2	0.2
$A_{exposed=6.5cm^2}$ ($i_{AC} \leq 500A/m^2$)	1.4	2	0.2
$A_{exposed=5.7cm^2}$ ($i_{AC} > 500A/m^2$)	1.2	2	0.2

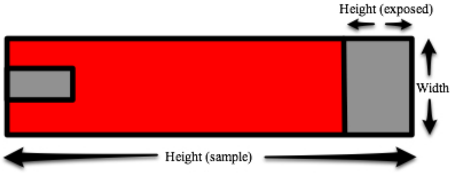

Figure 3.1: *Geometry of test samples. The area without paint on the left hand side in the picture ensured electrical conduction between sample and setup.*

3.2.2 Pre-treatment

The samples were given a finish of roughly 1000 grit using a standard grinding table with supplementary SiC papers (220, 500, 1000 grit, in that order). During this procedure, all edges were smoothened to avoid large current distribution discrepancies during experiment. Samples were then rinsed with distilled water, acetone and ethanol. A blow dryer was utilized to dry the samples. Standard masking tape was used in preparation for the subsequent coating. The coating applied was "Microshield - Stop-off lacquer". This is a type of acid-proof coating often used in laboratory experiments due to its favorable properties with respect to adhesion, curing time, and the fact that it is reasonably easy to remove when needed. Figure 3.1 illustrates a sample upon completion of mentioned steps.

3.3 Rotating working electrode

3.3.1 Sample geometry

In order to fit the rotating working electrode assembly, the samples needed to be cylindrical with a machined hole in the middle. Dimensions are given in table 3.3. Figure 3.2 illustrates the general geometry of the samples. The exposed area was 3 cm^2.

Table 3.3: *Dimensions of test samples. Rotating working electrode.*

	Dimensions			
Parameter	Height [cm]	R_i [cm]	R_o [cm]	$A_{exposed}$ [cm^2]
Sample	0.8	0.3	0.6	3.0

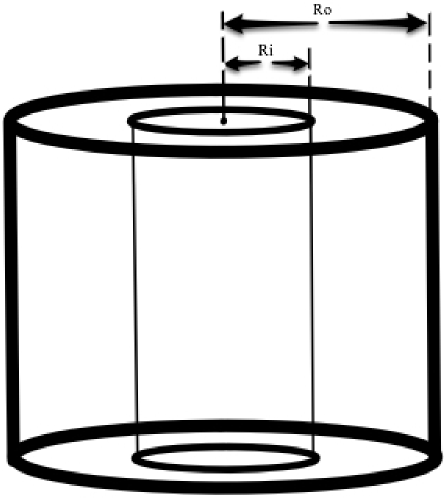

Figure 3.2: *Geometry of test samples. Rotating working electrode.*

3.3.2 Pre-treatment

The samples were, also in this case, given a finish of 1000 grit. This was achieved by using a custom built sample holder, illustrated in figure 3.3, attatched to a regular household drill bit. While grinding, samples were kept immersed in water. Seeing as the surface profile was already relatively fine, it was possible moving directly to a 1000 grit SiC paper. After grinding, samples were rinsed with distilled water, acetone and ethanol and dried with a blow dryer.

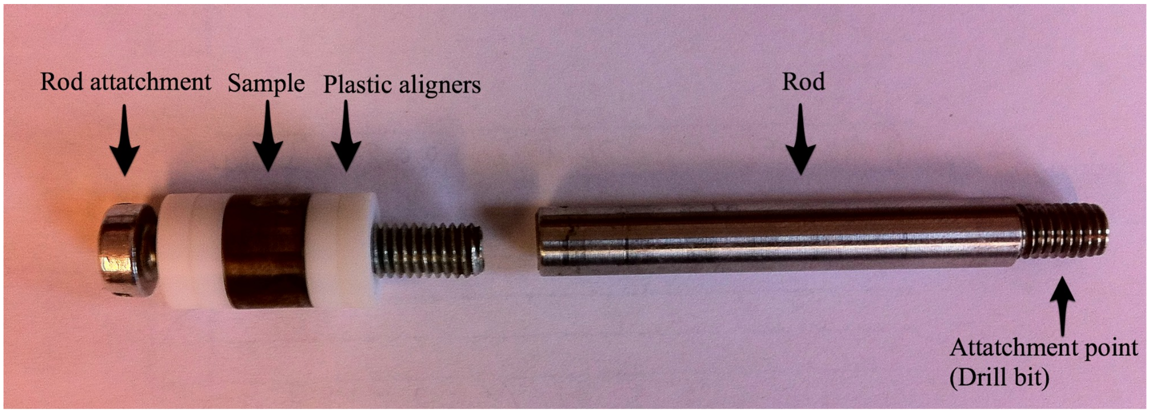

Figure 3.3: *Sample holder for pre treatment of cylindrical steel samples used in polarization experiments. All metallic parts made in carbon steel to avoid galvanic couplings.*

3.4 Apparatus

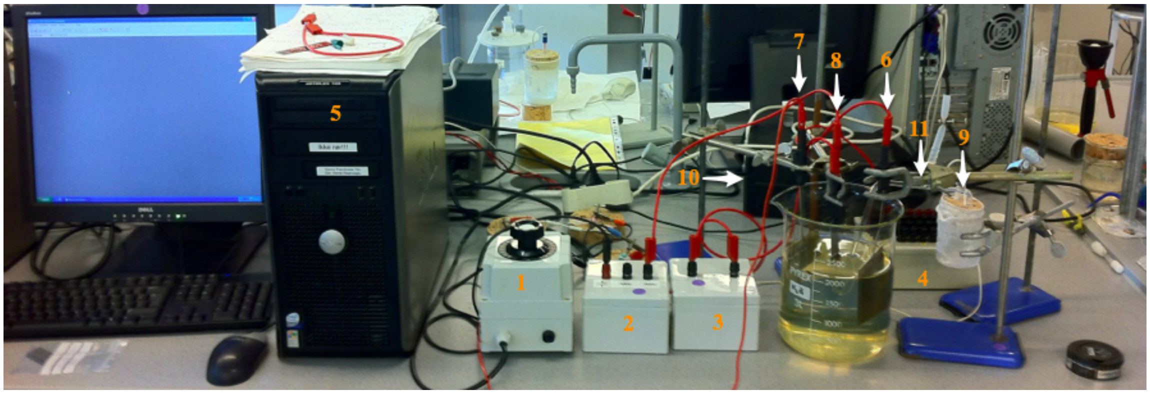

Figure 3.4: *Picture captured of the weight loss setup with each of its components numbered:* **1.** *VariAC,* **2.** 500μ*F capacitor +* 10Ω *resistor,* **3.** *10H Inductance,* **4.** 1Ω *resistor,* **5.** *in-PC Gamry Reference G750 potentiostat,* **6.** *DC counter electrode,* **7.** *AC counter electrode,* **8.** *Working electrode,* **9.** *SCE reference electrode,* **10.** *Isolating transformer,* **11.** *Salt bridge*

Figure 3.4 depicts a simplistic view of the basic apparatus used for all experiments in this paper. A technical view of this basic circuit structure is given in figure 3.5. Detailed apparatus descriptions for each of the different experiments are given in relevant sections to follow.

The setup was developed by F. Bolzoni [15], but has been modified [9] to include a potentiostat in contrast to the original 12V battery DC source. It consists of one AC circuit and one ordinary three-electrode DC-circuit. The two are separated to avoid mutual interference. This is achieved through a 500µ*F* capacitor in the AC circuit and a 10H inductance in the DC circuit. These work as filters for DC and AC signals respectively. The inductance introduced a resistance of 9.4Ω to the circuit and needed to be considered and corrected for in measurements. The VariAC is the AC source, delivering an AC signal with a frequency of 50Hz[2]. The potentiostat is the DC source. The resistors were inserted to measure both the actual AC delivered by the VariAC on the working electrode and the voltage response upon polarization in the DC circuit. Titanium counter electrodes and a standard calomel reference electrode (SCE) immersed in saturated KCl were used. The electrolyte was 3.5wt% NaCl. Reagent grade NaCl was mixed with distilled water to avoid contaminations. Power supplies were connected to an isolating transformer, establishing a common ground for the entire setup both for HSE purposes and to avoid ohmic losses. Before experiments were initiated, all wires were checked and approved by measuring their resistance using a multimeter. Clamps used to connect electrodes were also checked, ensuring their conductivity were satisfactory.

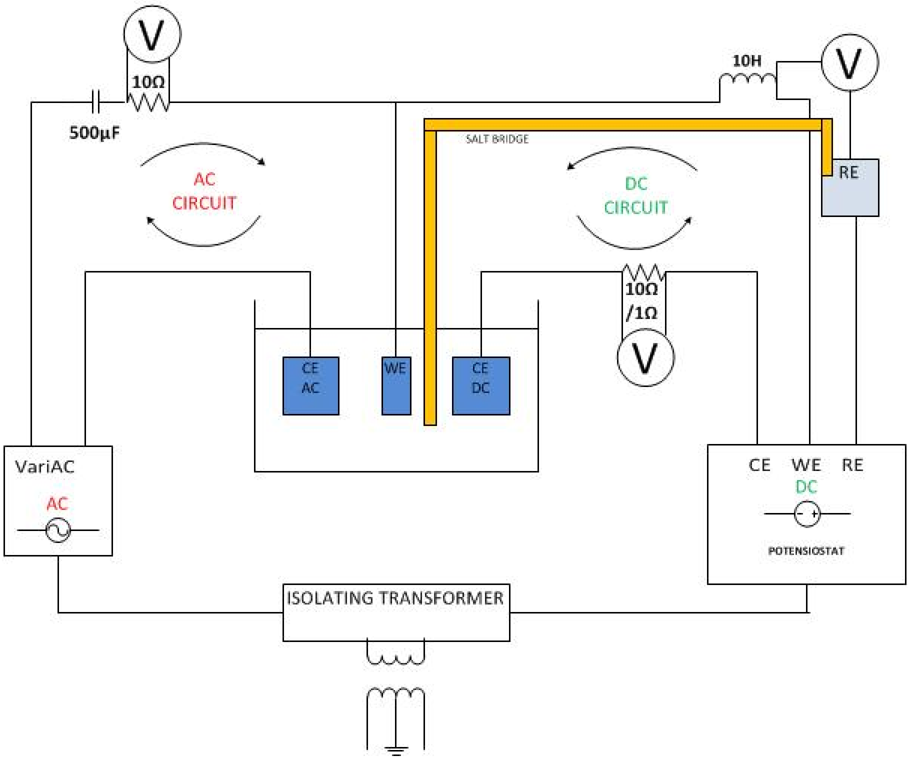

Figure 3.5: *Basic circuit structure used for all weight loss experiments.*

---

[2] A frequency of 50Hz is the default setting on the VariAC and is not possible to adjust.

3.4.1 Weight loss experiments (stationary working electrode)

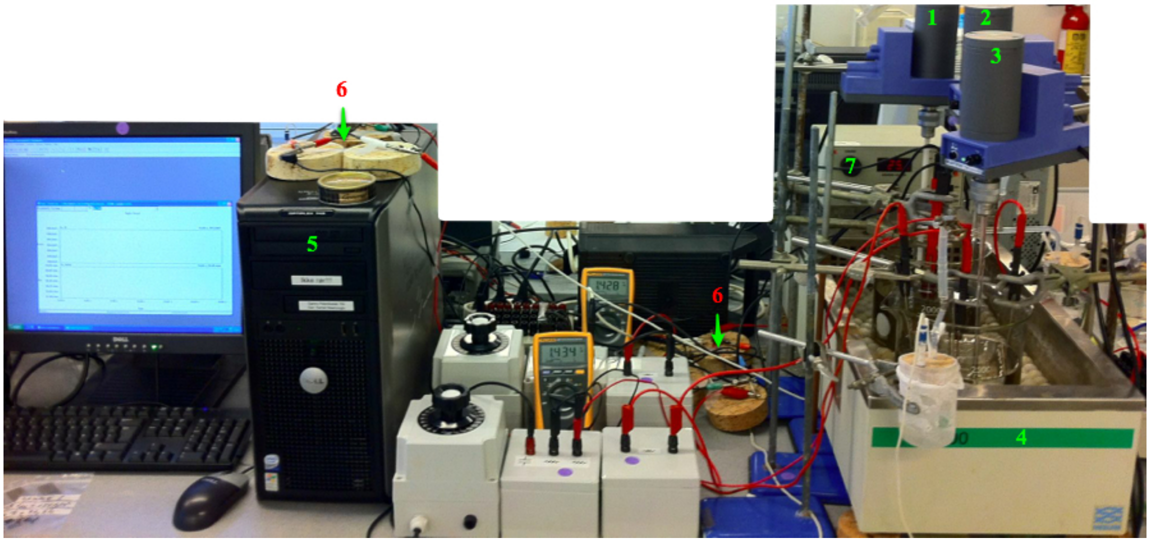

Figure 3.6: *Overview - setup. Two active circuits.* ***1, 2, 3.*** *Rotating rods driven by electrical motor,* ***4.*** *Temperature controlled chamber,* ***5.*** *in-PC Gamry Reference G750 potentiostat,* ***6.*** *Connection clamps (potentiostat - circuit),* ***7.*** *Temperature control. Multimeters visible in figure were connected to observe the applied AV.*

Experiments at the open circuit potential, E_{OC}

Figure 3.6 shows an overview picture of the setup. Two separate circuits connected to one computer each (with Gamry potentiostat and software installed) were operated during these experiments. The basic circuit structure was identical to the one previously described, but an explanatory circuit drawing has been included in figure 3.7(a) to supplement this. 3.7(b) gives a closer look at the experiment cell itself. The cells were placed in a temperature control chamber to ensure that the temperature was kept constant at room temperature (25 °C). This chamber was filled with water and was constantly stirred. In order to attain accurate and reproducible results from the experiments, the electrolyte needed to have a homogenous and constant concentration of oxygen. This was achieved by introducing rotating glass rods driven by electrical motors (**2.** and **3.** in figure 3.6) in the experiment cell. The rotational speed was kept constant and equal at 100 rpm for both cells in all experiments.

Experiments at fixed potentials, E_x

A separate string of experiments where the working electrode was to be potensiostatically polarized to fixed potentials were also performed. This was achieved simply by changing experimental parameters via the Gamry software, making alterations to what is seen in figure 3.6 unnecessary.

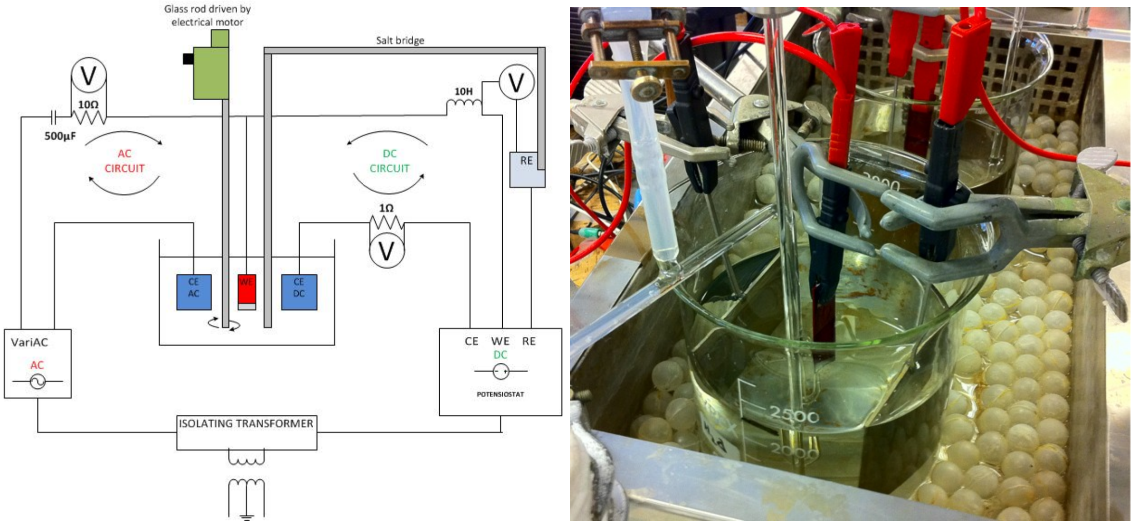
Glass rod driven by electrical motor
Salt bridge
V
10Ω
500µF
AC CIRCUIT
DC CIRCUIT
10H
V
RE
1Ω
V
CE AC
WE
CE DC
VariAC
AC
CE WE RE
DC
POTENSIOSTAT
ISOLATING TRANSFORMER
2500
2000

(a) (b)

Figure 3.7: *(a) Circuit structure, (b) Experiment cell*

3.4.2 Weight loss experiments (rotating working electrode)

Figure 3.8 shows an overview picture of the setup used for the experiments requiring a rotating working electrode. Also in this case, the circuit structure was the same as the basic one described earlier. A supplementary circuit drawing is depicted in figure 3.9(a). Figure 3.9(b) gives a closer look at the experiment cell. A rotating electrode setup with adjustable rotational speed was used for the working electrode, simulating flow. Pt counter electrodes were used. As in the experiments with a stationary working electrode, A SCE reference electrode immersed in saturated KCl allowed for potential measurements. In order to ensure temperature control in these experiments, a water pump (**4.** in figure 3.8) was used to drive water through the outer chamber of the experiment cell. A closed cycle containing water driven by the pump was led through a temperature controlled chamber (keeping 25 °C) by the use of rubber tubing and a copper coil. The rubber tubing was connected to the hollow copper coil so that when passing through the temperature controlled chamber, the water in the closed cycle would be carried inside the coil. The purpose of this being to exploit the favorable heat conduction properties of copper.

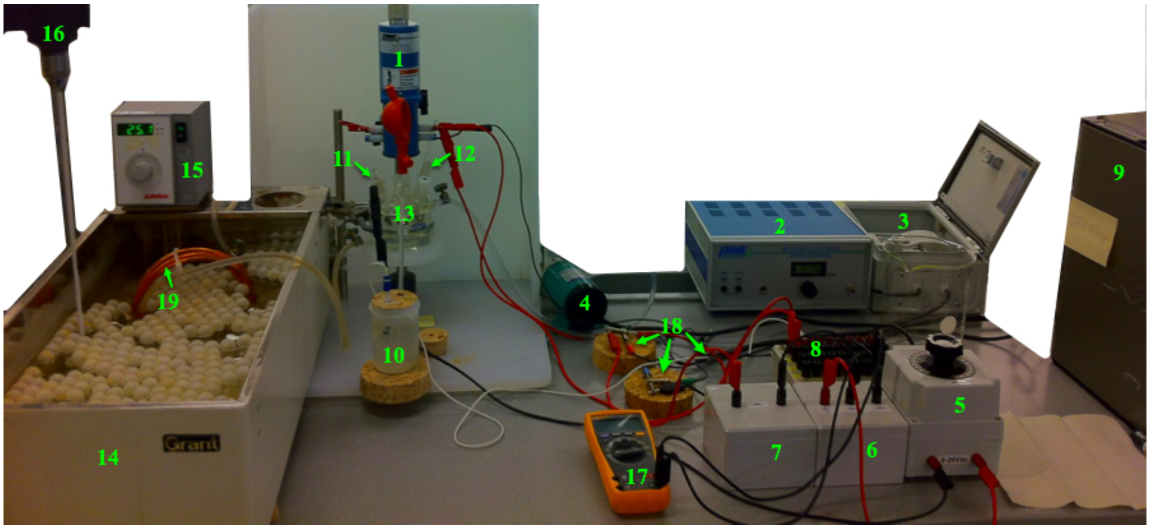
16
1
15
11
12
13
9
2
3
19
4
18
10
8
5
14
7
6
17

Figure 3.8: *Overview - experiment cell.* ***1.*** *Rotation motor,* ***2.*** *Rotation control and power supply,* ***3.*** *Control unit for water pump,* ***4.*** *Water pump,* ***5.*** *VariAC,* ***6.*** *500µF capacitor + 10Ω resistor,* ***7.*** *10H inductance,* ***8.*** *1Ω resistor,* ***9.*** *In-PC Gamry Reference 750 potentiostat,* ***10.*** *Reference electrode (SCE) with container filled with saturated KCl,* ***11.*** *AC counter electrode,* ***12.*** *DC counter electrode,* ***13.*** *Electrolyte container (Experiment cell),* ***14.*** *Temperature control chamber,* ***15.*** *Temperature control unit,* ***16.*** *Electrical motor with stirring attachment,* ***17.*** *Multimeter,* ***18.*** *Connection clamps, Gamry,* ***19.*** *Copper coil for temperature control.*

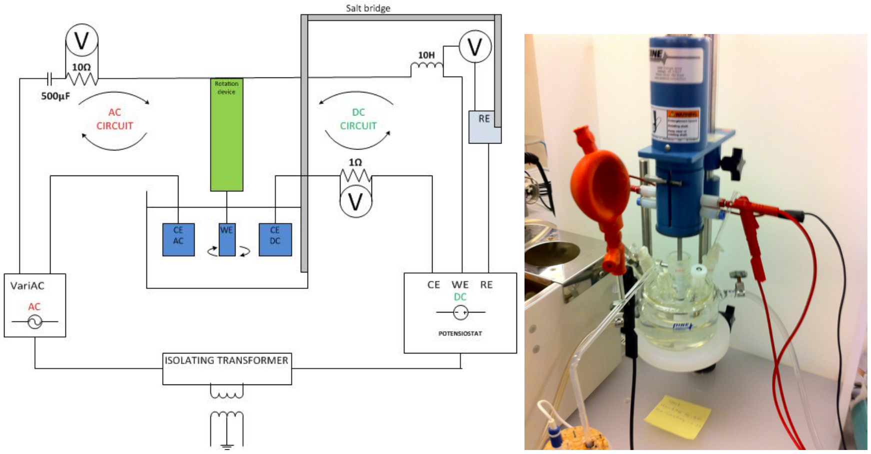
Salt bridge
V
10Ω
500µF
AC CIRCUIT
Rotation device
DC CIRCUIT
10H
V
RE
1Ω
V
CE AC
WE
CE DC
VariAC
AC
CE WE RE
DC
POTENSIOSTAT
ISOLATING TRANSFORMER

(a) (b)

Figure 3.9: *(a) Circuit structure, (b) Setup*

3.5 Test procedure

3.5.1 Weight loss experiments - stationary working electrode

Experiments at the open circuit potential, E_{OC}

Linear polarization resistance (LPR) measurements were performed using the in-PC Gamry potentiostat. Via the pre-installed Gamry software[3], the experiment mode "R_p/E_c - Trend" was selected. This experiment mode will polarize the working electrode (steel sample) ±10mV relative to E_{corr} at logging time ($\Delta E = 20mV$). The resulting current response is subsequently logged over this potential span. The polarization resistance (R_p) is then calculated from ΔE and ΔI through the Stern Geary equation (equation 3.1). This sequence is repeated at intervals determined by the user. The duration of experiments conducted in this paper was 3 days (72h) with such LPR-scans at one hour intervals. Figure 3.10 depicts the input window, in this case for an experiment at $i_{AC} = 500A/m^2$, in which appropriate input-values were inserted prior to each experiment.

$$R_p[\Omega] = \frac{B}{i_{corr}} = \frac{\Delta E}{\Delta I} \tag{3.1}$$
$$B[mV/dec] = \frac{b_a \cdot b_c}{2.3(b_a + b_c)}$$

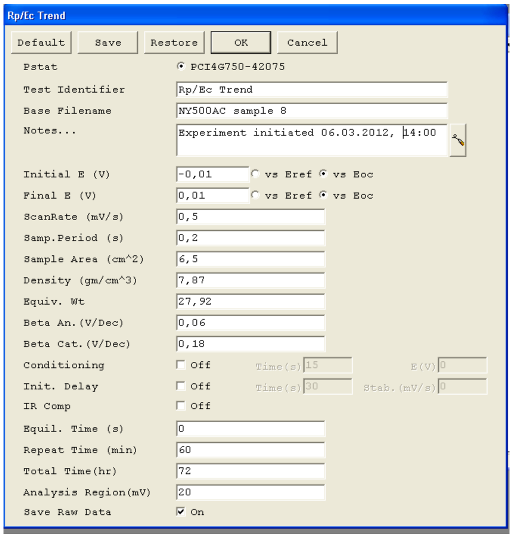

Pstat	● PCI4G750-42075		
Test Identifier	Rp/Ec Trend		
Base Filename	NY500AC sample 8		
Notes...	Experiment initiated 06.03.2012, 14:00		
Initial E (V)	-0,01	○ vs Eref ● vs Eoc	
Final E (V)	0,01	○ vs Eref ● vs Eoc	
ScanRate (mV/s)	0,5		
Samp.Period (s)	0,2		
Sample Area (cm^2)	6,5		
Density (gm/cm^3)	7,87		
Equiv. Wt	27,92		
Beta An.(V/Dec)	0,06		
Beta Cat.(V/Dec)	0,18		
Conditioning	☐ Off	Time(s) 15	E(V) 0
Init. Delay	☐ Off	Time(s) 30	Stab.(mV/s) 0
IR Comp	☐ Off		
Equil. Time (s)	0		
Repeat Time (min)	60		
Total Time(hr)	72		
Analysis Region(mV)	20		
Save Raw Data	☑ On		

Figure 3.10: *Gamry software - input window R_p/E_c Trend - experiment*

---

[3] Gamry framework v. 5.51, program package DC105

Anodic and cathodic Tafel slopes are significantly influenced by the applied level of AC. Using constant and predetermined values for these parameters like the ones visible from figure 3.10 is for this reason not considered to be accurate. These input-values are default values selected by the Gamry software for use in an integrated analysis software, but should be disregarded. Potentiodynamic scans were performed at the end of each experiment in order to extract correct polarization data and Tafel slopes for each individual experiment. These scans were performed in two separate steps. Firstly, a scan in the cathodic direction relative to E_{corr} was performed. When the potential had stabilized back to its original value, the anodic scan was performed. The two sets of data points were combined to form polarization curves in the analysis.

Weight loss measurements were conducted straight forward by weighing samples before applying coating, then weighing them once more upon completion of experiment and chemical post treatment. The total weight loss could then be calculated, hence also the corrosion rate (CR) through equation 3.2 where ΔW is the weight loss, t is the time of exposure, A is the exposed surface area and ρ is the steel density.

$$CR[mmy] = \frac{\Delta W}{t \cdot A \cdot \rho} \tag{3.2}$$

The mentioned chemical post treatment consisted of two separate procedures. Firstly, to rid the samples of the protective coating, a powerful solvent was needed. "Microstrip" was used. This is a product made specifically for the applied coating. Samples were completely immersed during 30 second cycles while stirring, until coating was removed. The number of cycles needed, varied between 5-7. No metal loss was documented. The second step of the procedure was ridding the samples of corrosion products. For this purpose an acidic solution in accordance with ASTM G1-03, C.3.5 [16] was utilized. This solution consists of distilled water, concentrated HCl and hexamethylene tetramine which is a corrosion inhibitor. Samples were, also here, completely immersed during 30 second cycles while stirring. The number of cycles needed, varied for the different applied AC densities. Some additional uniform metal loss was unavoidable in this process due to the acidic nature of the solution. To compensate for this, a clean steel sample given the same pre treatment as the test samples was exposed to the solution through several cycles. Weight losses were logged after each cycle. The additional weight loss encountered due to this procedure could then be subtracted in the actual experiments. The results of this investigation are given graphically in figure 4.2 in the results section.

A test matrix describing the experiments performed in this category is given in table 3.4. Each of the experiments were carried out twice to ensure reliable results.

Table 3.4: *Test matrix for weight loss experiments with stationary working electrode at E_{OC}. The temperature was kept constant at T = 25 °C. The electrolyte was 3.5 wt% NaCl and the exposure time was t = 3 days (72h) for all experiments.*

Test matrix		
Experiment	$A_{exposed}$ $[cm^2]$	i_{AC} $[A/m^2]$
Weight loss, LPR	6.5	100
	6.5	250
	6.5	500
	5.7	700

Experiments at fixed potentials, E_x

These experiments were performed using the same apparatus as the above described experiments at E_{OC}. The working electrode was polarized to the wanted potential by the Gamry potentiostat via the computer software. A multimeter was used to manually verify correct polarization. This was inserted between the inductance and the reference electrode as graphically described in the circuit drawing in figure 3.7(a).

Weight loss measurements were performed using the same procedure as described in the previous section. Table 3.5 depicts a test matrix for the experiments performed under this category.

Table 3.5: *Test matrix for weight loss experiments with stationary working electrode at fixed potentials. Experimental conditions otherwise the same as in table 3.4. Total exposure time was t = 3 days (72h) for all experiments*

Test matrix			
Experiment	$A_{exposed}$ $[cm^2]$	i_{AC} $[A/m^2]$	E_x $[mV_{SCE}]$
Weight loss, polarization	6.5	250	[-600, -800, -1000, -1200]
	6.5	500	[-600, -800, -1000, -1200]
	5.7	700	[-600, -800, -1000, -1200]

3.5.2 Weight loss experiments - rotating working electrode

Prior to experiments, the electrolyte container was thoroughly rinsed with 3.5 wt% NaCl electrolyte. The steel sample was then mounted on to sample holder and attached to the rotating electrode setup. Electrical conduction was verified by the use of a multimeter between sample and connection clamp for the working electrode entering potentiostat. The electrolyte was inserted in its container and the sample was lowered into position. Subsequently, the reference and counter electrodes were positioned. Rotation was initiated via the rotation control unit and the preferred level of AC was applied.

Table 3.6: *Test matrix for experiments using a rotating working electrode. The temperature was kept at RT and equal for all samples were* $A_{exposed} = 3cm^2$. *The electrolyte was 3.5 wt% NaCl and the exposure time was t = 3 days (72h) for all experiments.*

Test matrix		
Experiment	Rotational speed $[rpm]$	i_{AC} $[A/m^2]$
Weight loss, rotation	250	100
		250
		500
		700

3.6 Surface characterization

To investigate the corroded sample surfaces upon experiment completion, a field emission scanning electron microscope (FESEM) was used. More specifically, a Zeiss Ultra 55 limited edition illustrated in figure 3.11.

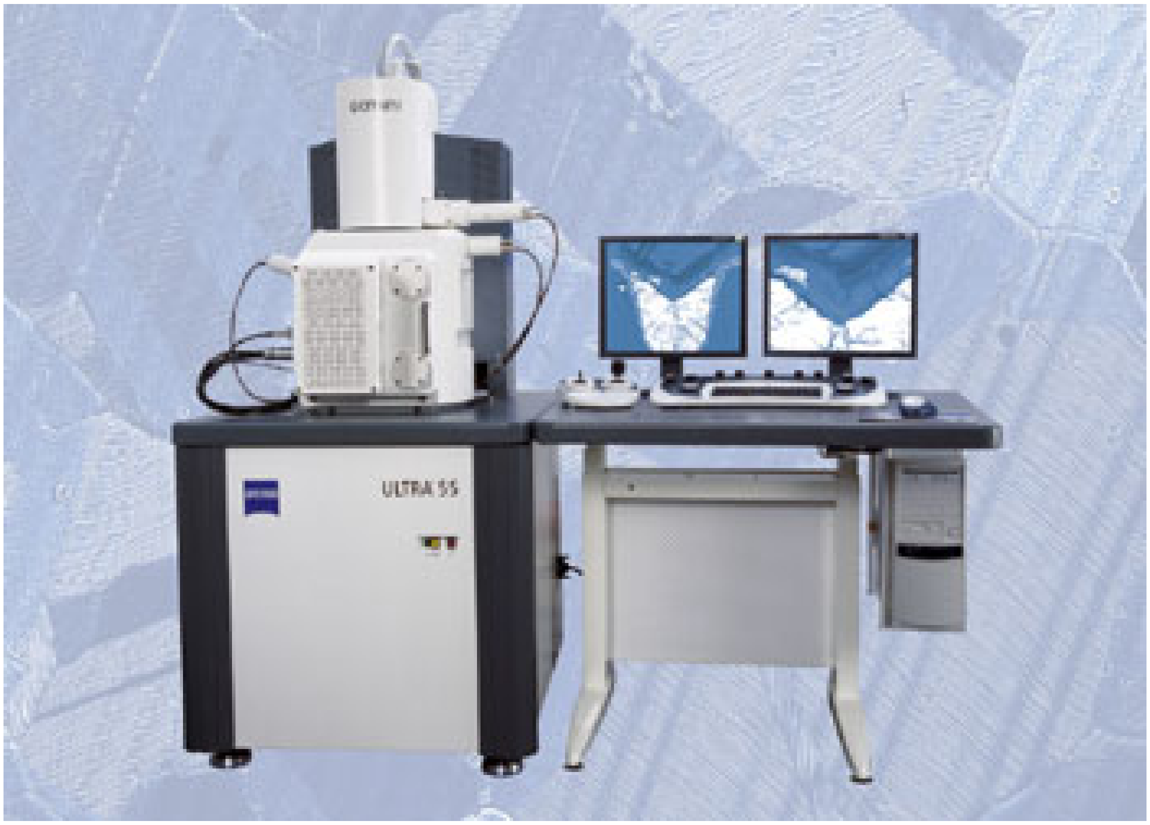

Figure 3.11: *Zeiss Ultra 55 limited edition (FESEM). Field emission scanning electron microscope used for surface characterizations throughout experiments.*

Chapter 4

Results

In the following sections, results from all three categories of performed experiments will be presented. To maintain an organized structure, they have been divided into three separate sections:

Section 4.1 Weight loss experiments - stationary WE at open circuit

Section 4.2 Weight loss experiments - stationary WE at fixed potentials

Section 4.3 Weight loss experiments - rotating WE at open circuit

4.1 Weight loss experiments - stationary WE at open circuit

4.1.1 Corrosion rate

The experiments were performed with a duration of 3 days (72h) at AC densities 100, 250, 500 and 700 A/m^2. Figure 4.1 shows i_{corr} (with resulting CR) as a function of applied i_{AC}. Table 4.1 contains key results from these experiments.

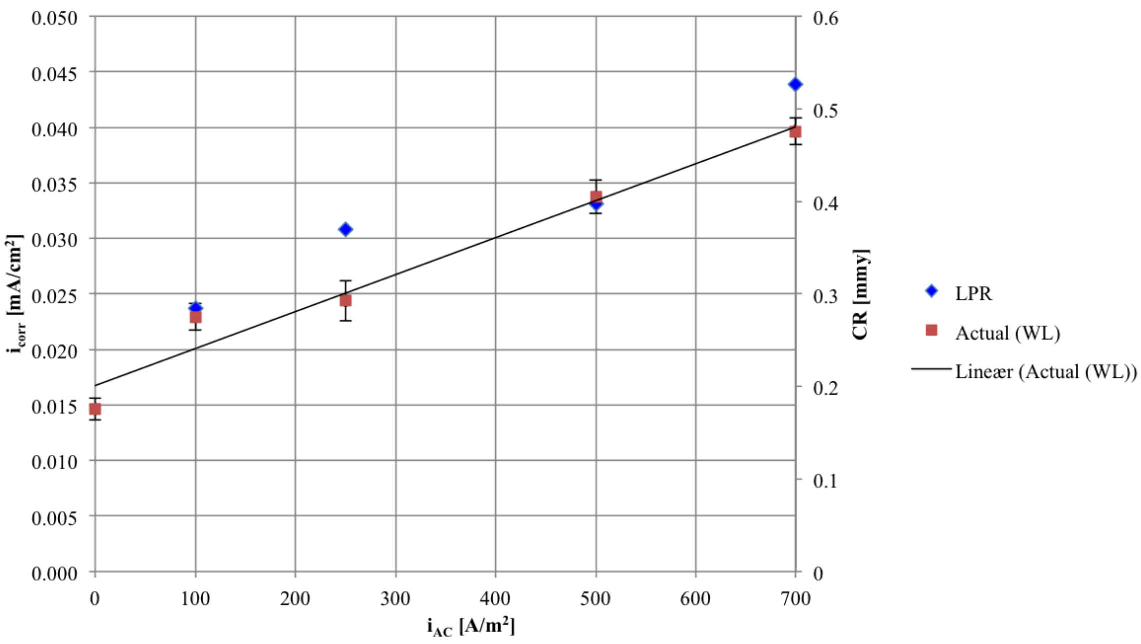

Figure 4.1: *i_{AC} vs. CR. Blue dots represent LPR measurements (mean values) while red dots represent actual weight loss measurements. Standard deviation plotted for weight loss measurements. Data for $i_{AC} = 0$ from specialization project [2].*

Table 4.1: *Key results from LPR - and weight loss experiments. Values of i_{corr} in table A.1 in appendix A.*

Key results					
$i_{AC}[A/m^2]$	E_{corr} [mV_{SCE}]	R_p^{mean} [Ω]	CR_{LPR}^{mean} [mmy]	CR_{LPR}^{end} [mmy]	CR_{WL} [mmy]
100	-770	130	0.28	0.34	0.27
250	-778	100	0.36	0.47	0.28
500	-800	93	0.39	0.72	0.39
700	-790	80	0.51	0.76	0.46

4.1.2 Weight loss measurements

The measured weight losses enabled calculation of corrosion rates (CR) based on the total time of exposure according to equation 3.2. It has been established that application of AC into an otherwise ordinary electrochemical cell, will increase the corrosion current and thereby also the CR. An approximately linear correlation between applied AC density and CR was observed. This is illustrated graphically in figure 4.1.

The additional weight loss encountered as a result of chemical post treatment, needed to be subtracted from the measured weight loss according to ASTM G1-03 [16]. Figure 4.2 graphically shows this additional weight loss depending on the number of cycles of total immersion in the acidic solution. Table 4.2 contains data recorded during measurements.

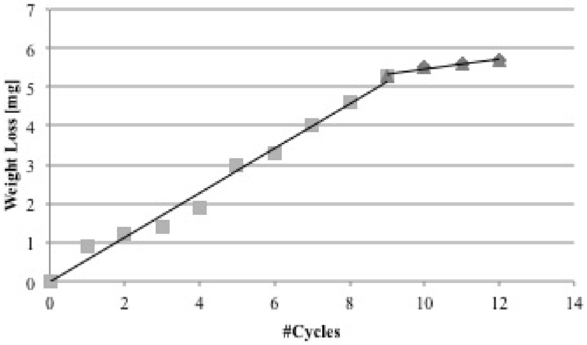

Figure 4.2: *Measured added weight loss for steel samples exposed to solution in accordance with ASTM G1-03, C.3.5. One cycle corresponds to 30 seconds of total immersion. Values were collected from a clean sample with identical pre treatment as the test samples.*

Table 4.2: *Correction for added metal loss encountered during chemical post treatment.*
**Data from specialization project [2] with an exposure time of 7 days.*

Weight loss measurements				
$i_{AC} [A/m^2]$	Δm^{mean} [mg]	$\#cycles_{HCl}$	$\Delta m^{mean}_{corrected}$ [mg]	CR [mmy]
0	19.7*	5	16.7*	0.17
100	12.8	3	11.3	0.27
250	13.6	3	12.1	0.28
500	19.8	5	16.8	0.39
700	19.0	3-4	17.3	0.46

4.1.3 LPR measurements

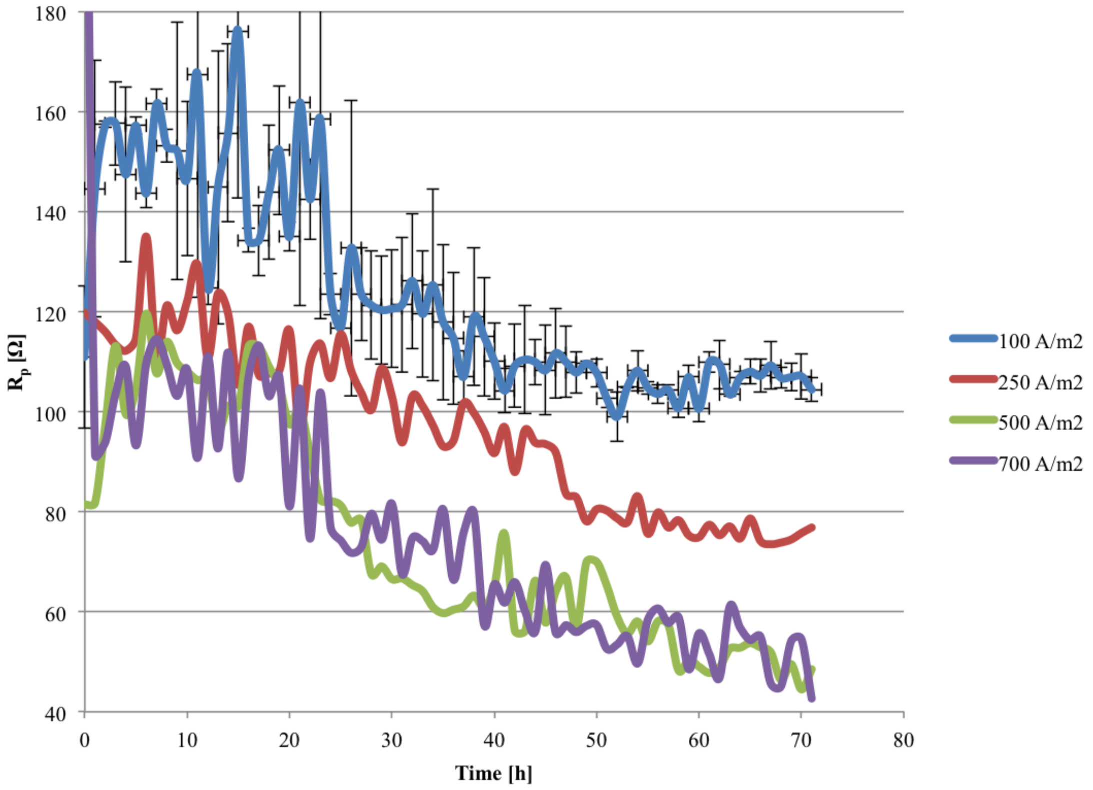

Figure 4.3: *R_p vs. time. Recorded using Gamry in-PC potentiostat and software.*

Figure 4.3 shows the development of the polarization resistance (R_p) during the total exposure time for each AC density tested. These data were used to calculate corrosion rates. The standard deviation has been plotted for $i_{AC} = 100A/m^2$ only (see figure A.1 and A.2 in appendix A for all plots). In order to perform corrosion rate-calculations[1], the proportionality constant B which is based on anodic and cathodic Tafel slopes, were needed. Figure 4.4 shows polarization curves recorded at the end of each experiment. Tafel slopes for each curve were extracted from this and constants were calculated. A proportionality constant B of $20mV/dec$ was found to represent all AC densities with a sufficient amount of precision ($\pm 1mV/dec$). A criteria for the LPR technique to be accurate, is straight cathodic and anodic lines in such a polarization curve. Introducing AC will alter the nature of polarization data. From figure 4.4, it is observed that as AC densities increase, curves show an increasingly irregular behavior. For 500 and 700 A/m^2 an oscillating tendency is visible in the cathodic area. The anodic area (relative to E_{corr}) behaves similarly for all AC densities, also here, with an oscillating tendency. Despite this behavior, characteristic areas of the curves such as were hydrogen reduction is active, are recognized. Comparing values of CR_{LPR}^{mean} and CR_{WL}, as has been done in figure 4.1, shows there is good correspondence between the two parameters. This substantiates assumptions made in the calculations, though a level of error will most likely still be present.

---

[1] Stern Geary equation (equation 3.1)

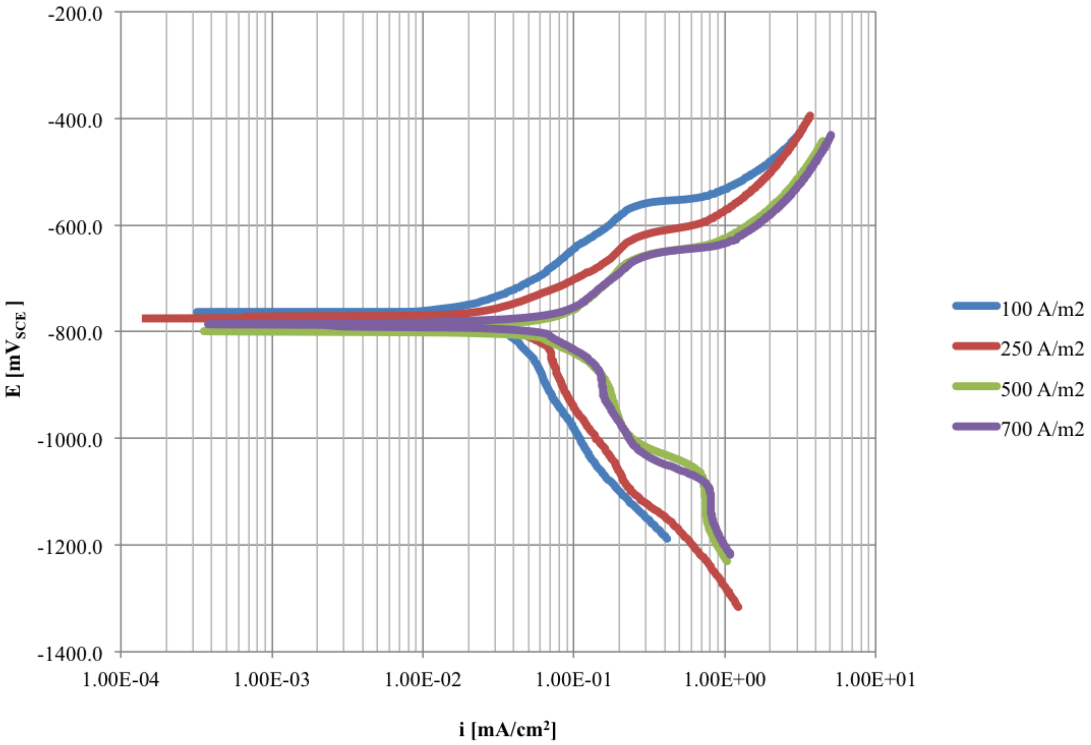

Figure 4.4: *Polarization curves - Stationary working electrode, E_{OC}*

4.1.4 Time dependency of i_{corr}

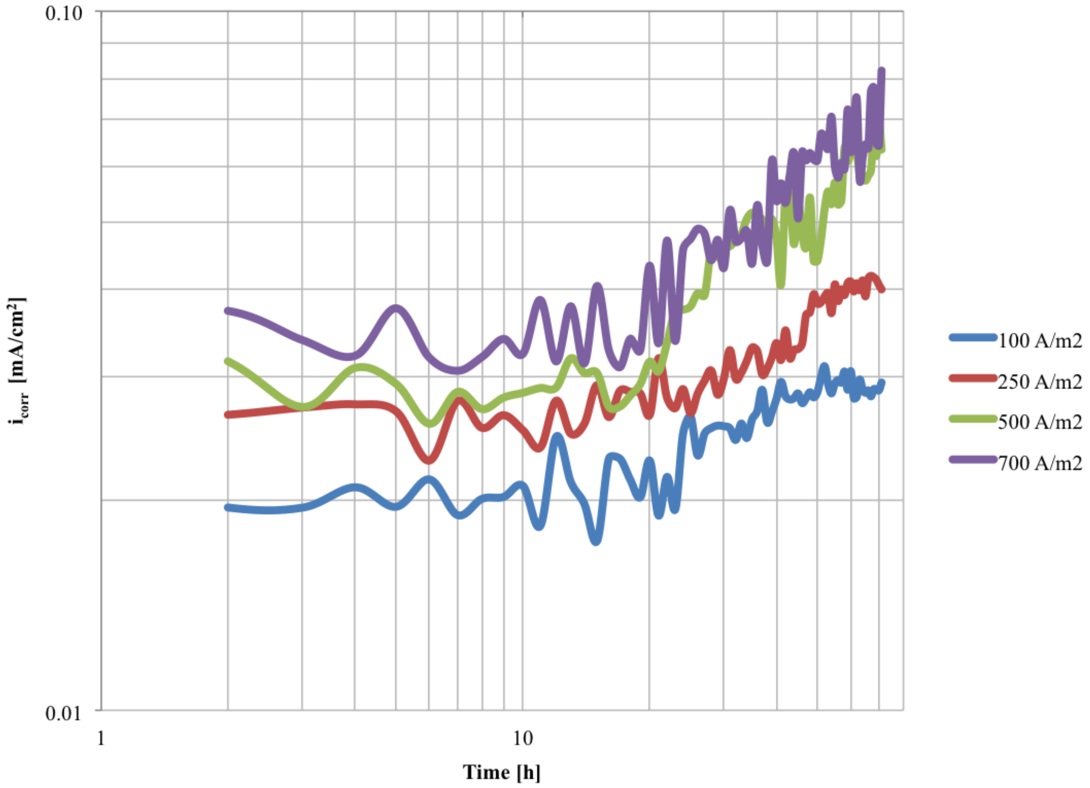

Figure 4.5: i_{corr} *vs. time.*

Figure 4.5 shows the development of i_{corr} as a function of time based on the data from LPR measurements (R_p was converted to i_{corr} by the use of the proportionality constant B [mV/dec]). Initially, i_{corr} is fairly stable for all AC densities. After roughly 10h, it starts to increase.

4.1.5 Corrosion potential

In the presence of AC, the corrosion potential, E_{corr} of steel in 3.5wt% NaCl, behaves in a well documented and characteristic manner. An immediate drastic potential drop is followed by a gradual stabilization towards a less negative value though still cathodic to the case at $i_{AC} = 0A/m^2$. The potential at which stabilization occurs, becomes more cathodic as applied AC is increased. Figure 4.6 depicts the behavior of E_{corr} during these experiments.

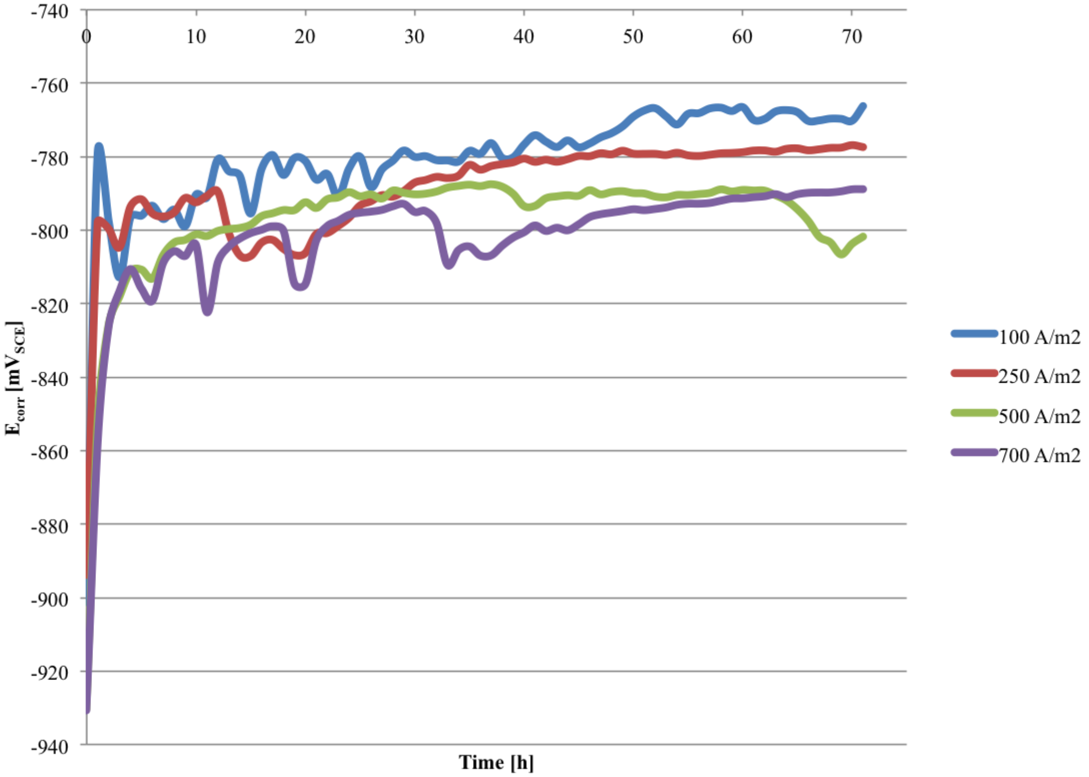

Figure 4.6: *E_{corr} vs. time. Recorded using Gamry in-PC potentiostat and software.*

4.1.6 Surface characterization

During a specialization project by the author in the autumn of 2011 [2], a similar experiment in 3.5wt% NaCl electrolyte at E_{OC} with different applied levels of AC was performed. As a part of this work, a comprehensive surface characterization study was completed. The only difference between these experiments, was the use of a manual potentiostat then, and an automatic in-PC potentiostat now. The experiment cells are identical, making the results of this study equivalently relevant. They have therefore been included in this paper.

Macroscopic

In the presence of AC, a black surface oxide is formed. This was the case for all AC densities applied. Figure 4.7 shows photos captured at different durations and test parameters.

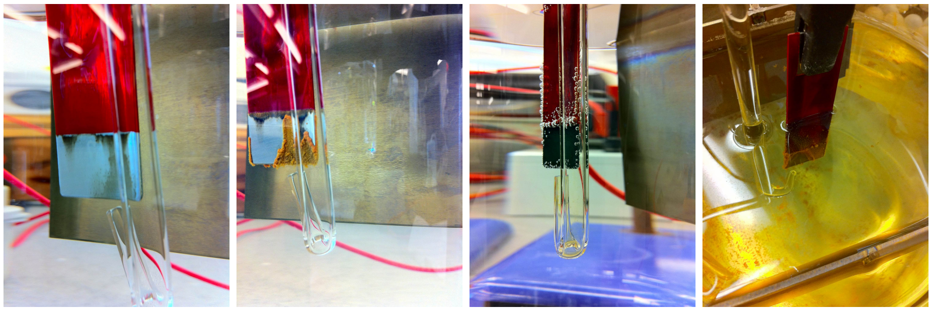

(a) $i_{AC} = 0A/m^2$. 5 minutes into experiment.
(b) $i_{AC} = 0A/m^2$. 24h into experiment.
(c) $i_{AC} = 700A/m^2$. 5 minutes into experiment.
(d) $i_{AC} = 700A/m^2$. 24h into experiment.

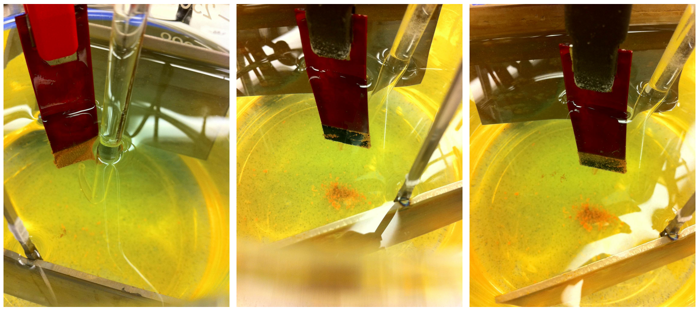

(e) $i_{AC} = 100A/m^2$. 24h into experiment.
(f) $i_{AC} = 100A/m^2$. 6 days into experiment.
(g) $i_{AC} = 100A/m^2$. 7 days into experiment.

Figure 4.7: *Photos captured at different durations and test parameters. Clear differences in surface activity are visible depending on test parameters [2].*

The layer of oxides in 4.7(c) was formed in a matter of seconds after application of AC. The entire exposed sample surface was covered and rapid hydrogen evolution was visible along the edges. No hydrogen evolution was visible in these first minutes on the counter electrodes (cathodes), suggesting some rapid surface activation taking place at the working electrode (anode) where it alternates between anodic and cathodic states. The sample in 4.7(a), where no AC was applied, a much slower reaction to the environment was observed. 24 hours into experiment, corrosion products are concentrated along edges and randomly on the exposed surface (figure 4.7(b)). The entire surface was not covered.

The oxide formed in the presence of AC is quickly and uniformly covered by corrosion products. Figure 4.7(e) shows a sample at $i_{AC} = 100A/m^2$ at 24 hours of exposure. This layer of corrosion products continuously formed and detached in cycles on top of the oxide for all AC densities. On one occasion ($i_{AC} = 100A/m^2$) the entire layer detached at the same time, illustrating its instability (figure 4.7(f)).

Microscopic

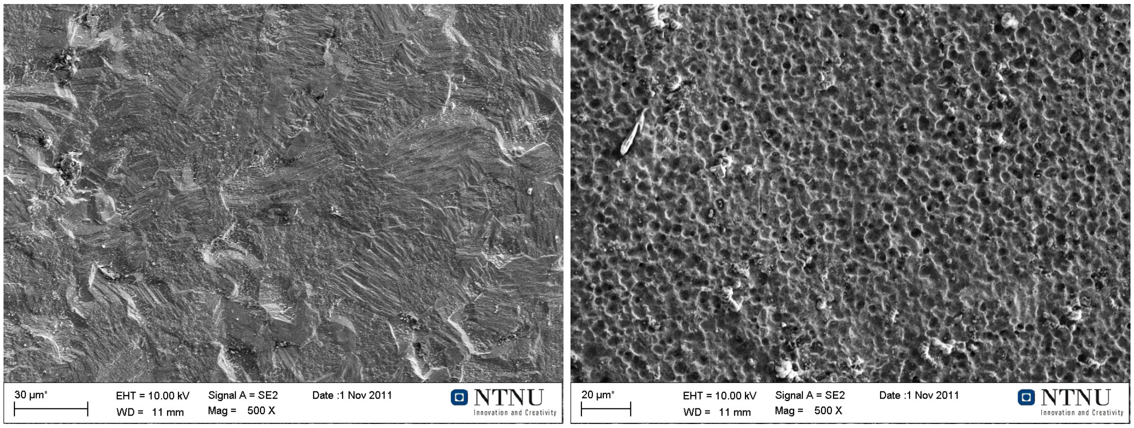
30 µm*
EHT = 10.00 kV
WD = 11 mm
Signal A = SE2
Mag = 500 X
Date :1 Nov 2011
NTNU
Innovation and Creativity
20 µm*
EHT = 10.00 kV
WD = 11 mm
Signal A = SE2
Mag = 500 X
Date :1 Nov 2011
NTNU
Innovation and Creativity

(a) $i_{AC} = 0A/m^2$, M = 500X

(b) $i_{AC} = 100A/m^2$, M = 500X

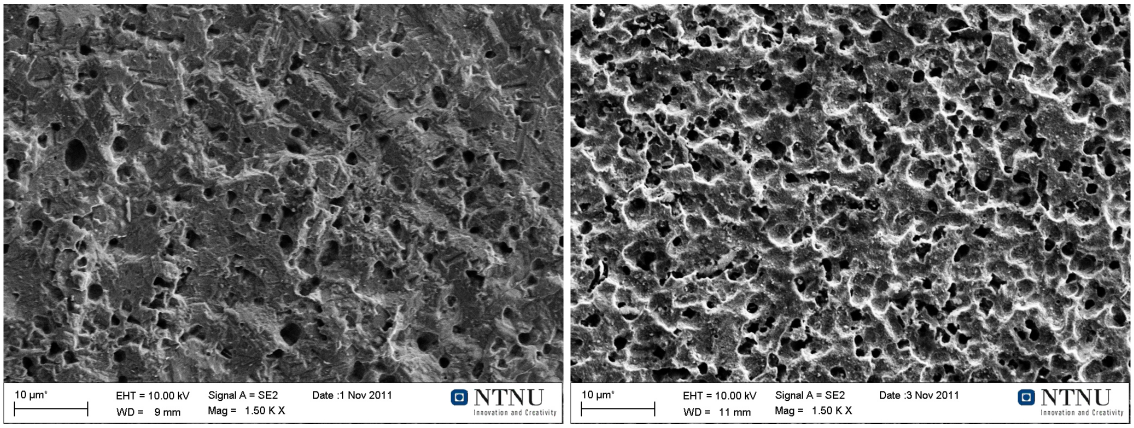
10 µm*
EHT = 10.00 kV
WD = 9 mm
Signal A = SE2
Mag = 1.50 K X
Date :1 Nov 2011
NTNU
Innovation and Creativity
10 µm*
EHT = 10.00 kV
WD = 11 mm
Signal A = SE2
Mag = 1.50 K X
Date :3 Nov 2011
NTNU
Innovation and Creativity

(c) $i_{AC} = 250A/m^2$, M = 1500X

(d) $i_{AC} = 500A/m^2$, M = 1500X

Figure 4.8: *SEM,* $i_{AC} = 0, 100, 250$ *and* $500A/m^2$.

Figure 4.8 shows samples subjected to different levels of AC upon removal of corrosion products (for the complete catalogue of surface characterization images, see figure B.1 through B.5 in appendix B). Figure 4.8(a) shows a sample where no AC was applied. The corrosion products which formed during the experiment were fairly homogenous and adhered well to the sample surface. Some areas of the sample were not at all covered by such corrosion products. These areas appeared unaffected and no deformation was visible. Areas covered by mentioned corrosion products appeared to have uniformly corroded, as in 4.8(a). 4.8(b) shows the surface profile of a sample exposed to $i_{AC} = 100A/m^2$. Shallow hemispherical pits throughout the entire surface are visible. As applied AC densities increase, the corresponding pit depths increase[2]. 4.8(c) and (d) displays samples exposed to $i_{AC} = 250$ and $500A/m^2$. The number of pits past their initiation stage increase as AC densities increase and for the sample exposed to $i_{AC} = 500A/m^2$ an elongated pit shape was observed.

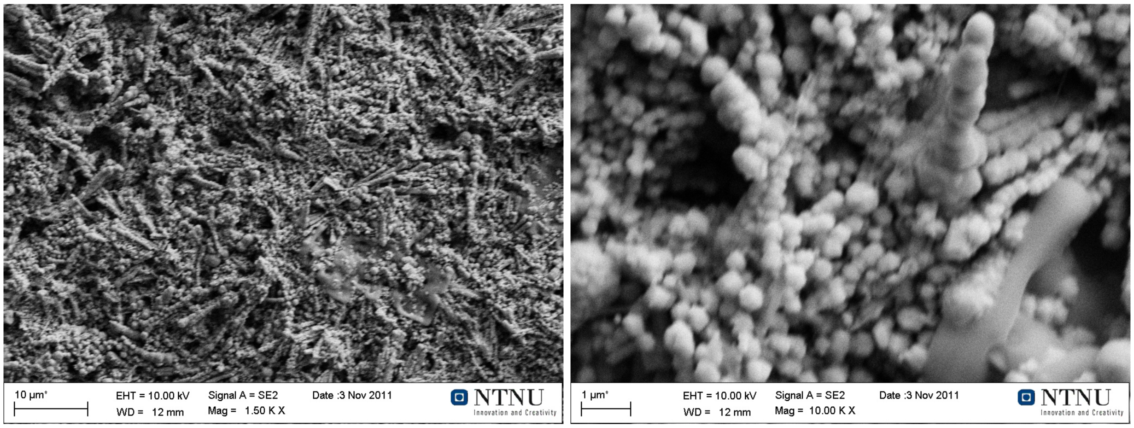
10 µm*
EHT = 10.00 kV
WD = 12 mm
Signal A = SE2
Mag = 1.50 K X
Date :3 Nov 2011
NTNU
Innovation and Creativity
1 µm*
EHT = 10.00 kV
WD = 12 mm
Signal A = SE2
Mag = 10.00 K X
Date :3 Nov 2011
NTNU
Innovation and Creativity

(a) $i_{AC} = 500A/m^2$, M = 1500X (b) $i_{AC} = 500A/m^2$, M = 10 000X

Figure 4.9: *SEM,* $i_{AC} = 500A/m^2$*. Iron oxide layer.*

Figure 4.9 shows pictures captured in SEM of the black iron oxide layer formed in the presence of AC. Its protective properties as a barrier for migration of ions are doubtful given its porous structure. Results from weight loss experiments support this assumption. An EDS analysis was performed in an attempt to determine the composition of the oxide. Figure 4.10 and table 4.3 summarizes results gained. An accelerating voltage of 10kV was used. The size of the resulting interaction volume was not considered and may be a source of error in the layers true chemical composition. The main components are as expected Fe and O. Cl is present in smaller quantities, which is consistent with observed pitting corrosion. The oxide layer is believed to consist of combinations of Fe_3O_2 and Fe_3O_4.

---

[2] Observation made qualitatively by first focusing inside the pit, then "refocusing" back to the surface

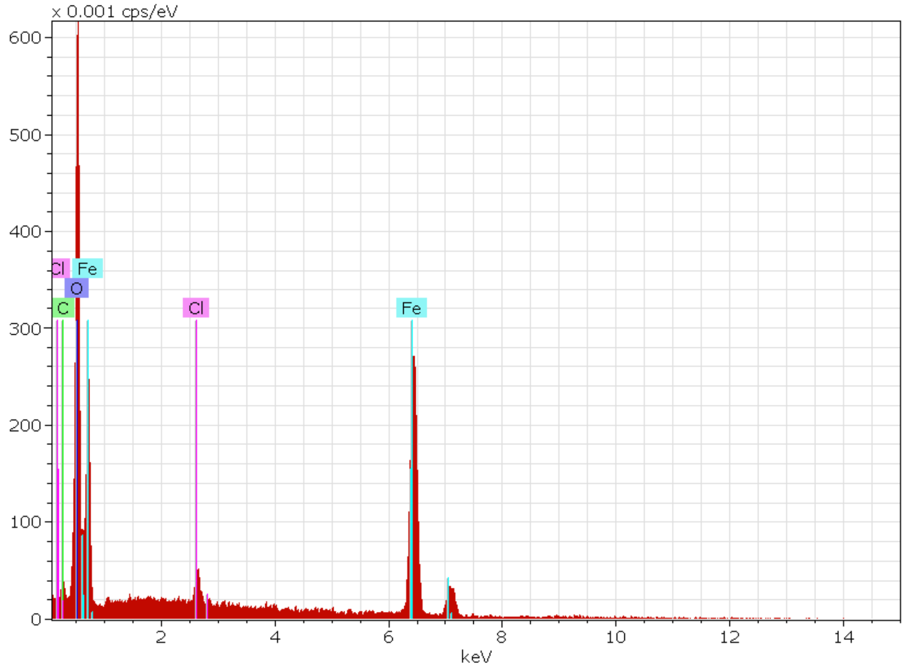

Figure 4.10: *Energy dispersive X-ray diffraction (EDS) microanalysis of the oxide formed on steel sample exposed to* $i_{AC} = 500A/m^2$.

Table 4.3

Quantitative analysis (EDS)				
	Fe	**O**	**C**	**Cl**
Atomic no.	26	8	6	17
Atom%	0.3048	0.5837	0.0986	0.0129
Mass%	0.4723	0.2591	0.0329	0.0127
Net intensity	6247	5768	247	562
Background	20	133	69	54
Sigma	0.0333	0.1536	0.3620	0.0795
K-factor	0.3387	0.7509	0.1469	0.0080
Atomic weight [g/mol]	55.845	16	12.01	35.453

4.2 Weight loss experiments - stationary WE at fixed potentials

4.2.1 Corrosion rate

The experiments were performed with a duration of 3 days (72h) at AC densities 250, 500 and 700 A/m^2. Experiments at fixed potentials -600, -800, -1000 and -1200 mV_{SCE} were performed for each AC density. Figure 4.11 graphically illustrates the CR in each case. This data is tabulated in table 4.4.

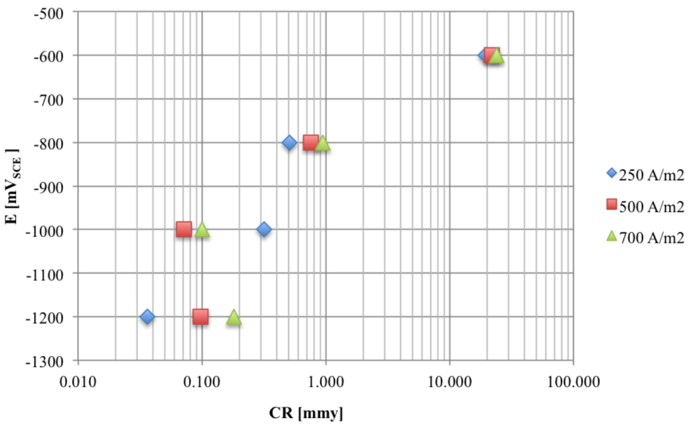

Figure 4.11: *E_x vs. CR.*

Table 4.4: *Results from experiments at fixed potentials. Weight loss measurements were performed in accordance with the procedure described in section 4.1.2.*

Key results					
i_{AC} $[A/m^2]$	E_x $[mV_{SCE}]$	Δm^{mean}[mg]	$\#cycles_{HCl}$	$\Delta m^{mean}_{corrected}[mg]$	**CR [mmy]**
250	-600	818.5	3	817.0	**19.48**
	-800	22.8	3	21.3	**0.51**
	-1000	14.2	1	13.5	**0.32**
	-1200	2.3	1	1.6	**0.04**
500	-600	907.2	3	905.7	**22.06**
	-800	32.2	2	31.2	**0.76**
	-1000	4.0	2	3.0	**0.07**
	-1200	5.1	2	4.1	**0.10**
700	-600	873.6	3	872.1	**24.05**
	-800	36.5	4	34.5	**0.95**
	-1000	4.5	2	3.5	**0.10**
	-1200	7.3	2	6.3	**0.18**

4.2.2 Surface characterization

Photos captured during the experiments in combination with a SEM study are used in this section to study the surfaces of the samples.

Macroscopic

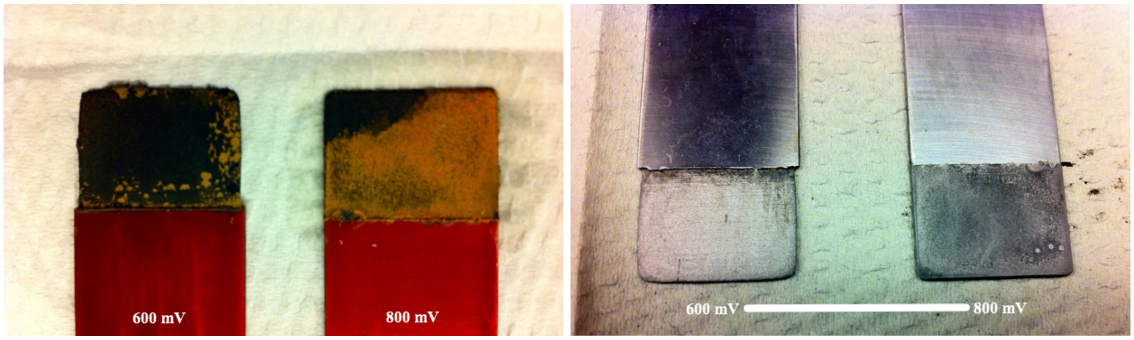

(a) Samples before post-treatment

(b) Samples after post-treatment

Figure 4.12: *Samples exposed to* $i_{AC} = 250A/m^2$ *for 3 days (72h) at -600 and -800 mV respectively.*

Figure 4.12 shows samples exposed to $i_{AC} = 250A/m^2$ at -600 and -800 mV_{SCE}. Heavy corrosion ($\sim$ 20 mmy) was documented for all AC densities at -600 mV_{SCE}. The corrosion attack uniformly covered the exposed surface. For the samples kept at -800 mV_{SCE}, pitting corrosion was detected even in the macroscopic characterization. This was the case for all AC densities.

Figure 4.13 shows samples upon completion of each experiment at -1000 and -1200 mV_{SCE} for all AC densities tested. At these potentials, the exposed samples behaved differently depending on applied AC density. At $i_{AC} = 250A/m^2$, the sample kept at -1200 mV_{SCE} showed no sign of corrosion. At this potential, for $i_{AC} = 500$ and $700A/m^2$, the opposite was the case and the characteristic black oxide layer was present. At $700A/m^2$ the surface was considerably more deformed than at $500A/m^2$. This became apparent after post-treatment. In the case where the working electrode was polarized to -1000 mV_{SCE}, the samples at $i_{AC} = 500$ and $700A/m^2$ showed no or little sign of corrosion. The black oxide was present, but once removed, the surface appeared relatively undeformed. At 250 A/m^2, the sample had corroded significantly. All these observations are consistent with measured weight losses and corrosion rates (figure 4.11, table 4.4).

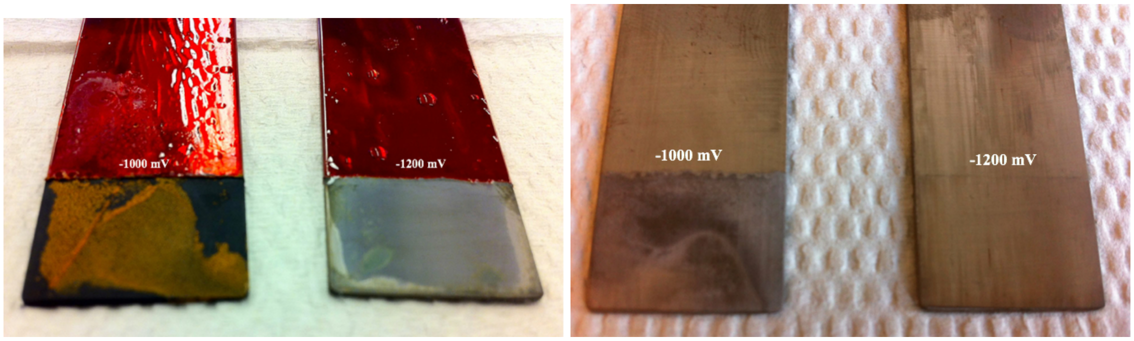
-1000 mV
-1200 mV
-1000 mV
-1200 mV

(a) Samples before post-treatment ($i_{AC} = 250 A/m^2$) (b) Samples after post-treatment ($i_{AC} = 250 A/m^2$)

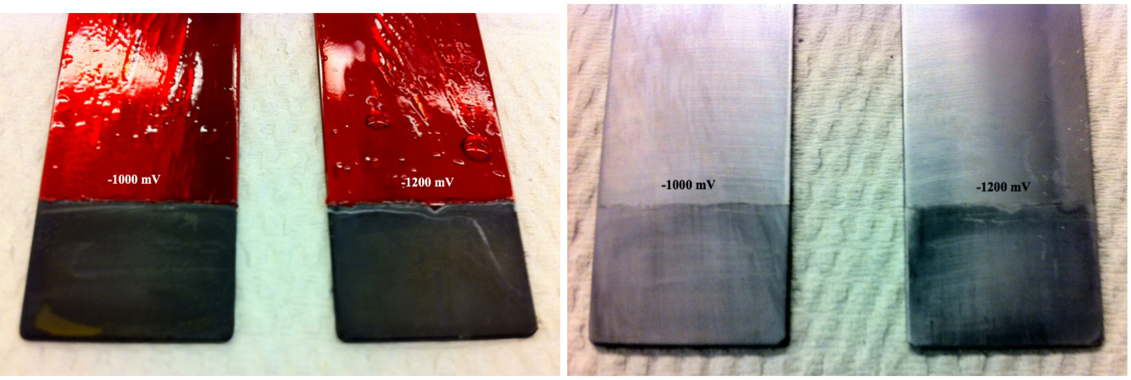
-1000 mV
-1200 mV
-1000 mV
-1200 mV

(c) Samples before post-treatment ($i_{AC} = 500 A/m^2$) (d) Samples after post-treatment ($i_{AC} = 500 A/m^2$)

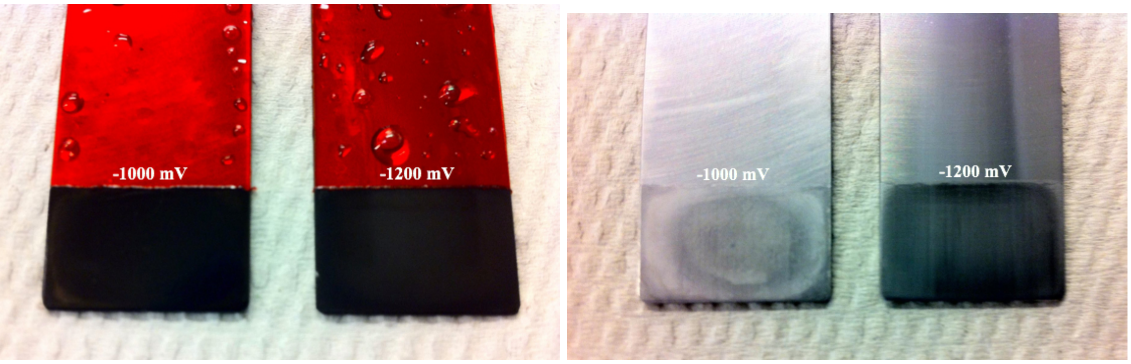
-1000 mV
-1200 mV
-1000 mV
-1200 mV

(e) Samples before post-treatment ($i_{AC} = 700 A/m^2$) (f) Samples after post-treatment ($i_{AC} = 700 A/m^2$)

Figure 4.13: *Samples exposed to different AC densities for 3 days (72h) at -1000 and -1200 mV respectively.*

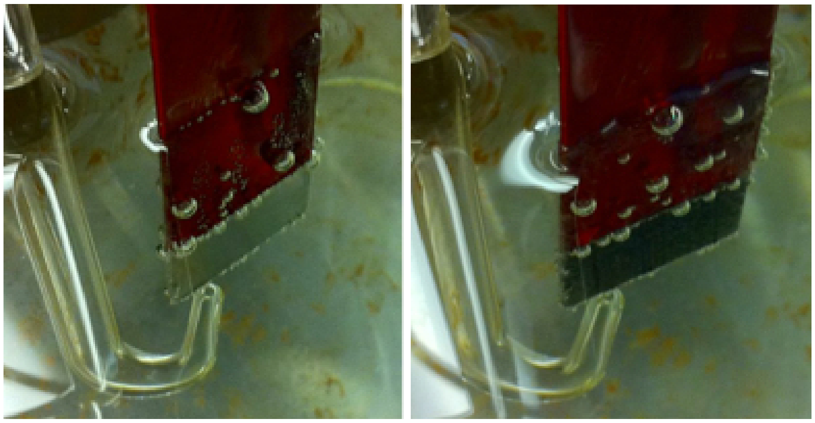

(a) 1 minute of exposure (b) 3 days of exposure

Figure 4.14: *Sample exposed to* $i_{AC} = 700A/m^2$ *at polarization* $-1200mV_{SCE}$

Figure 4.14 shows a sample exposed to $i_{AC} = 700A/m^2$ at polarization $-1200mV_{SCE}$ during different stages of the experiment. Heavy development of gas was visible immediately after initiation of experiment.

Microscopic

Figure 4.15 shows SEM surface characterization images of all AC densities tested in this experiment at the potentials -1000 and $-1200mV_{SCE}$. Figure B.6 through B.11 contains the complete catalogue of surface characterization images from polarization experiments.

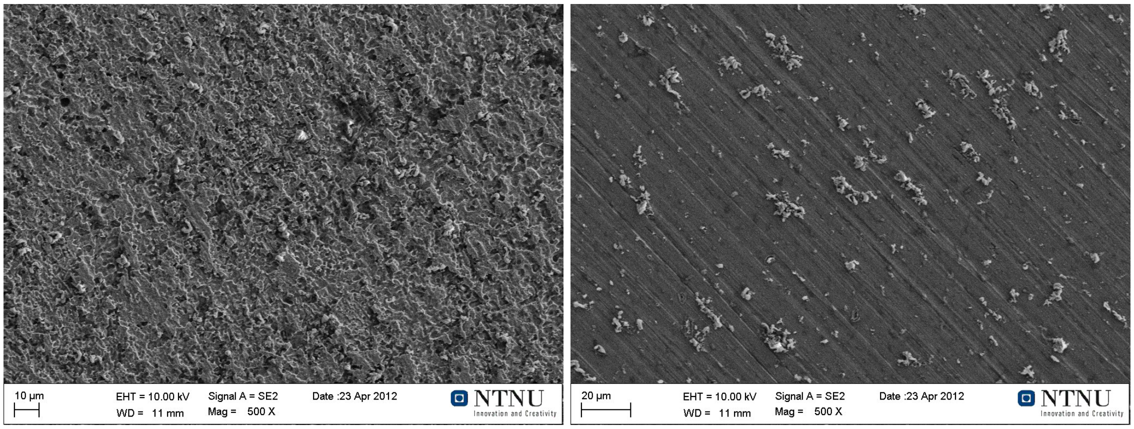
10 µm
EHT = 10.00 kV
WD = 11 mm
Signal A = SE2
Mag = 500 X
Date :23 Apr 2012
NTNU
Innovation and Creativity
20 µm
EHT = 10.00 kV
WD = 11 mm
Signal A = SE2
Mag = 500 X
Date :23 Apr 2012
NTNU
Innovation and Creativity

(a) $i_{AC} = 250A/m^2$, $E_x = -1000mV_{SCE}$, M = 500X (b) $i_{AC} = 250A/m^2$, $E_x = -1200mV_{SCE}$, M = 500X

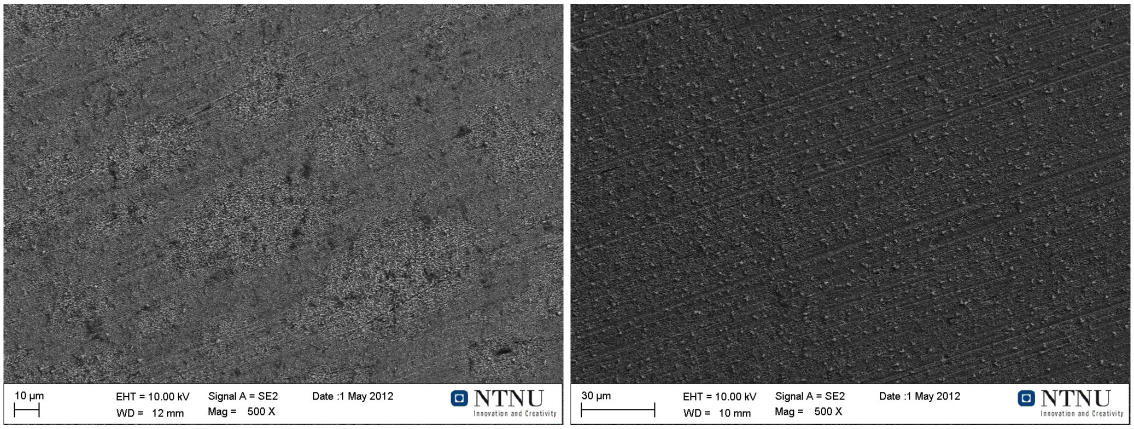
10 µm
EHT = 10.00 kV
WD = 12 mm
Signal A = SE2
Mag = 500 X
Date :1 May 2012
NTNU
Innovation and Creativity
30 µm
EHT = 10.00 kV
WD = 10 mm
Signal A = SE2
Mag = 500 X
Date :1 May 2012
NTNU
Innovation and Creativity

(c) $i_{AC} = 500A/m^2$, $E_x = -1000mV_{SCE}$, M = 500X (d) $i_{AC} = 500A/m^2$, $E_x = -1200mV_{SCE}$, M = 500X

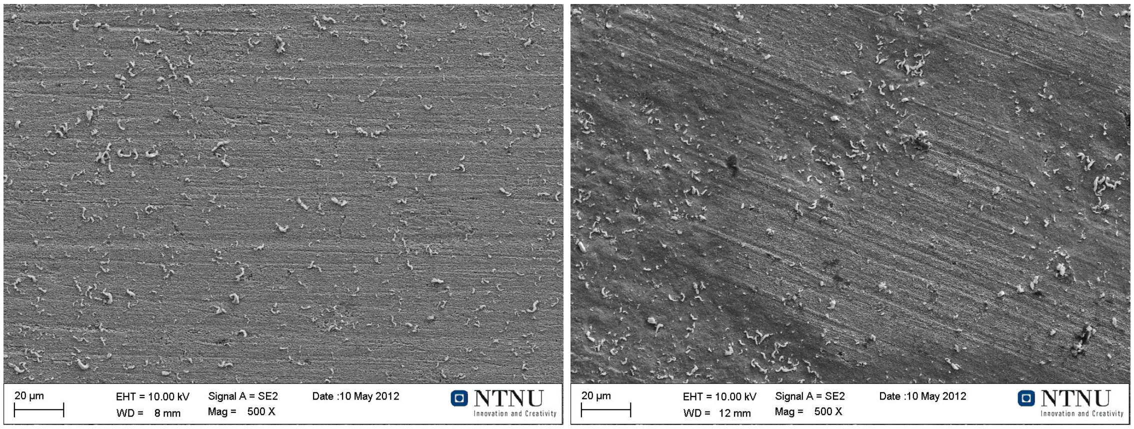
20 µm
EHT = 10.00 kV
WD = 8 mm
Signal A = SE2
Mag = 500 X
Date :10 May 2012
NTNU
Innovation and Creativity
20 µm
EHT = 10.00 kV
WD = 12 mm
Signal A = SE2
Mag = 500 X
Date :10 May 2012
NTNU
Innovation and Creativity

(e) $i_{AC} = 700A/m^2$, $E_x = -1000mV_{SCE}$, M = 500X (f) $i_{AC} = 700A/m^2$, $E_x = -1200mV_{SCE}$, M = 500X

Figure 4.15: *SEM images of all AC densities at -1000 and -1200* mV_{SCE}

4.3 Weight loss experiments - rotating WE

4.3.1 Corrosion current

The experiments were performed with a duration of 3 days (72h) at AC densities 100, 250, 500 and 700 A/m^2. In addition, separate experiments were performed at $i_{AC} = 0 A/m^2$. Figure 4.16 shows i_{AC} vs. i_{corr}. Key data is tabulated in table 4.5.

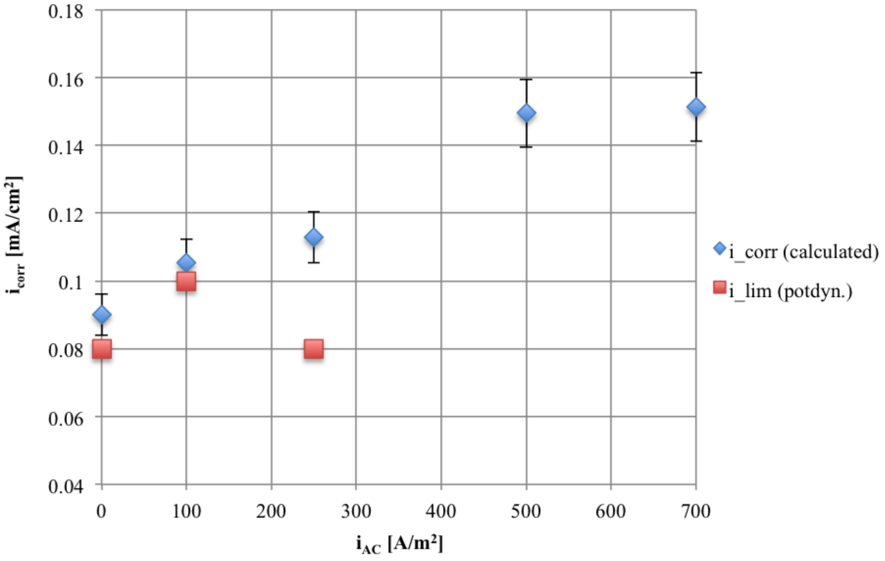

Figure 4.16: *i_{AC} vs. i_{corr}. Blue markers represent values of i_{corr} calculated from weight loss measurements. Red markers represent values of i_{lim} extracted graphically from polarization curves (figure 4.17). Standard deviation is plotted for weight loss measurements.*

Table 4.5

Key data

$i_{AC}[A/m^2]$	$\Delta m^{mean}_{corrected}$[mg]	$i^{WL}_{corr}[mA/cm^2]$	$i^{potdyn}_{lim}[mA/cm^2]$
0	20.3	0.09	0.08
100	23.8	0.11	0.10
250	24.6	0.11	0.08
500	33.3	0.15	-
700	34.2	0.15	-

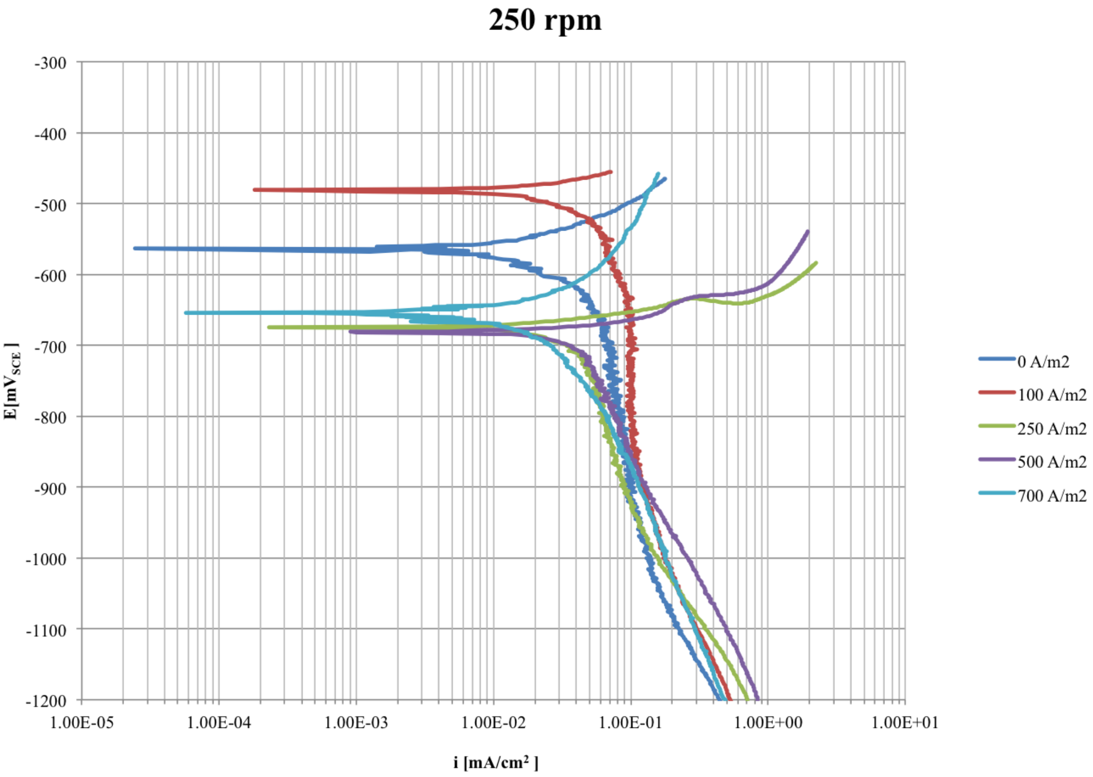

Figure 4.17: *Polarization curves, 250 rpm*

Table 4.6: *Curves were corrected for IR-drop in the electrolyte (R-value in table).* b_c *was corrected to only represent hydrogen reduction.*

Polarization data, 250 rpm				
$i_{AC}[A/m^2]$	E_{corr} [mV]	$R[\Omega]$	$i_{lim}[mA/cm^2]$	$b_c[mV/dec]$
0	-564	13	0.08	146
100	-484	10	0.10	163
250	-678	9	0.08	118
500	-685	9	-	177
700	-658	8	-	198

4.4 Summary of results

Stationary WE at E_{OC}

1. Corrosion rates increase as AC densities are increased. An approximately linear correlation between i_{AC} and i_{corr} has been established.

2. The corrosion potential decreases with increasing levels of AC. The initial potential drop once applying even low values of AC, is drastic. Further increasing i_{AC} leads to more negative potentials, but added effects are smaller than the initial one.

3. A dark/black iron oxide layer believed to consist of regular iron oxide and magnetite (Fe_3O_2 and Fe_3O_4), covers the entire sample surface once AC is applied. Brittle/non-protective properties. Increasing irregular texture/brittleness as AC densities are increased.

4. Surface characterization indicates pitting of increasing severity as AC densities are increased.

5. LPR (mean values) and weight loss measurements conform well. The corrosion current increases as a function of time after initial induction period.

Stationary WE at E_x

1. [E_x = -600 mV_{SCE}] Large CR for all AC densities.

2. [E_x = -800 mV_{SCE}] Pitting corrosion was detectable by the naked eye. Increasing CR as AC densities are increased.

3. [E_x = -1000 mV_{SCE}] AC densities 500 and 700 A/m^2 shows no/few signs of corrosion. At i_{AC} = 250 A/m^2 considerably more mass loss was documented.

4. [E_x = -1200 mV_{SCE}] Sample at i_{AC} = 250 A/m^2 is protected (no corrosion). For i_{AC} =500 and 700 A/m^2, corrosion is detected. Significantly more so at 700 A/m^2 than 500 A/m^2.

5. Surface characterization supports the recorded weight loss measurements. The dark/black iron oxide layer was present in all strings of the experiments except the one at i_{AC} = 250 A/m^2 and -1200 mV_{SCE}, where no such layer was formed.

Rotating WE at E_{OC}

1. $i_{corr} \approx i_{lim}$ for i_{AC} = 100 and 250 A/m^2.

2. i_{corr} is significantly larger for AC densities 500 and 700 A/m^2.

Chapter 5

Discussion

5.1 AC corrosion

Observed consequences of AC application on a system where low alloy carbon steel constitute the working electrode in 3.5 wt% NaCl electrolyte under open circuit conditions:

- Rapid formation of iron oxide surface layer on working electrode.
- Initial drastic drop in E_{corr}. Subsequent stabilization (still cathodic to E^0_{corr}).
- Apparent disappearance of i_{lim} at high AC densities under turbulent conditions.
- Development of gas bubbles on working electrode.
- Cyclic deposit/detachment behavior of corrosion products.
- Increasing CR as function of i_{AC}.
- Initial induction period ($\sim$10h) with constant CR.
- increasing CR as function of time after induction period.
- Pitting corrosion of increasing severity as function of i_{AC}.

In the following sections these observations will be discussed and a corrosion mechanism will be proposed. The consequences of polarizing the working electrode combined with applying AC will as well be assessed.

5.2 Corrosion mechanism

5.2.1 Iron oxide surface layer

The formation of a passive iron oxide surface layer on the carbon steel samples once exposed to AC, were reported for all AC densities (section 4.1.6). Its structure is porous and the layer is not believed to offer any barrier properties for protection against the electrolyte. The rate at which it was formed and its resulting thickness seemed to increase with increasing AC densities. The development of gas bubbles on the sample were initiated instantly after application of AC and became increasingly rapid as AC densities increased. This will in all likelihood contribute to the layers porosity. The iron oxide layer was formed both under stagnant conditions (activation control) and turbulent conditions (mixed control). The composition of the layer is believed to be a mix of magnetic iron oxide (Fe_3O_4, magnetite) and regular iron oxide (Fe_3O_2, rust). An alkalization process initiates when applying AC, causing the formation of this surface layer (magnetite forms at high levels of PH, ref. Pourbaix diagram in figure 2.14(a)). An enlarged cathodic half cycle of the sinusoidal potential in these initial minutes is believed to explain this.

5.2.2 Corrosion current

An approximately linear relationship between i_{AC} and i_{corr} (thereby also the CR), was established during the weight loss experiments at open circuit (section 4.1.1, figure 4.1). In figure 5.1, results from weight loss experiments have been combined with results from the specialization project by the author [2] from 2011.

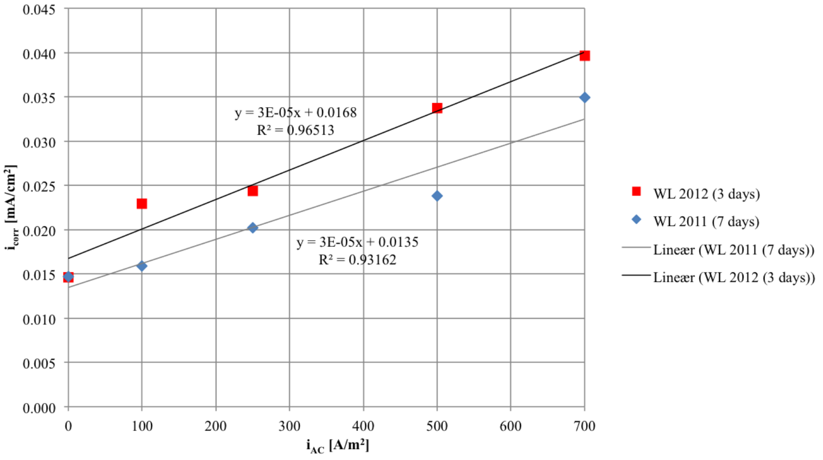

Figure 5.1: *i_{AC} vs. i_{corr}. Results based on total weight loss during entire exposure period. Red dots represent results from experiments performed for this thesis. Blue dots represent results from specialization project [2]. The R^2-value measures how well the data fit an ideal linear function ($R^2 = 1$).*

Experimental conditions were different in the two sets of experiments and may explain why values of i_{corr} are slightly higher in experiments from 2012 than in the ones from 2011 (stirring of the electrolyte, stricter temperature control).

$$\begin{aligned} i_{corr}(2012) &= 3 \cdot 10^{-5} \cdot i_{AC} + 0.017 \\ i_{corr}(2011) &= 3 \cdot 10^{-5} \cdot i_{AC} + 0.014 \end{aligned} \tag{5.1}$$

Equations 5.1 is the result of fitting linear trend lines to the data in figure 5.1.

LPR measurements

The LPR measurements were performed in order to surveil i_{corr} during the experiments. In the mentioned specialization project [2] from 2011, a manual potentiostat was used for such measurements. Comparing corrosion rates calculated from LPR measurements with data from weight loss measurements in these experiments resulted in large deviations ($i_{corr}^{LPR} << i_{corr}^{WL}$) and the technique was at that time considered to be inaccurate in systems with applied AC (figure D.1 in appendix D).

The circuit used in these experiments consist of one ordinary 3 electrode DC circuit and one AC circuit (section 3.4, figure 3.5). These are separated by a capacitor in the AC circuit and an inductance in the DC circuit to avoid mutual interference. The only task of the inductance in the DC circuit is in other words to filter out AC current so that only DC current flows in that circuit. Since the potentiostat only registers current in the DC circuit and values from the LPR measurements were considerably lower than actual values from weight loss measurements, it was suggested that i_{corr} included a non-Faradaic AC component (i_{AC}) according to equation 5.2. Instead of being solely devoted to charging the electrode double layer, it was at that time believed that a fraction ($\frac{i_{AC}}{C}$) of otherwise capacitive currents, directly contributed to the transfer of electrons at the electrode surface.

$$i_{corr} = i_{DC} + \frac{i_{AC}}{C} \tag{5.2}$$

This would have explained the observed values of i_{corr} since the potentiostat only would be able to register the i_{DC} component.

To investigate this further it was decided to implement an in-PC Gamry potentiostat into the circuit, which is the case in this paper. The reason for this was concerns regarding accuracy with the manual potentiostat. With a fully automated experiment scheme driven by the computer software, constant scan rates and high level accuracy measurements could be attained on an hourly basis. The results from these experiments (section 4.1.3, figure 4.1) show there is good correspondence between LPR- and weight loss measurements. This means that the LPR technique *is* a tool capable of quantifying AC corrosion. It further implies that equation 5.2 is invalid and that a relationship according to equation 5.3 applies.

$$i_{corr} = i_{DC}(i_{AC}) \tag{5.3}$$

Instead of actively contributing to i_{corr} as an addend, i_{AC} is believed to indirectly affect i_{DC} and cause it to increase. In other words, i_{corr} is purely a faradaic DC current and a function of i_{AC}.

Analyzing the the experiments (section 4.1.4, figure 4.5) reveals that i_{corr} is time dependent. After what seems to be an induction period of roughly 10h, i_{corr} starts to increase. This may be explained by the observed pitting corrosion of increasing severity as AC densities are increased (section 4.1.6, figure 4.8). The induction period is the required time span for negatively charged chloride ions (Cl^-) to migrate through the surface layer due to an excess positive charge generated by metal dissolution. As discussed in 5.2.1, the iron oxide layer which is formed when AC is applied, does not have strong barrier properties. Thereby it causes a proneness to localized corrosion attacks like pitting. Judging by the results presented in figure 4.5, this surface layer is able to withstand such migration for roughly 10h. This seemingly applies for all AC densities tested. After this induction period, pitting corrosion initiates and pit propagation explains the increasing i_{corr} (this has been illustrated in figure 5.2. The autocatalytic nature of pits is explained in section 2.2).

For ideally growing hemispherical pits, the relationship $i_{corr} \propto t^{\frac{1}{3}}$ where t is the time and n is a geometrical exponent has been determined to be valid (G.S. Frankel [17]). To investigate how the obtained experimental data behaved compared to such a relationship, the propagation phase of the experiment ($t \geq 10h$) was mathematically modeled to fit equation 5.4 through simple regression analysis.

$$i_{corr} = C \cdot t^n \tag{5.4}$$

Figure 5.3(b) illustrates the result of this analysis (on the form $\log i \propto n \log t$) while 5.3(a) contains the actual experimental data. Table 5.1 contains the estimated values of n and C.

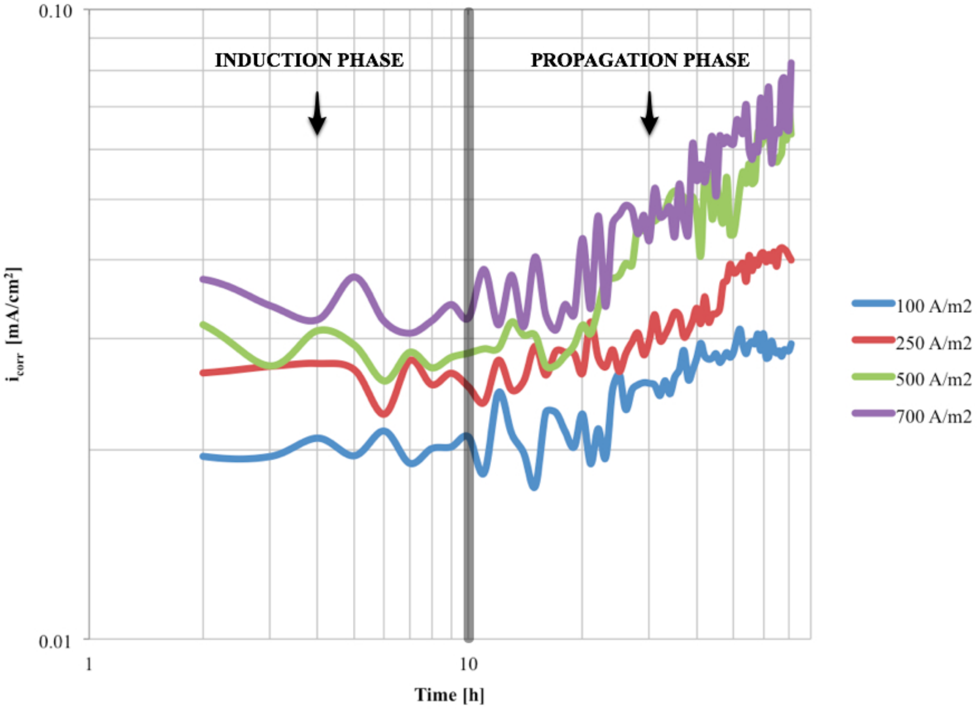

Figure 5.2: *The different stages of pitting.*

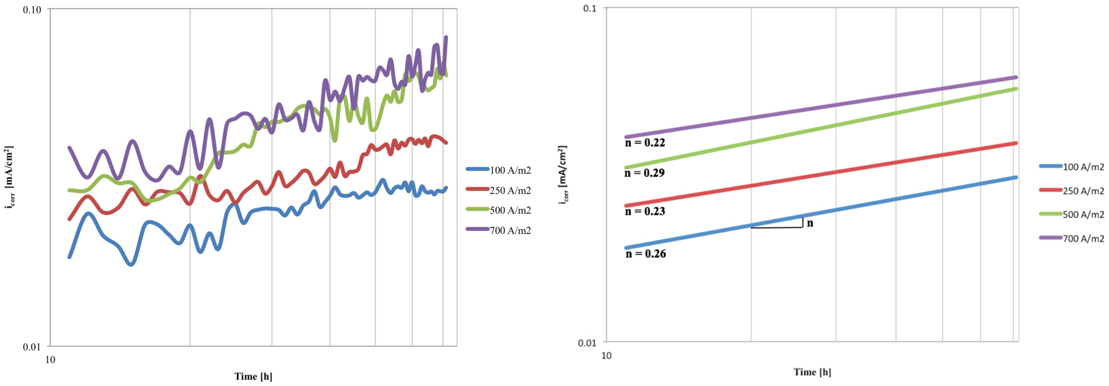

(a) Data from experiment

(b) Mathematically modeled

Figure 5.3: *i_{corr} vs. time. Logarithmical axes.*

Table 5.1

Regression analysis		
$i_{AC}[A/m^2]$	n	C
100	0.26	0.010
250	0.23	0.015
500	0.29	0.016
700	0.22	0.024

Relative to the ideal case of hemispherical pit propagation ($n = \frac{1}{3}$), these n-values appear to be well within the required margin to be deemed relevant for such an analysis. Comparing the estimations with surface characterization images (figure 4.8 and B.1 through B.5 in appendix B), there is good correspondence between pit geometry and estimated n-values. For example, one would expect n-values closer to the ideal value for AC densities 100 and $500A/m^2$ than 250 and $700A/m^2$. This is also the case, establishing conformity between the theory of pit propagation, the observed development of i_{corr} and surface characterization images.

5.2.3 Limiting current

Figure 4.4 shows polarization curves recorded at the end of each experiment (stationary WE, open circuit). At AC densities 500 and $700A/m^2$, the cathodic scan resulted in an oscillating potential-current relationship. Linear curves, like the ones for 100 and $250A/m^2$, were expected. In explaining this current behavior, the effects of AC on the working electrode needs to be assessed. In a small potential range around -900mV_{SCE} the current seems to be controlled by the limiting current for oxygen reduction. At roughly -1000mV_{SCE} the cathodic reaction switches, and becomes dominated by hydrogen reduction. This behavior is explained by the fact that oxygen reduction is diffusion controlled. High AC densities combined with increasingly negative potentials will initiate rapid development of hydrogen on the working electrode. The diffusion process is not fast enough and the system switches to activation control (hydrogen reduction). The iron oxide surface layer covering the working electrode is also believed to be a contributing factor to this development.

At roughly $-1100mV_{SCE}$, another limiting factor is encountered and the current does not seem to increase further. Due to the heavy development of hydrogen gas on the surface of the working electrode (figure 4.7(c)), a "hydrogen carpet" is created. This is believed to cover the surface so densely that further current exchange is blocked. The above described phenomena has been illustrated in the polarization curve for $i_{AC} = 700A/m^2$ in figure 5.4.

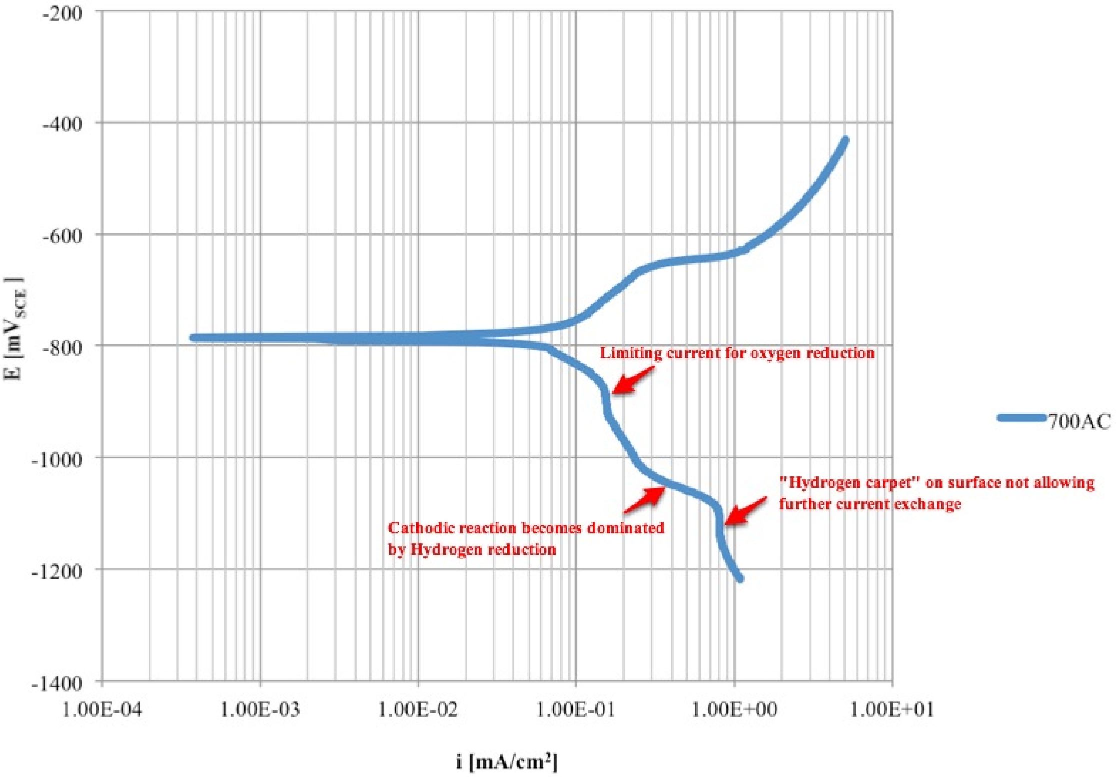

Figure 5.4: *Polarization curve - Stationary working electrode,* $i_{AC} = 700A/m^2$

Experiments using a rotating working electrode at open circuit (section 4.3) were performed in order to investigate the correlation between i_{corr} and i_{lim} for oxygen reduction and how these parameters act relative to each other under the influence of AC. Under normal circumstances (no applied AC), i_{corr} is expected to be equal to i_{lim} due to well established electrochemical considerations. Applying AC will alter traditional polarization data and at high levels of AC, the system seemingly becomes completely activation controlled (figure 4.17). Figure 4.16 displays combined results from weight loss measurements and potentiodynamic scans. The following observations were made:

$i_{corr} \approx i_{lim}$ for i_{AC} = 100 and 250 A/m^2.

i_{corr} is significantly larger for i_{AC} = 500 and 700 A/m^2

For $i_{AC} > 250A/m^2$, the diffusion of oxygen towards the working electrode surface becomes too slow, hydrogen reduction becomes the dominating cathodic reaction and the system switches completely to activation control.

After formation of the passive iron oxide surface layer during the initial alkalization process, the corrosion potential gradually stabilize at a level (hereby referred to as E_{corr}^{AC}) which is negative compared to the initial value at no AC (E_{corr}). The potential difference observed ($\Delta E = E_{corr}^{AC} - E_{corr}$) increases as applied AC density increases. This is illustrated in figure 5.5.

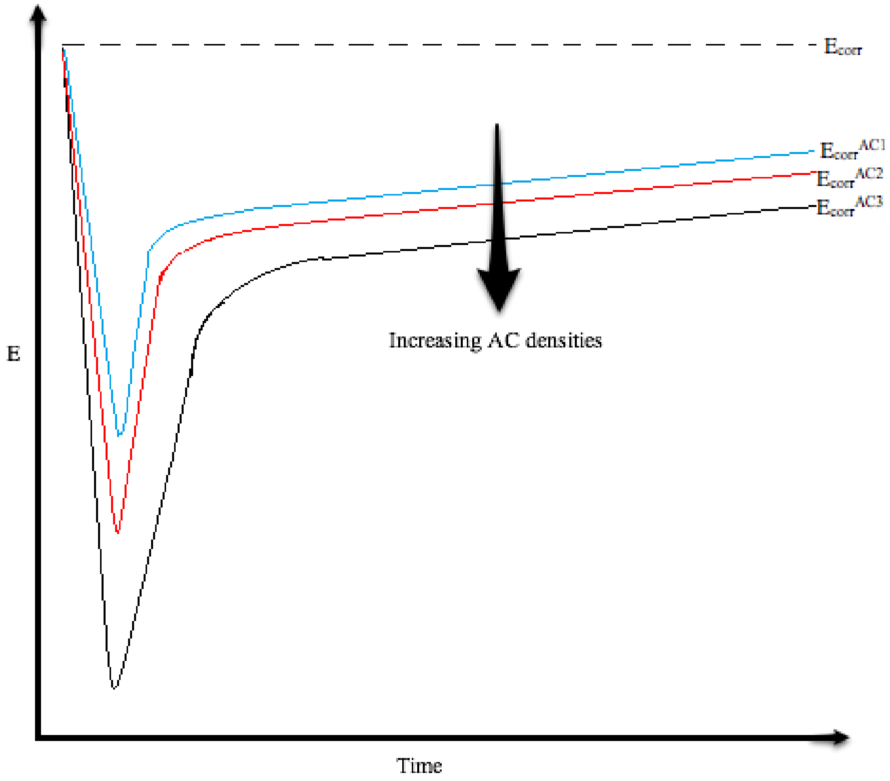

Figure 5.5: *Principle sketch of the potential development encountered as AC densities are increased.* $E_{corr} > E_{corr}^{AC1} > E_{corr}^{AC2} > E_{corr}^{AC3}$.

As AC densities of increasing magnitude are applied to the working electrode, the potential resultant amplitude will become larger. The anodic peak potential will in other words reach increasingly positive values. Pit initiation and growth takes place at a critical potential E_C and as the mentioned anodic peak potential become larger, this will occur at lower potentials. Hence, the corrosion potential will decrease. Furthermore, the porous iron oxide layer will increase the probability of localized corrosion attacks in an electrolyte including chloride ions due to already mentioned reasons. A synergy effect between the increasing anodic peak potential and an enlarged potential span of pitting is believed to explain the corrosion potential behavior.

Figure 5.6 shows how this mechanism affects i_{lim} for oxygen reduction in a system under mixed control. A natural consequence of the decreasing corrosion potential is a diminished region of active limiting current. When the potential becomes sufficiently cathodic, the system will switch to activation control. This is controlled by limits to the diffusion rate of oxygen. If the applied AC amplitude is sufficiently large, the system will in other words switch completely to activation control.

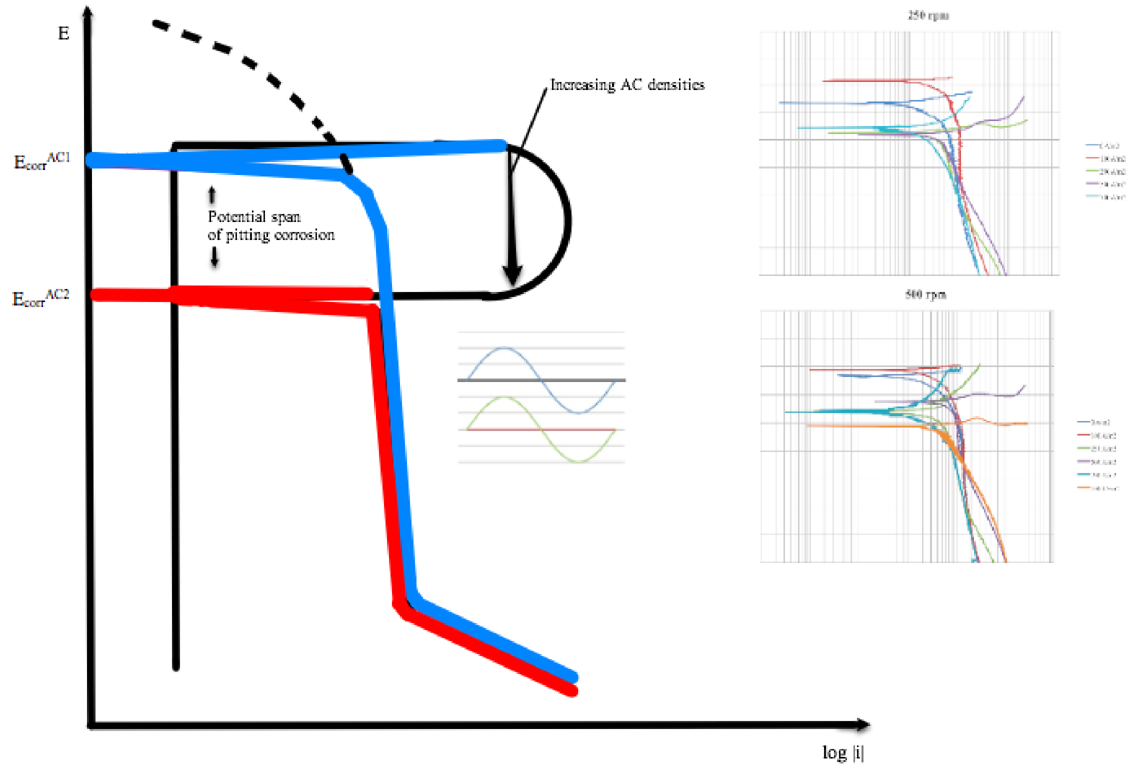
E
E_{corr}^{AC1}
E_{corr}^{AC2}
Increasing AC densities
Potential span of pitting corrosion
log |i|
250 rpm
500 rpm

Figure 5.6: *Principle sketch explaining the effect of AC on corrosion properties for a system under mixed control. The same principles are believed to be relevant for systems under full activation control with the exception of limiting currents.*

5.2.4 Polarized working electrode

The motivation behind performing such an experiment was mainly to investigate how applying AC would affect the corrosion process when polarized to the cathodic region of the potential scale (-1000 and $-1200 mV_{SCE}$). Proneness towards alkaline corrosion was suspected due to the alkaline environment created at the working electrode under such conditions. The main results from these experiments are given in figure 4.11 (tabulated in table 4.4). The complete catalogue of SEM surface characterization images are given in figure B.6 through B.11 in appendix B.

At $-600 mV_{SCE}$, large corrosion rates were expected for all AC densities. The results confirm this and figure 4.12 illustrates it. Anodic oxidation currents will be large and the working electrode is in the pitting region of the polarization curve. Surface characterization images indicates uniform corrosion. These observations are explained by the large corrosion rate under such conditions. Multiple pits propagating simultaneously, covering the entire surface will most likely make the surface appear this way.

At $-800 mV_{SCE}$, corrosion rates of increasing magnitude and pitting corrosion of increasing severity was expected as AC densities were increased. These expectations correspond well to reported results. The polarization potential is close to E_{corr} for the carbon steel being tested. As the anodic half cycle amplitude of the AC signal is increased, longer periods of time is spent above the critical potential of pitting (E_c) in each cycle. The driving force of pit propagation will as a consequence become larger. Pitting severity will increase and more metal loss is reported as a function of applied AC.

At $-1000 mV_{SCE}$, little or no metal loss was expected. In theory the working electrode should be cathodically protected against corrosion. For $i_{AC} = 250 A/m^2$ this was not the case and a corrosion rate of $0.32 mmy$ was reported. Surface characterization images (figure 4.15(a)) reveal pitting corrosion. No electrochemical explanation may be given for this observation and the result is believed to be caused by some error in that particular experiment. Possibly, KCl from the reference electrode leaked out into the electrolyte causing high concentrations of chloride ions at the working electrode. For the remaining AC densities tested, corrosion rates were negligible as expected.

At $-1200 mV_{SCE}$, heavy development of gas bubbles on the working electrode was observed (figure 4.14). The cathodic reaction ($2H_2O + 2e^- = H_2 + 2OH^-$) takes place and creates an alkaline environment at the working electrode. Since the driving force of the cathodic reaction is enlarged with increasing levels of applied AC, the level of alkalinity will also increase. Observed corrosion rates increase with increasing levels of AC. Surface characterization images corresponds well with these findings. Figure 4.15(f) shows a sample at $i_{AC} = 700 A/m^2$. The surface is partly etched, indicating an alkaline corrosion attack. Figure 5.7 sums up mentioned comments in a polarization curve recorded in experiments without any polarization.

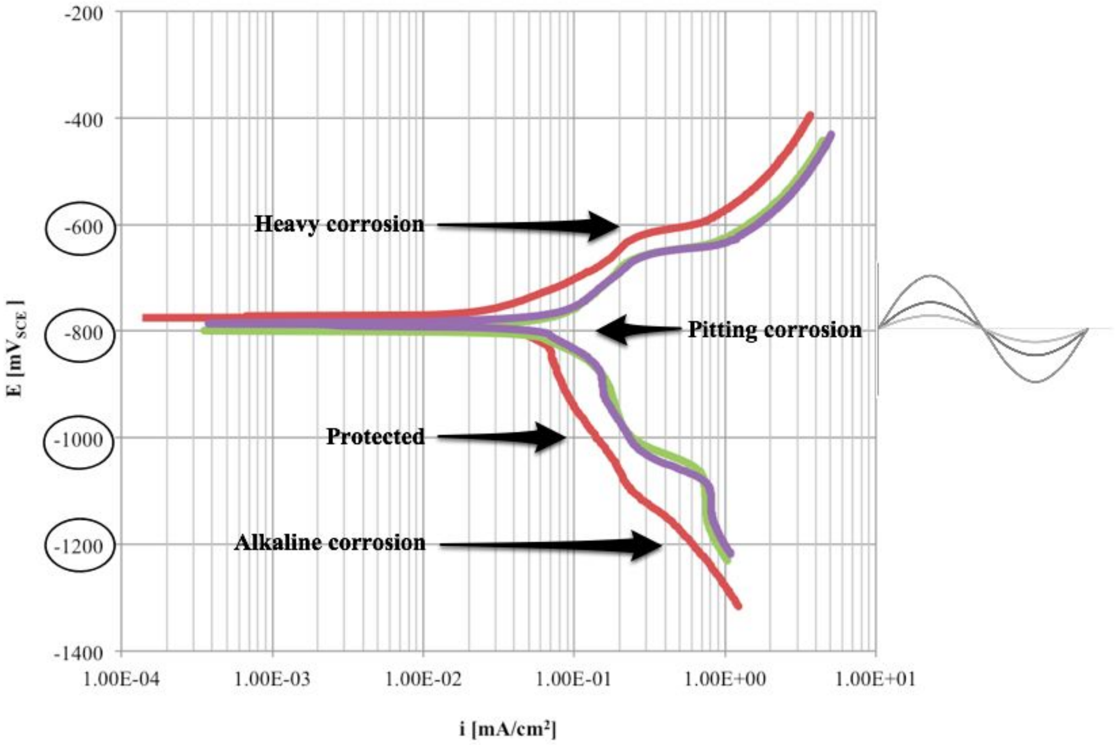

Figure 5.7: *Overview - different zones of polarization. Arrows and descriptions indicate observed corrosion types when polarized to those respective potentials for the duration of the experiment.*

Chapter 6

Conclusions

Corrosion kinetics of low alloy carbon steel in 3.5% NaCl electrolyte under the influence of AC was studied in this paper. The following conclusions could be made from analyzing the results:

1. Application of AC strongly influences corrosion kinetics in the system studied. An initial alkalization of the working electrode surface, enables the formation of a passive non-protective iron oxide surface layer consisting of combinations of regular iron oxide and magnetite (Fe_3O_2 and Fe_3O_4). The lack of barrier properties leads to a proneness towards localized corrosion attacks.

2. The corrosion current is believed to be purely a Faradaic DC-current acting as a function of applied level of AC ($i_{corr} = i_{DC}(i_{AC})$). Corrosion rates from LPR measurements coincide well with weight loss measurements and the technique is considered suitable for corrosion monitoring experiments with applied AC.

3. Pitting corrosion has been documented for all AC densities tested under open circuit conditions. After an initial induction period, pits start to propagate. Severity of pitting (measured in cumulative metal loss) increases as a function of i_{AC}. The mean corrosion current is approximately proportional to applied AC density ($i_{corr}^{mean} \propto i_{AC}$).

4. Under turbulent conditions (rotating WE), the cathodic reaction switches from mixed control to activation control for $i_{AC} > 250A/m^2$. The corrosion current increases significantly as a consequence of not being limited by diffusion of oxygen.

5. Alkaline corrosion has been documented for $i_{AC} > 250A/m^2$ for samples polarized to $-1200mV_{SCE}$. Increasing levels of applied AC increases the cathodic half cycle of the sinusoidal potential which leads to an enlarged level of basicity (increased PH). Alkaline corrosion of increasing severity is the result.

Chapter 7

Further work

1. An oscilloscope should be inserted into the DC circuit to investigate possible AC interference. Conclusions made in this paper rely on the assumption that the inductance of 10H filters out the entire AC signal. This assumption should be verified.

2. Further studies are required to clarify the effect of frequency of the applied AC signal (in this paper an AC signal of 50Hz was used for all experiments). Very few studies have been performed on this topic (section 2.1.1) and multiple assumptions should be verified. A signal generator combined with an amplifier should be implemented into the circuit and different AC/ frequency-combinations should be tested.

3. The properties of the iron oxide surface layer should be further studied. X-ray photoelectron spectroscopy (XPS) should be considered in order to verify composition, thickness and chemical/electronic state of the elements included in the layer.

4. Further experiments where the working electrode is polarized to cathodic potentials should be performed. Higher levels of AC ($i_{AC} > 700A/m^2$) should be applied and the observed alkaline corrosion should be thoroughly characterized.

References

[1] Nexans Norway. Direct electrical heating (deh) system [online]. 2011. Available from: `http://www.nexans.com/eservice/Navigate.nx?navigationId=276758` [cited 28.10.2011].

[2] Espen Strandheim. Ac induced corrosion of carbon steel in 3,5wt% nacl electrolyte. Specialization Project, NTNU, 2011.

[3] Shashi B. Lalvani Mark A. Pagano. Corrosion of mild steel subjected to alternating voltages in seawater. *Corrosion Science*, 36:127–140, 1994.

[4] S. Venkatachalam S. Z. Fernandez, S. G. Mehendale. Influence of frequency of alternating current on the electrochemical dissolution of mild steel and nickel. *Journal of applied electrochemistry*, 10:649–654, 1980.

[5] P.J. Gellings. The influence of alternating potential or current polarization on the corrosion rates of metals. *Electrochimica*, 7:19–24, 1962.

[6] Ingrid Stamnes. Ac-korrosjon av rørstål. Master's thesis, NTNU, 2010.

[7] Marco Ormellese Sara Goidanich, Luciano Lazzari. Ac corrosion. part 2: Parameters influencing corrosion rate. *Corrosion Science*, 52:916–922, 2009.

[8] Marco Ormellese Sara Goidanich, Luciano Lazzari. Ac corrosion. part 1: Effects on overpotentials of anodic and cathodic processes. *Corrosion Science*, 52:491–497, 2009.

[9] Sven Morten Hesjevik. Interim report - ac corrosion testing. Technical report, Statoil, 2009.

[10] Eirik Belland. Alternating current corrosion of carbon steel. Master's thesis, NTNU, 2011.

[11] W. F. Bogaerts R. W Bosch. A theoretical study of ac-induced corrosion considering diffusion phenomena. *Corrosion Science*, 40(2/3):323–336, 1998.

[12] NACE International Task Group 327. Ac corrosion state-of-the-art: Corrosion rate,

mechanism, and mitigation requirements. *NACE International. Publication 35110*, (24242), 2010.

[13] G. Zhang Shashi B. Lalvani. The corrosion of carbon steel in a chloride environment due to periodic voltage modulation: Part 1. *Corrosion Science*, 37(10):1567–1582, 1995.

[14] G. Zhang Shashi B. Lalvani. The corrosion of carbon steel in a chloride environment due to periodic voltage modulation: Part 2. *Corrosion Science*, 37(10):1583–1598, 1995.

[15] L. Lazzari M. Ormellese MP. Pedeferri F. Bolzoni, S. Goidanich. Laboratory testing on the influence of alternated current on steel corrosion. *NACE international. Houston, Texas - Corrosion 2004*, (04208), 2004.

[16] ASTM International. ASTM G1-03. *Standard practice for preparing, cleaning, and evaluating corrosion test specimens*, 2003.

[17] G.S. Frankel. Pitting corrosion of metals - a review of the critical factors. *Journal of The Electrochemical Society*, 145(6):2186–2197, 1998.

Appendices

Appendix A

Weight loss/ LPR - measurements

Table A.1: *Stationary WE, open circuit*

Experiment data - mean values						
Samples	$i_{AC}[A/m^2]$	Δm^{mean} [mg]	A_{exp} [cm^2]	CR_{WL} [mmy]	i_{corr}^{WL} [mA/cm^2]	i_{corr}^{LPR} [mA/cm^2]
1, 2	100	11.3	6.5	0.27	0.023	0.024
3, 4	250	12.1	6.5	0.28	0.024	0.031
5, 6	500	16.8	6.5	0.39	0.034	0.033
7, 8	700	17.3	5.7	0.46	0.040	0.044

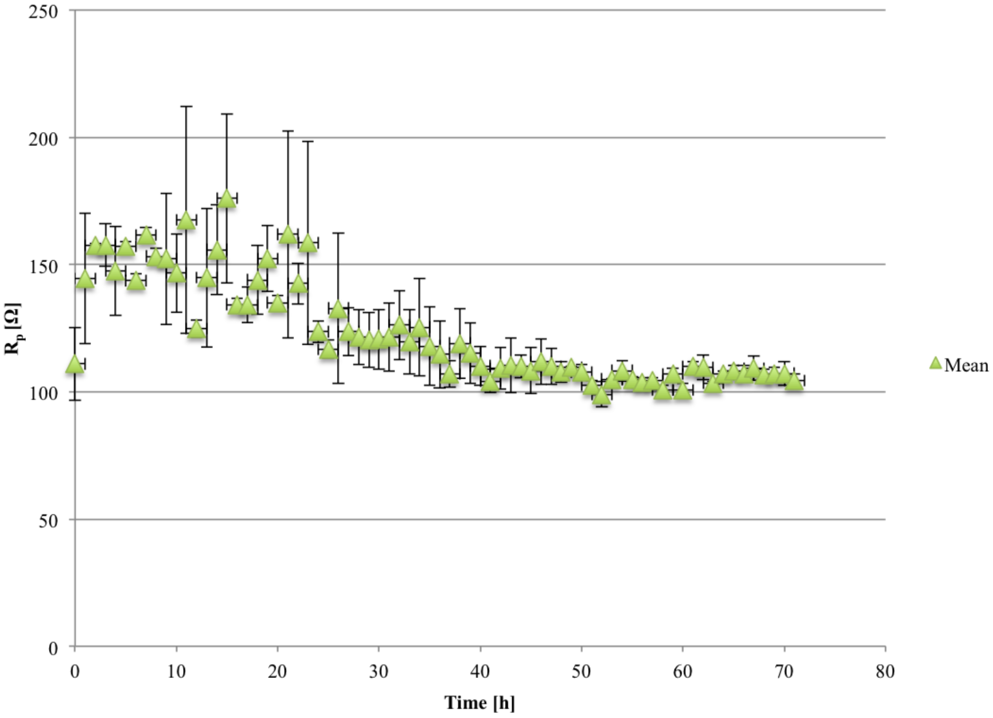

(a) $i_{AC} = 100 A/m^2$

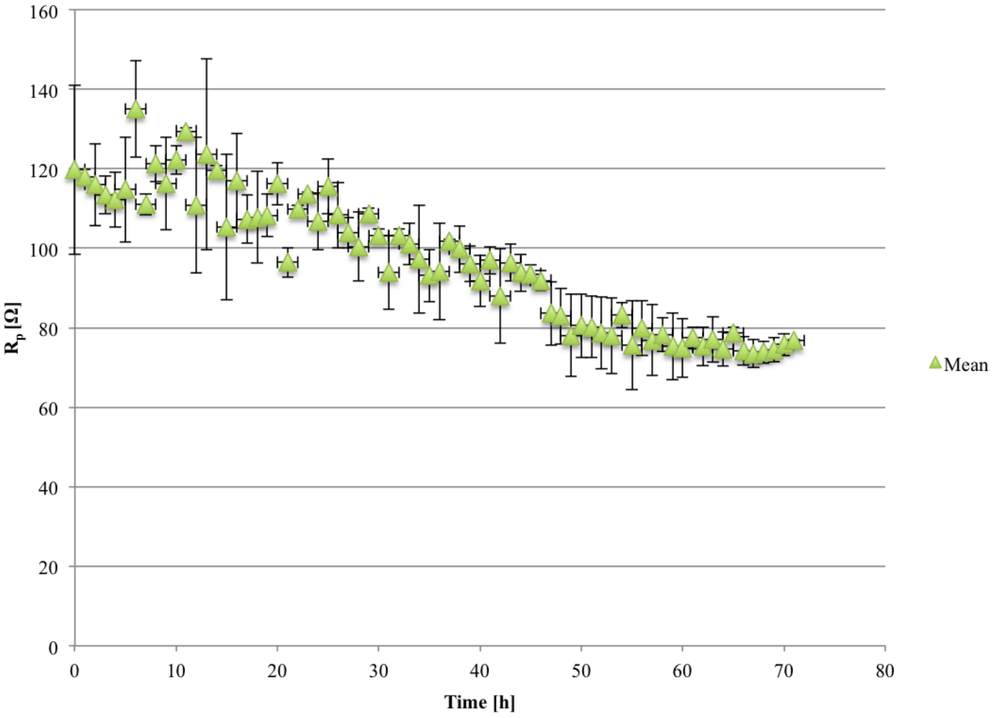

(b) $i_{AC} = 250 A/m^2$

Figure A.1: *R_p vs. time (with standard deviation plotted).*

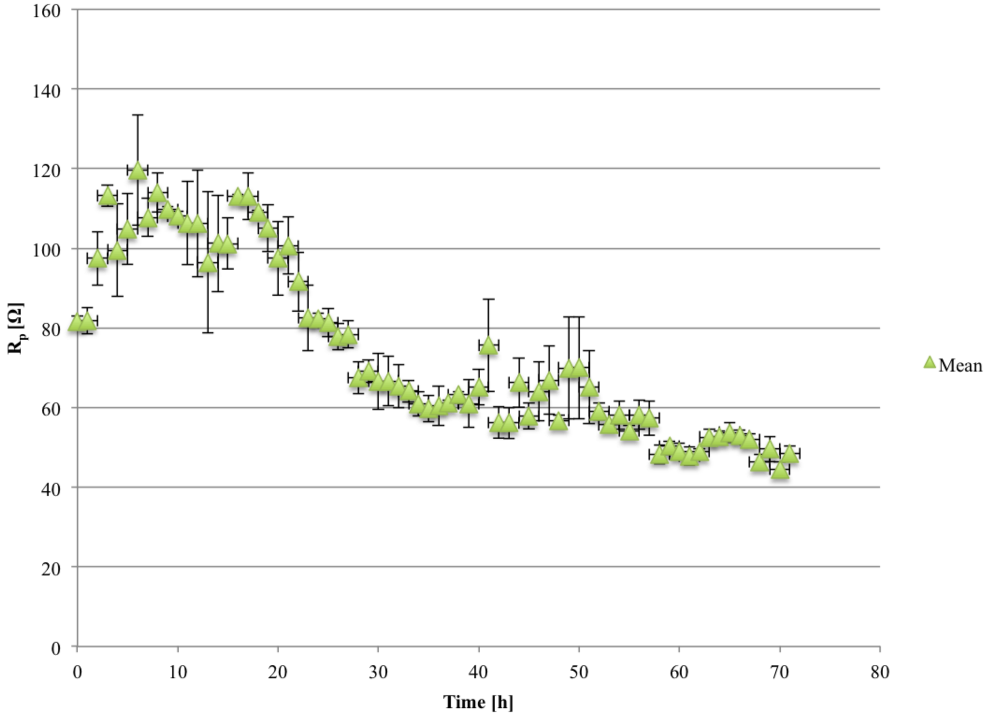

(a) $i_{AC} = 500A/m^2$

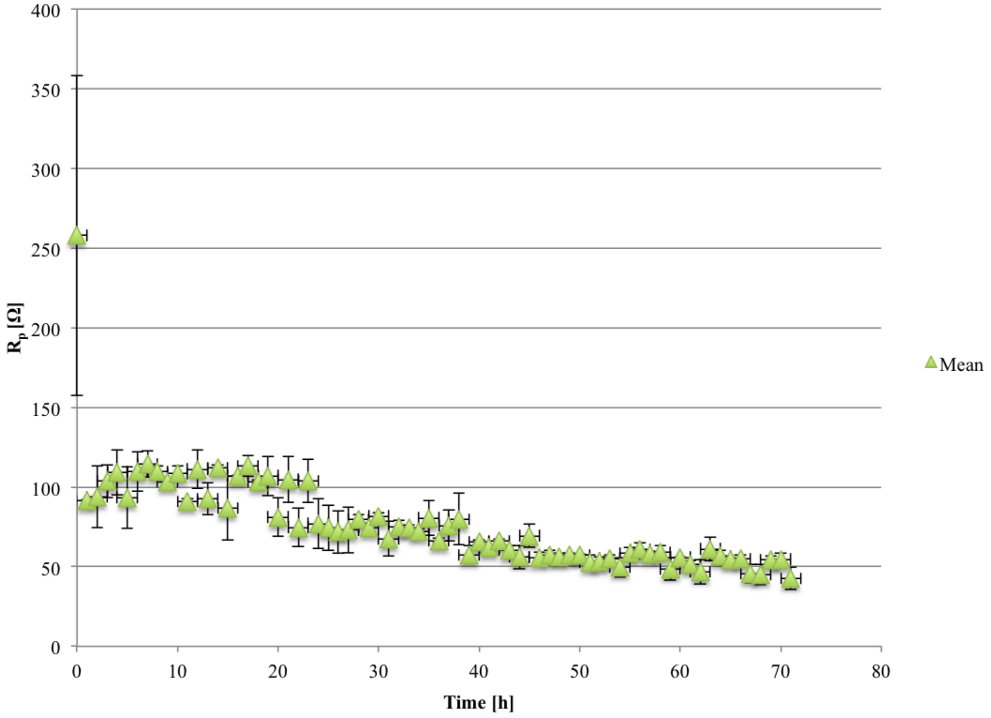

(b) $i_{AC} = 700A/m^2$

Figure A.2: *R_p vs. time (with standard deviation plotted).*

Appendix B

Surface characterization

This appendix contains the complete catalogue of surface characterization images captured throughout this experimental work. These images were produced by the use of a scanning electron microscope (SEM).

Figure B.1 through B.5 Experiment: Weight loss, stationary WE, open circuit (E_{OC})

Figure B.6 through B.11 Experiment: Weight loss, stationary WE, fixed potentials (E_x)

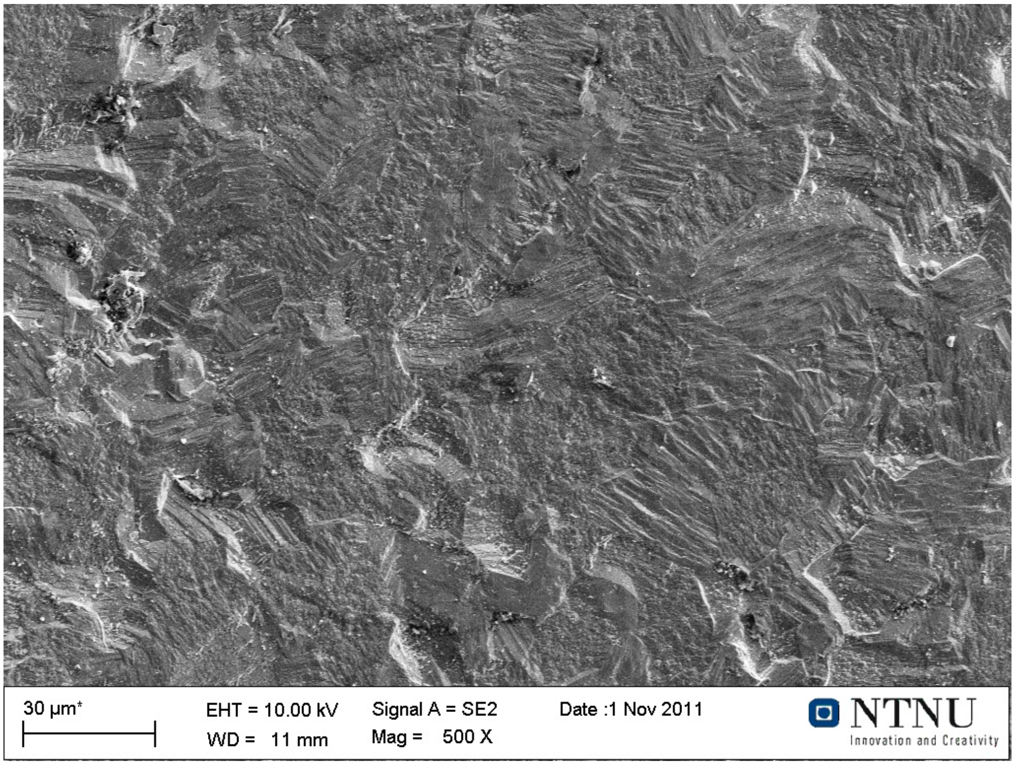
30 µm*
EHT = 10.00 kV
WD = 11 mm
Signal A = SE2
Mag = 500 X
Date :1 Nov 2011
NTNU
Innovation and Creativity

(a) $i_{AC} = 0A/m^2$, M = 500X

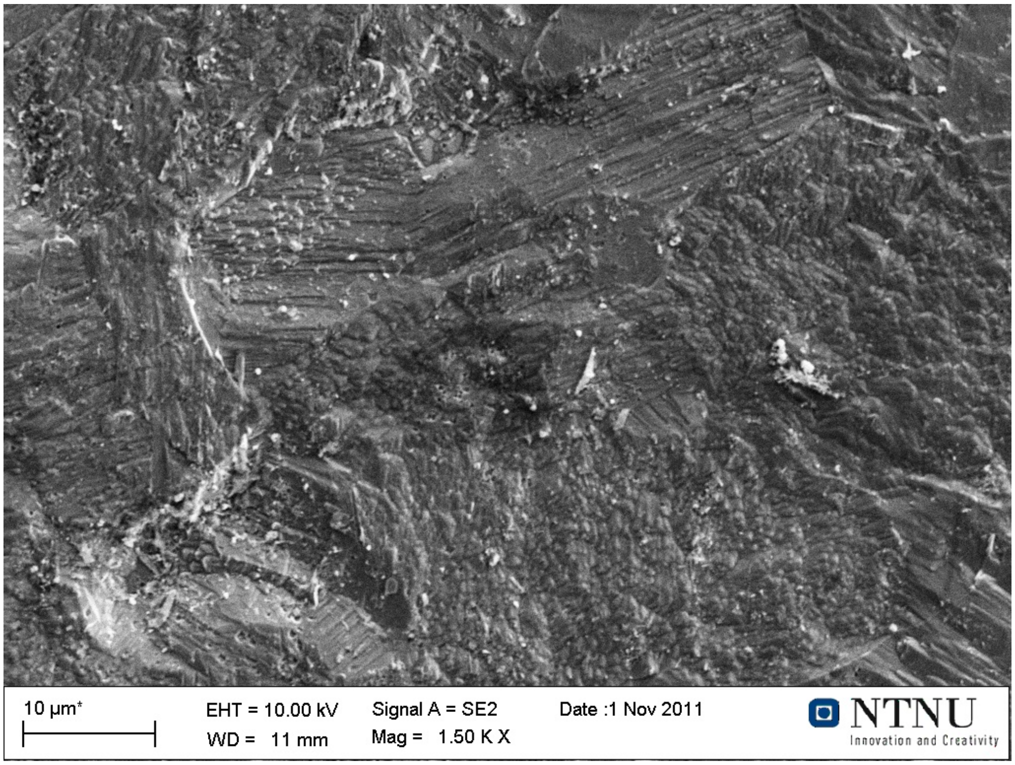
10 µm*
EHT = 10.00 kV
WD = 11 mm
Signal A = SE2
Mag = 1.50 K X
Date :1 Nov 2011
NTNU
Innovation and Creativity

(b) $i_{AC} = 0A/m^2$, M = 1500X

Figure B.1: *SEM*, $i_{AC} = 0A/m^2$

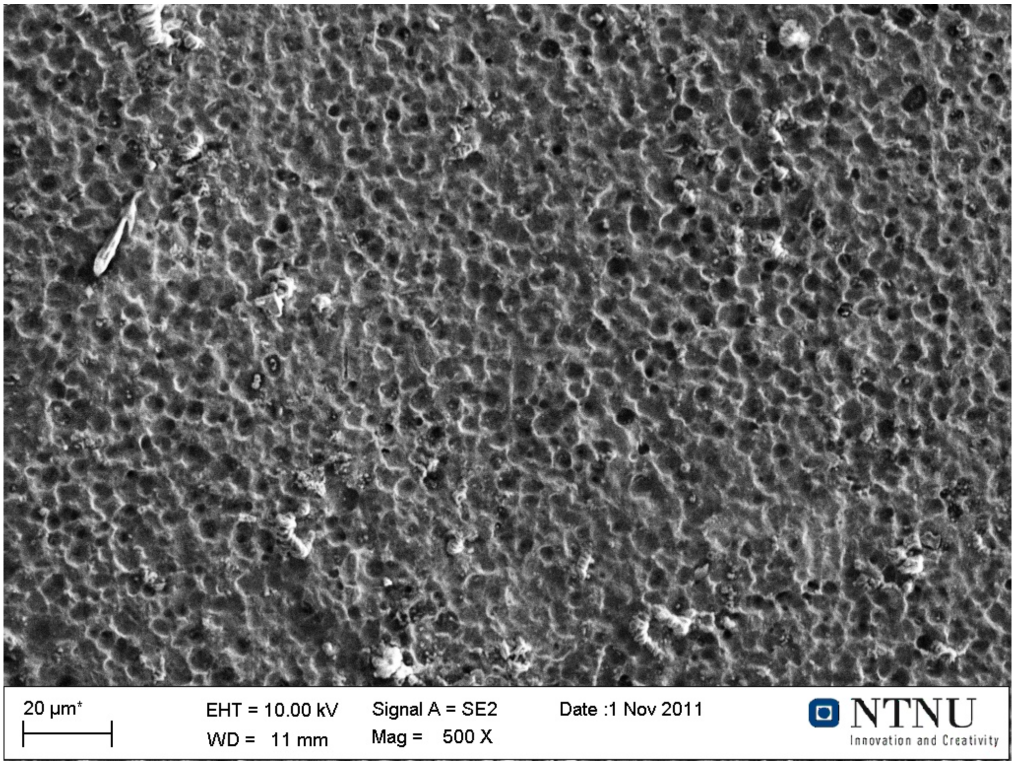
20 µm*
EHT = 10.00 kV
WD = 11 mm
Signal A = SE2
Mag = 500 X
Date :1 Nov 2011
NTNU
Innovation and Creativity

(a) $i_{AC} = 100A/m^2$, M = 500X

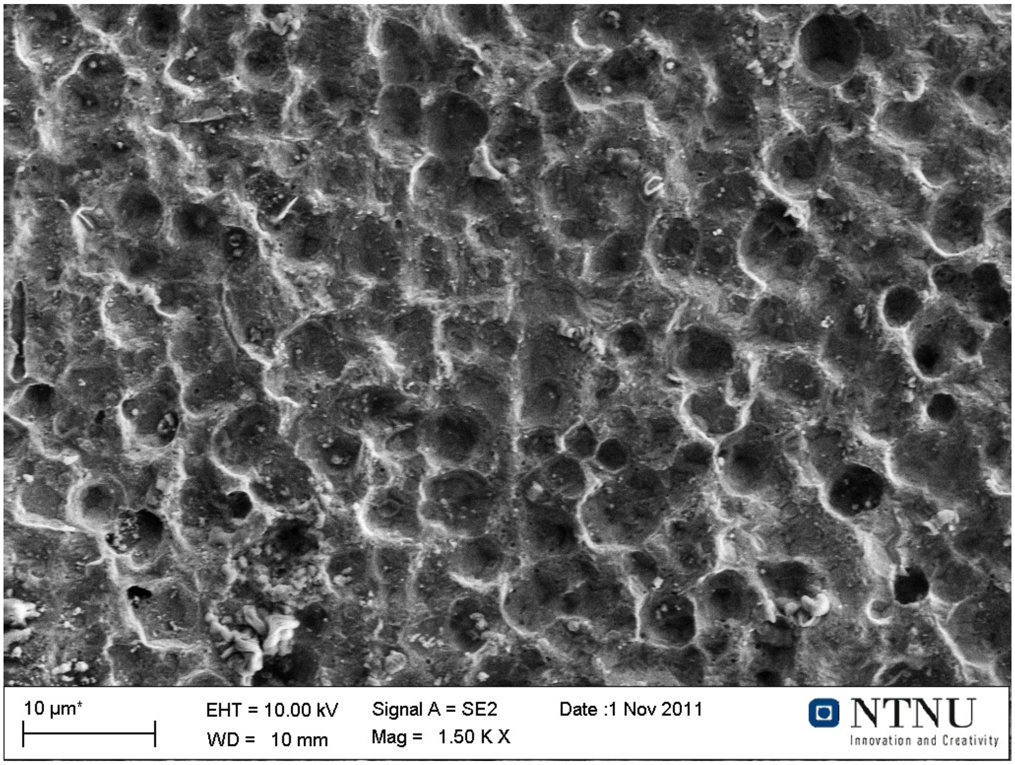
10 µm*
EHT = 10.00 kV
WD = 10 mm
Signal A = SE2
Mag = 1.50 K X
Date :1 Nov 2011
NTNU
Innovation and Creativity

(b) $i_{AC} = 100A/m^2$, M = 1500X

Figure B.2: *SEM,* $i_{AC} = 100A/m^2$

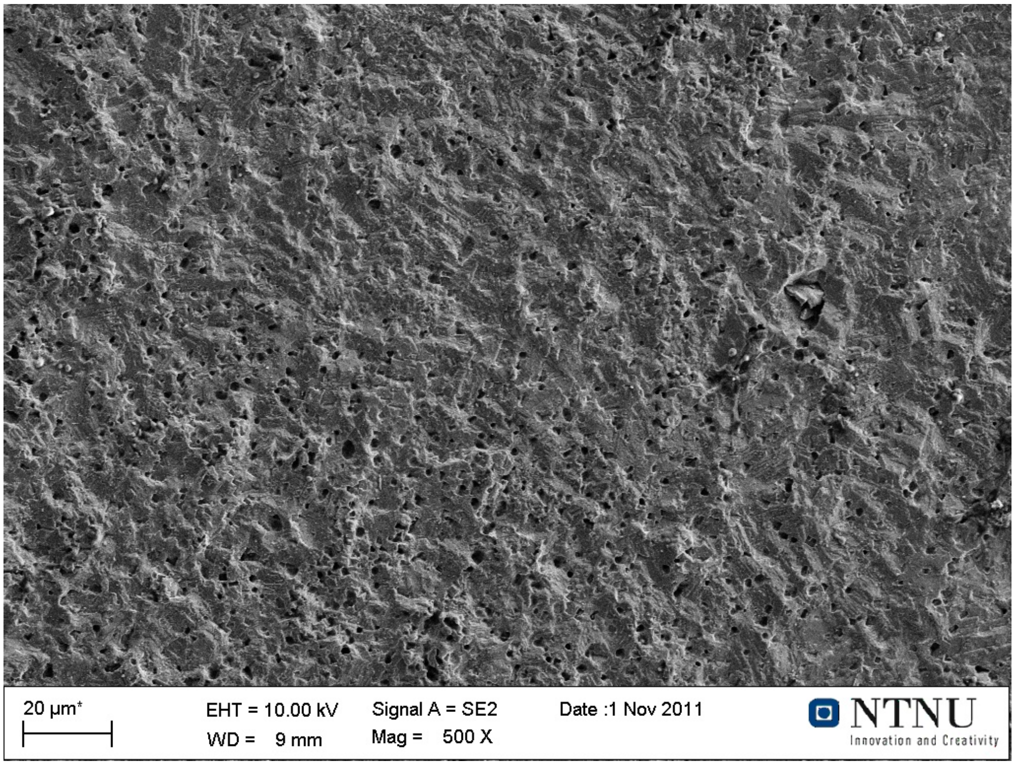
20 µm*
EHT = 10.00 kV
WD = 9 mm
Signal A = SE2
Mag = 500 X
Date :1 Nov 2011
NTNU
Innovation and Creativity

(a) $i_{AC} = 250 A/m^2$, M = 500X

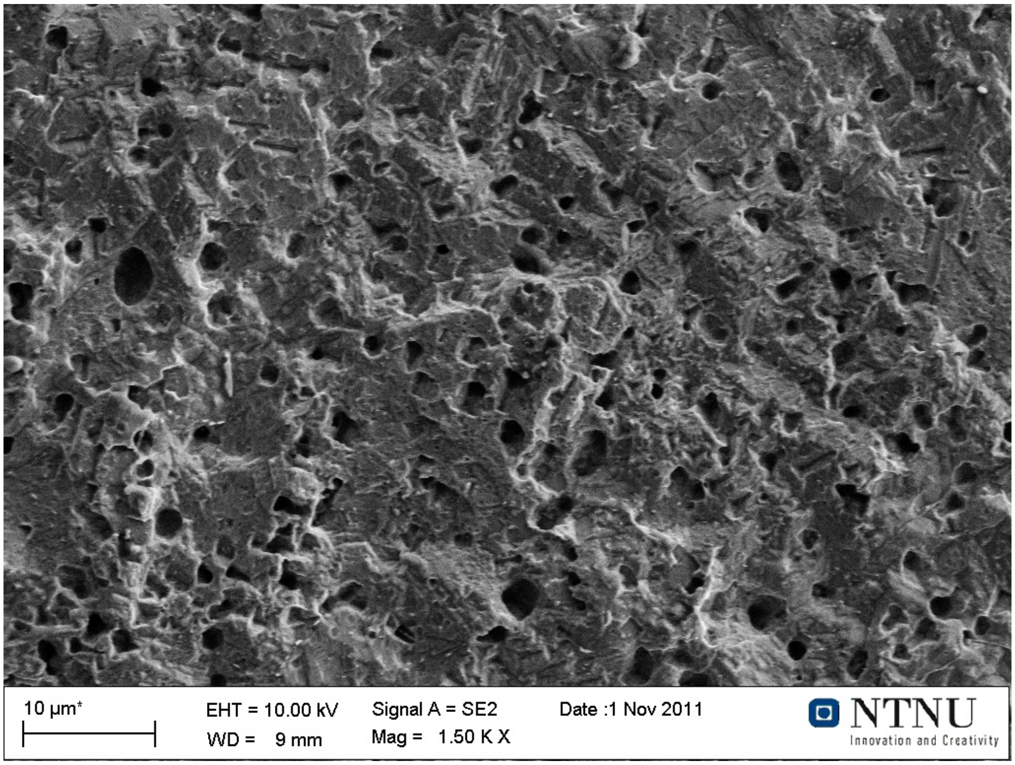
10 µm*
EHT = 10.00 kV
WD = 9 mm
Signal A = SE2
Mag = 1.50 K X
Date :1 Nov 2011
NTNU
Innovation and Creativity

(b) $i_{AC} = 250 A/m^2$, M = 1500X

Figure B.3: *SEM*, $i_{AC} = 250 A/m^2$

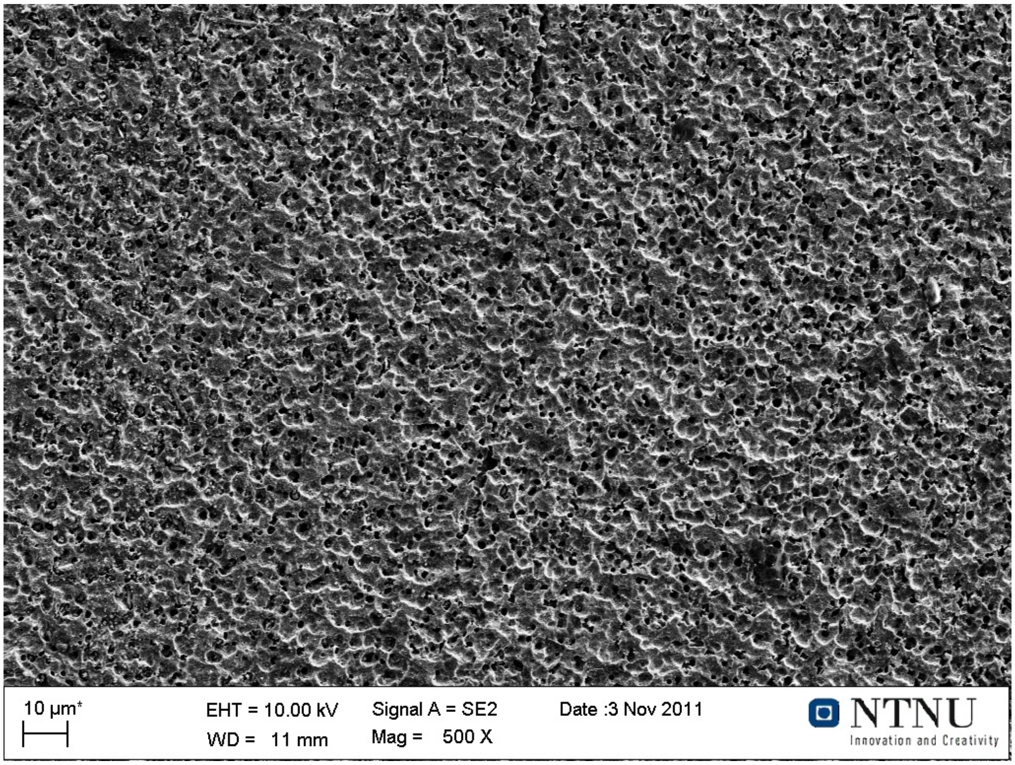
10 µm*
EHT = 10.00 kV
WD = 11 mm
Signal A = SE2
Mag = 500 X
Date :3 Nov 2011
NTNU
Innovation and Creativity

(a) $i_{AC} = 500A/m^2$, M = 500X

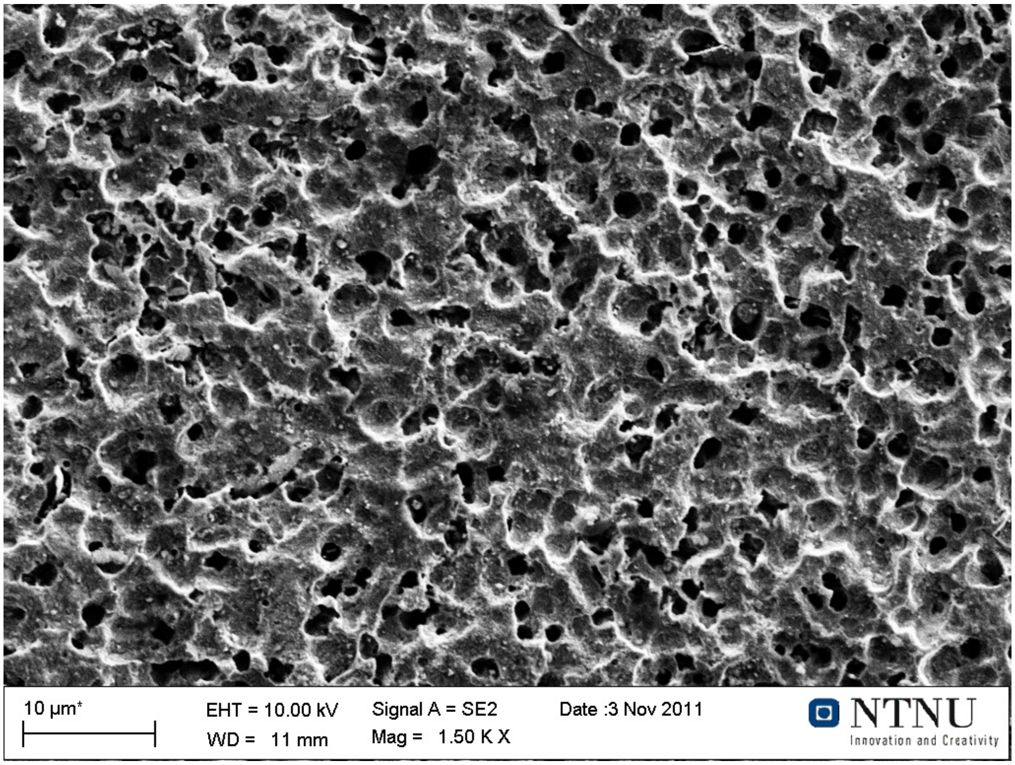
10 µm*
EHT = 10.00 kV
WD = 11 mm
Signal A = SE2
Mag = 1.50 K X
Date :3 Nov 2011
NTNU
Innovation and Creativity

(b) $i_{AC} = 500A/m^2$, M = 1500X

Figure B.4: *SEM*, $i_{AC} = 500A/m^2$

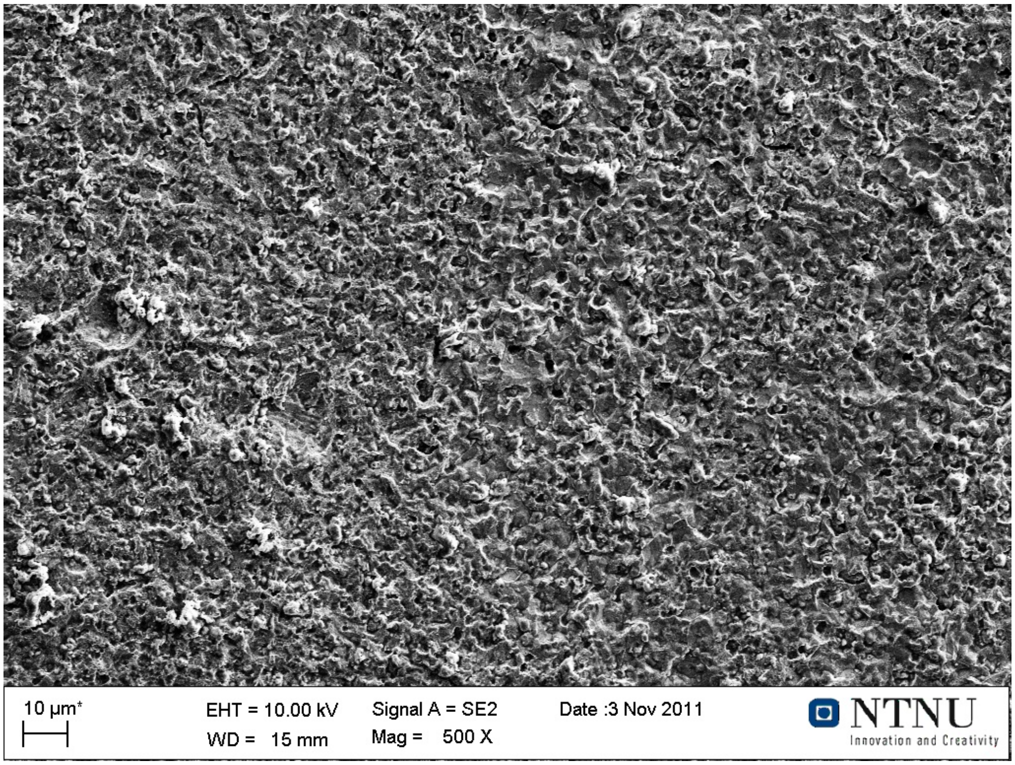
10 µm*
EHT = 10.00 kV
WD = 15 mm
Signal A = SE2
Mag = 500 X
Date :3 Nov 2011
NTNU
Innovation and Creativity

(a) $i_{AC} = 700A/m^2$, M = 500X

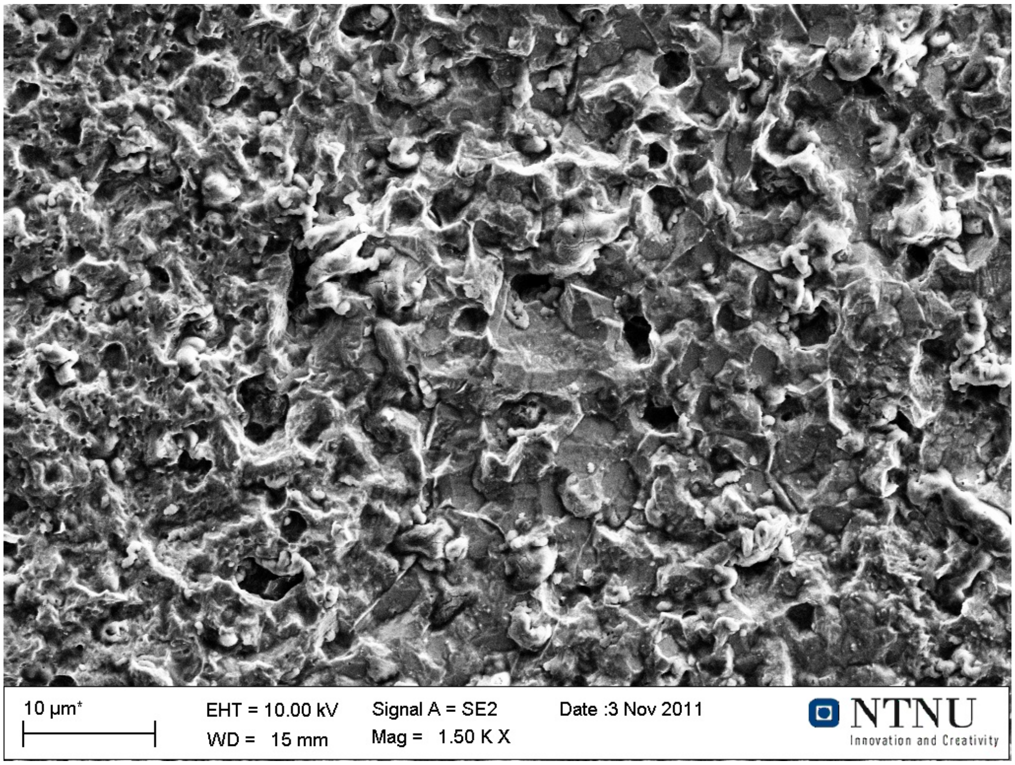
10 µm*
EHT = 10.00 kV
WD = 15 mm
Signal A = SE2
Mag = 1.50 K X
Date :3 Nov 2011
NTNU
Innovation and Creativity

(b) $i_{AC} = 700A/m^2$, M = 1500X

Figure B.5: *SEM,* $i_{AC} = 700A/m^2$

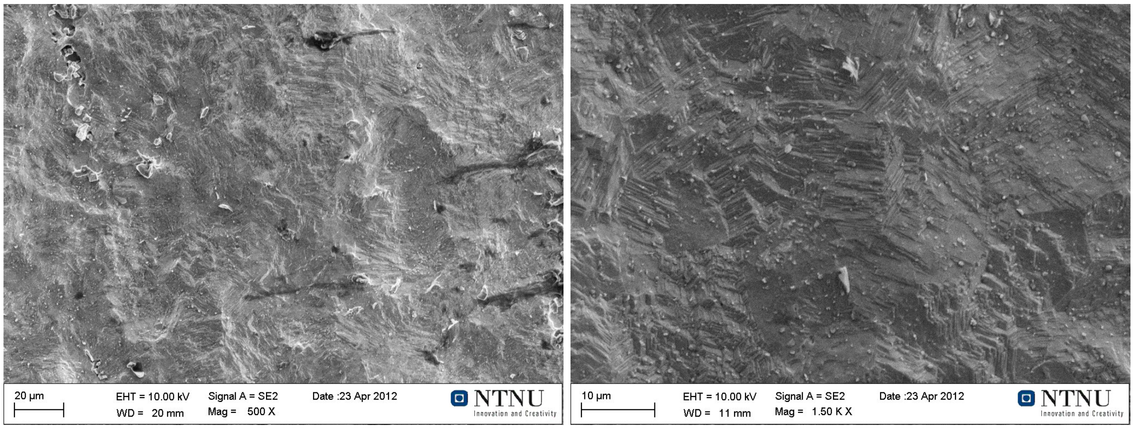
20 µm
EHT = 10.00 kV
WD = 20 mm
Signal A = SE2
Mag = 500 X
Date :23 Apr 2012
NTNU
Innovation and Creativity
10 µm
EHT = 10.00 kV
WD = 11 mm
Signal A = SE2
Mag = 1.50 K X
Date :23 Apr 2012
NTNU
Innovation and Creativity

(a) $E_x = -600mV_{SCE}$, M = 500X

(b) $E_x = -600mV_{SCE}$, M = 1500X

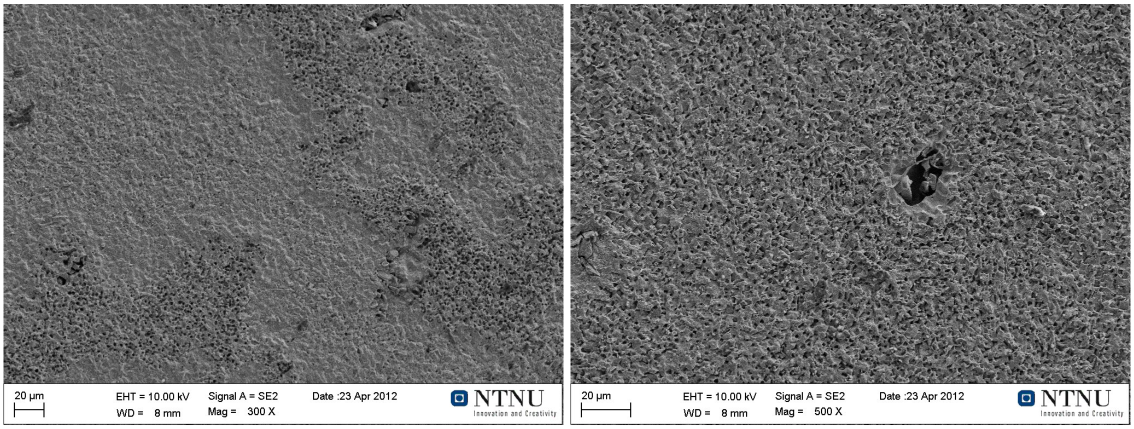
20 µm
EHT = 10.00 kV
WD = 8 mm
Signal A = SE2
Mag = 300 X
Date :23 Apr 2012
NTNU
Innovation and Creativity
20 µm
EHT = 10.00 kV
WD = 8 mm
Signal A = SE2
Mag = 500 X
Date :23 Apr 2012
NTNU
Innovation and Creativity

(c) $E_x = -800mV_{SCE}$, M = 300X

(d) $E_x = -800mV_{SCE}$, M = 500X

Figure B.6: *SEM*, $i_{AC} = 250A/m^2$

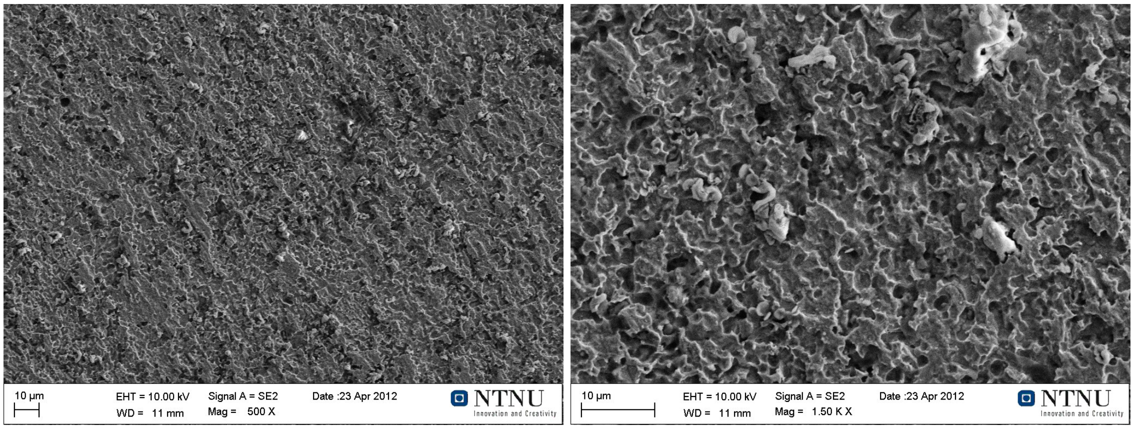
10 µm
EHT = 10.00 kV
WD = 11 mm
Signal A = SE2
Mag = 500 X
Date :23 Apr 2012
NTNU
Innovation and Creativity
10 µm
EHT = 10.00 kV
WD = 11 mm
Signal A = SE2
Mag = 1.50 K X
Date :23 Apr 2012
NTNU
Innovation and Creativity

(a) $E_x = -1000 mV_{SCE}$, M = 500X (b) $E_x = -1000 mV_{SCE}$, M = 1500X

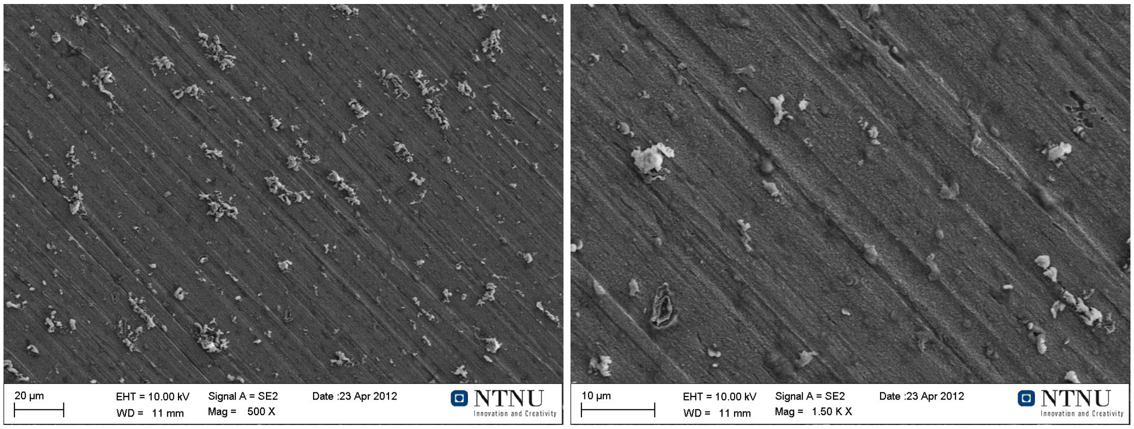
20 µm
EHT = 10.00 kV
WD = 11 mm
Signal A = SE2
Mag = 500 X
Date :23 Apr 2012
NTNU
Innovation and Creativity
10 µm
EHT = 10.00 kV
WD = 11 mm
Signal A = SE2
Mag = 1.50 K X
Date :23 Apr 2012
NTNU
Innovation and Creativity

(c) $E_x = -1200 mV_{SCE}$, M = 500X (d) $E_x = -1200 mV_{SCE}$, M = 1500X

Figure B.7: *SEM,* $i_{AC} = 250 A/m^2$

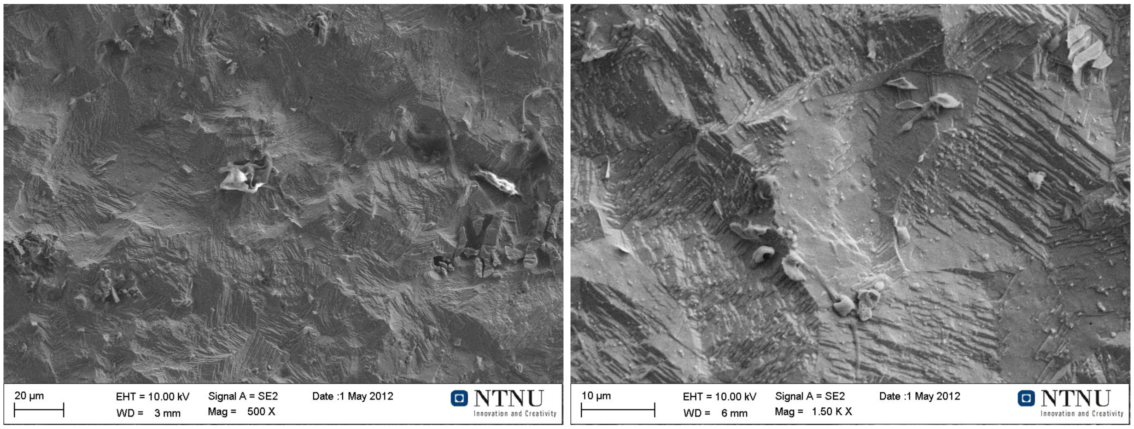
20 µm
EHT = 10.00 kV
WD = 3 mm
Signal A = SE2
Mag = 500 X
Date :1 May 2012
NTNU
Innovation and Creativity
10 µm
EHT = 10.00 kV
WD = 6 mm
Signal A = SE2
Mag = 1.50 K X
Date :1 May 2012
NTNU
Innovation and Creativity

(a) $E_x = -600mV_{SCE}$, M = 500X (b) $E_x = -600mV_{SCE}$, M = 1500X

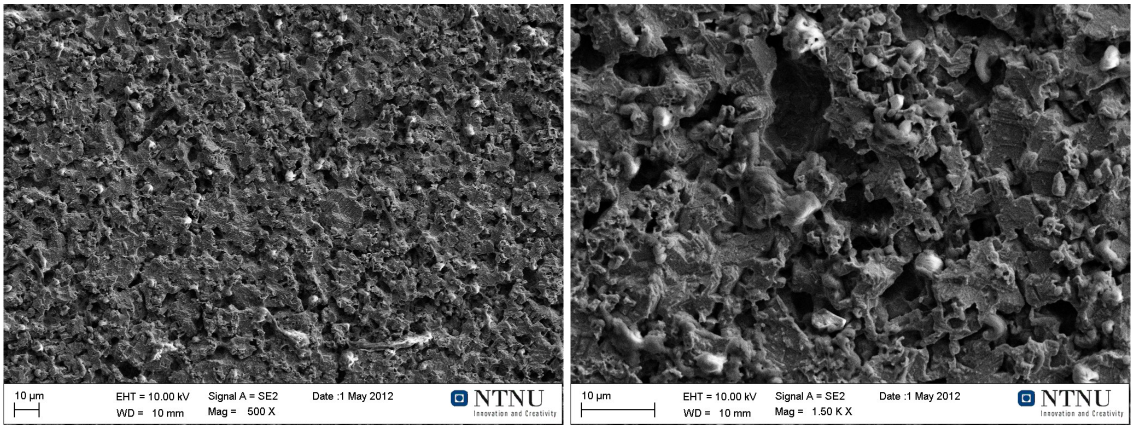
10 µm
EHT = 10.00 kV
WD = 10 mm
Signal A = SE2
Mag = 500 X
Date :1 May 2012
NTNU
Innovation and Creativity
10 µm
EHT = 10.00 kV
WD = 10 mm
Signal A = SE2
Mag = 1.50 K X
Date :1 May 2012
NTNU
Innovation and Creativity

(c) $E_x = -800mV_{SCE}$, M = 500X (d) $E_x = -800mV_{SCE}$, M = 1500X

Figure B.8: *SEM*, $i_{AC} = 500A/m^2$

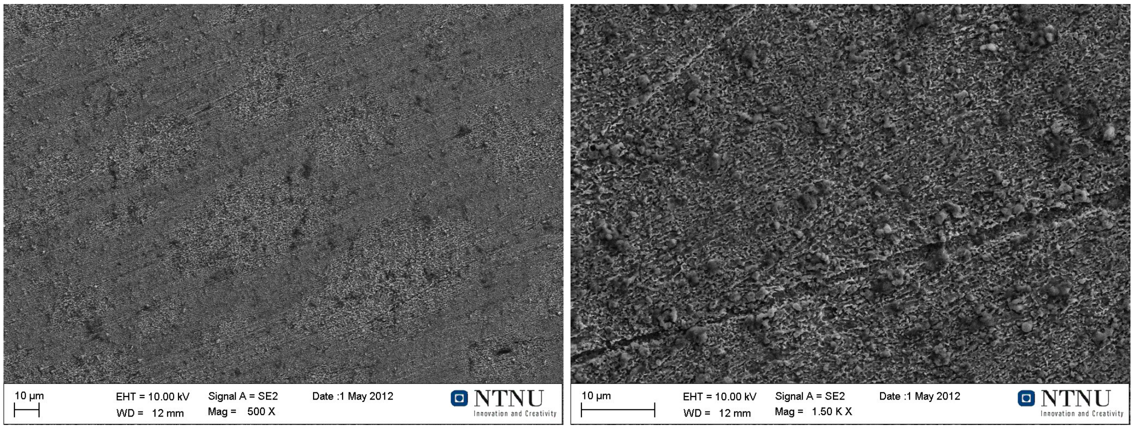
10 µm
EHT = 10.00 kV
WD = 12 mm
Signal A = SE2
Mag = 500 X
Date :1 May 2012
NTNU
Innovation and Creativity
10 µm
EHT = 10.00 kV
WD = 12 mm
Signal A = SE2
Mag = 1.50 K X
Date :1 May 2012
NTNU
Innovation and Creativity

(a) $E_x = -1000mV_{SCE}$, M = 500X (b) $E_x = -1000mV_{SCE}$, M = 1500X

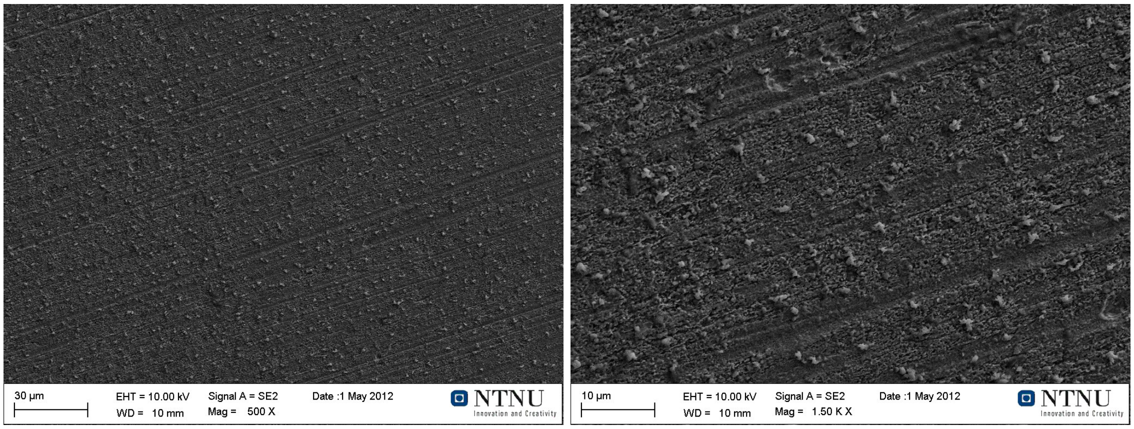
30 µm
EHT = 10.00 kV
WD = 10 mm
Signal A = SE2
Mag = 500 X
Date :1 May 2012
NTNU
Innovation and Creativity
10 µm
EHT = 10.00 kV
WD = 10 mm
Signal A = SE2
Mag = 1.50 K X
Date :1 May 2012
NTNU
Innovation and Creativity

(c) $E_x = -1200mV_{SCE}$, M = 500X (d) $E_x = -1200mV_{SCE}$, M = 1500X

Figure B.9: *SEM,* $i_{AC} = 500A/m^2$

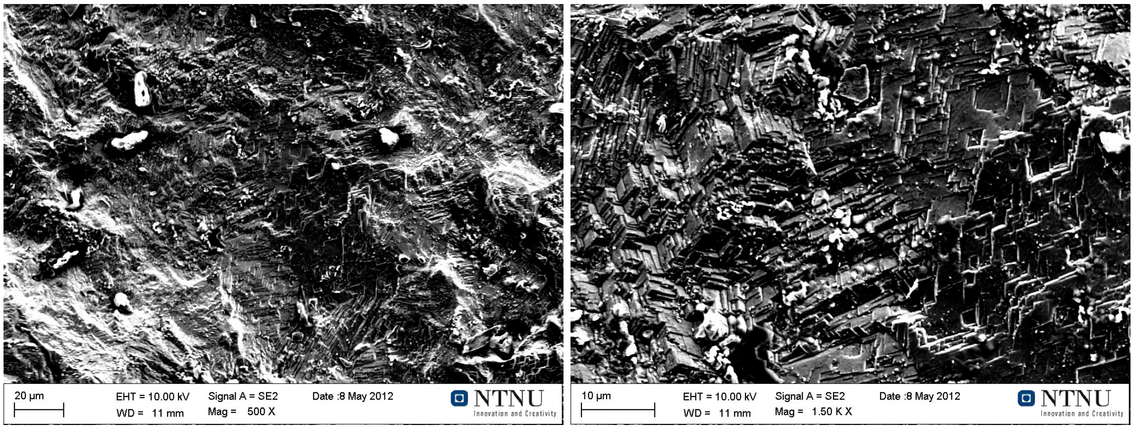
20 µm
EHT = 10.00 kV
WD = 11 mm
Signal A = SE2
Mag = 500 X
Date :8 May 2012
NTNU
Innovation and Creativity
10 µm
EHT = 10.00 kV
WD = 11 mm
Signal A = SE2
Mag = 1.50 K X
Date :8 May 2012
NTNU
Innovation and Creativity

(a) $E_x = -600mV_{SCE}$, M = 500X (b) $E_x = -600mV_{SCE}$, M = 1500X

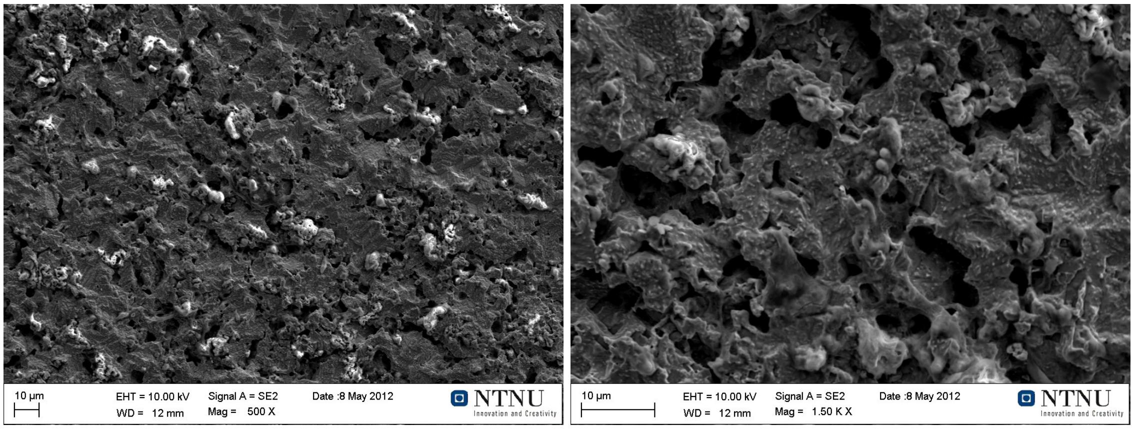
10 µm
EHT = 10.00 kV
WD = 12 mm
Signal A = SE2
Mag = 500 X
Date :8 May 2012
NTNU
Innovation and Creativity
10 µm
EHT = 10.00 kV
WD = 12 mm
Signal A = SE2
Mag = 1.50 K X
Date :8 May 2012
NTNU
Innovation and Creativity

(c) $E_x = -800mV_{SCE}$, M = 500X (d) $E_x = -800mV_{SCE}$, M = 1500X

Figure B.10: *SEM*, $i_{AC} = 700A/m^2$

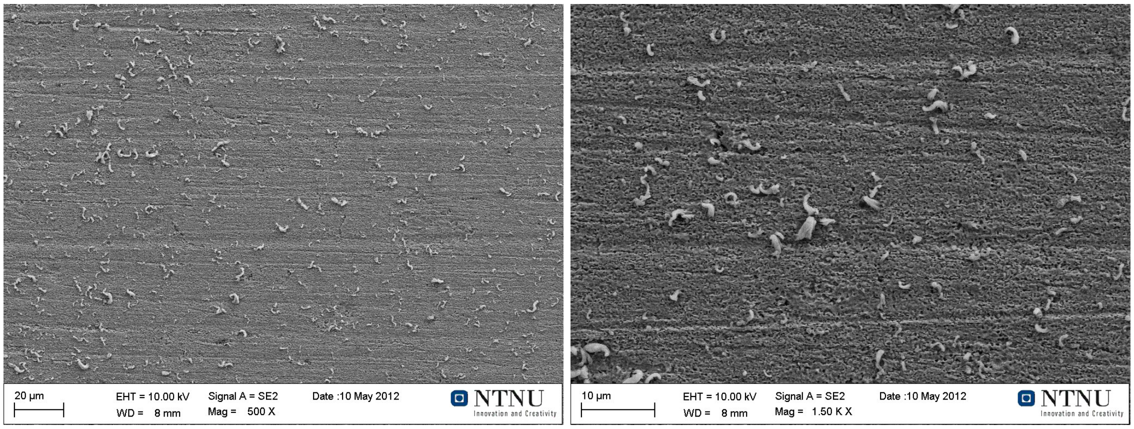
20 µm
EHT = 10.00 kV
WD = 8 mm
Signal A = SE2
Mag = 500 X
Date :10 May 2012
NTNU
Innovation and Creativity
10 µm
EHT = 10.00 kV
WD = 8 mm
Signal A = SE2
Mag = 1.50 K X
Date :10 May 2012
NTNU
Innovation and Creativity

(a) $E_x = -1000 mV_{SCE}$, M = 500X (b) $E_x = -1000 mV_{SCE}$, M = 1500X

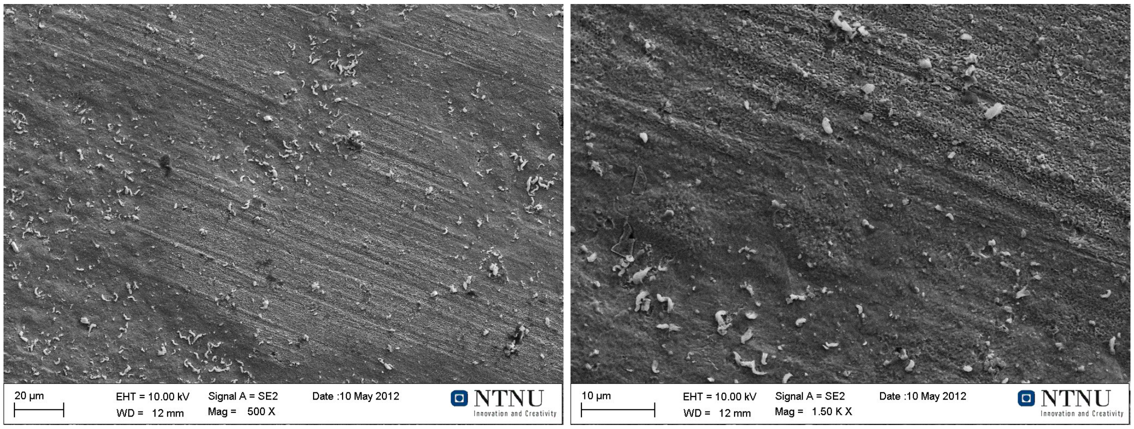
20 µm
EHT = 10.00 kV
WD = 12 mm
Signal A = SE2
Mag = 500 X
Date :10 May 2012
NTNU
Innovation and Creativity
10 µm
EHT = 10.00 kV
WD = 12 mm
Signal A = SE2
Mag = 1.50 K X
Date :10 May 2012
NTNU
Innovation and Creativity

(c) $E_x = -1200 mV_{SCE}$, M = 500X (d) $E_x = -1200 mV_{SCE}$, M = 1500X

Figure B.11: *SEM*, $i_{AC} = 700 A/m^2$

Appendix C

Sources of error

In comprehensive experimental studies like this one, some degree of error in measurements is to be expected. This section includes a summary of possible sources of error encountered throughout this study.

C.1 VariAC

The AC source in all experiments was a custom built VariAC. The preferred level of AC in each case was reached by measuring the voltage over a resistor by the use of a multimeter while tuning the VariAC. Once the correct voltage had been obtained, it was kept constant at this setting throughout the experiment. Some instability in applied AC density was however unavoidable due to a variety of factors, the most significant being local surface shrinkage of the samples due to corrosion (magnitude depending on experimental settings). Table C.1 sums up the deviations encountered in experiments with a stationary working electrode while table C.2 represents experiments with a rotating working electrode.

C.2 Electrolyte

As time passed during experiment, some of the electrolyte inevitably evaporated. Although only small quantities, this may have affected the level of salinity in the electrolyte. The effect of this was however assessed to be minor and its impact was neglected in the analysis. The electrolyte container was, as a preventive measure, marked with a pencil at the initial fill level and distilled water was added when deviations from this level became significant.

Table C.1: *Comparison of theoretical values of alternating voltage needed to achieve AC densities and the observed values. Some instability was encountered. The actual resistance in the inserted measuring resistor was 9.5 Ω.*

VariAC instability - stationary WE		
$i_{AC}[A/m^2]$	Required U_{AC}^{VariAC} [V]	Measured U_{AC}^{VariAC} [V]
100	0.62	0.58 - 0.69
250	1.55	1.50 - 1.61
500	3.10	3.02 - 3.20
700	3.80	3.57 - 3.94

Table C.2

VariAC instability - rotating WE			
$i_{AC}[A/m^2]$	Required U_{AC}^{VariAC} [V]	$U_{RMS}^{VariAC}[V/\sqrt{2}]$	Measured U_{AC}^{VariAC} [V]
100	0.29	0.20	0.26 - 0.32
250	0.71	0.50	0.68 - 0.74
500	1.43	1.01	1.39 - 1.46
700	2.00	1.41	1.96 - 2.04

C.3 Electrode position

The experimental setup used in the experiments with a stationary working electrode (figure 3.6) required repositioning of all electrodes (two counter electrodes and the working electrode), salt bridge and the rotating glass-rod prior to each experiment. Although they were carefully positioned in a predetermined manner, some variations may have occurred and is worth mentioning in this section. With regards to equipotential lines and the general distribution of charge this is a possible source of error.

Appendix D

Previous Work

Review of the results considered to be most important from the specialization project from 2011 by the author [2]. All experiments were performed in 3.5wt% NaCl electrolyte and the test material (working electrode) was carbon steel of identical composition as in this thesis.

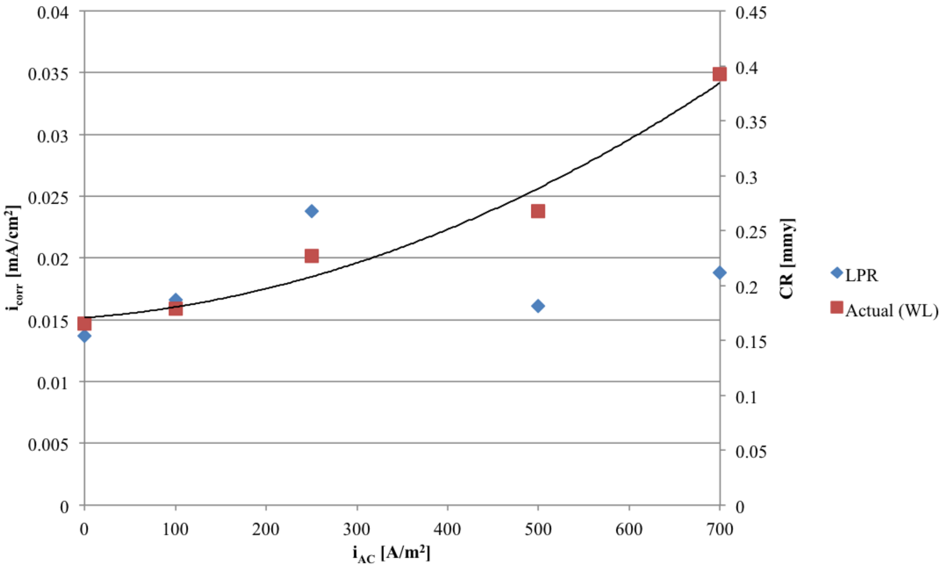

Figure D.1: *Measured mean values of i_{corr} and resulting CR at different applied AC densities. Red markers represent the actual values gained from weight loss measurements. Blue markers represent values from LPR measurements performed by the use of a manual Bank MP-81 potentiostat.*

Table D.1: *Results from the weight loss and LPR measurements (mean values).*

Results				
$i_{AC}[A/m^2]$	E_{corr} [mV]	R_p^{LPR} [Ω]	i_{corr}^{LPR} $[mA/cm^2]$	i_{corr}^{WL} $[mA/cm^2]$
0	-710	226	0.014	0.015
100	-768	186	0.017	0.016
250	-778	146	0.024	0.020
500	-789	208	0.016	0.024
700	-792	206	0.019	0.035

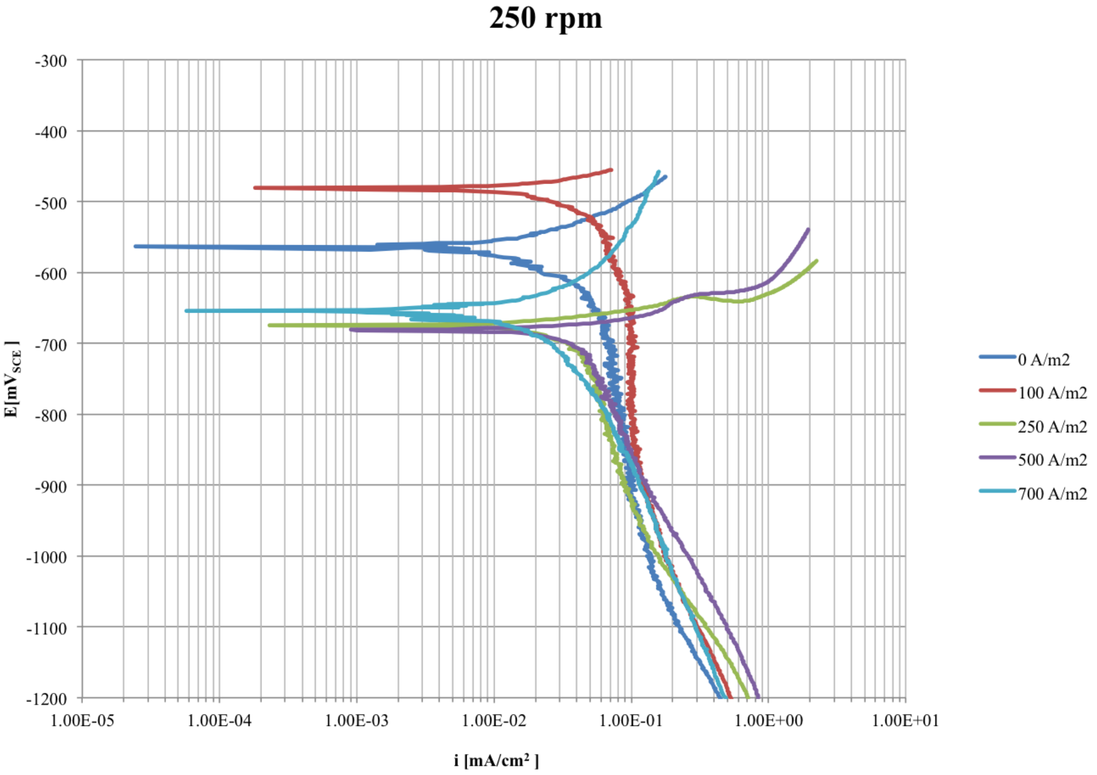

Figure D.2: *Polarization curves, 250 rpm*

Table D.2: *Curves were corrected for IR-drop in the electrolyte (R-value in table) and* i_{lim}. b_c *was corrected to only represent hydrogen reduction.*

Polarization data, 250 rpm				
$i_{AC}[A/m^2]$	E_{corr} [mV]	$R[\Omega]$	$i_{lim}[mA/cm^2]$	$b_c[mV/dec]$
0	-564	13	0.08	102
100	-484	10	0.1	128
250	-678	9	0.08	118
500	-685	9	-	187
700	-658	8	-	193

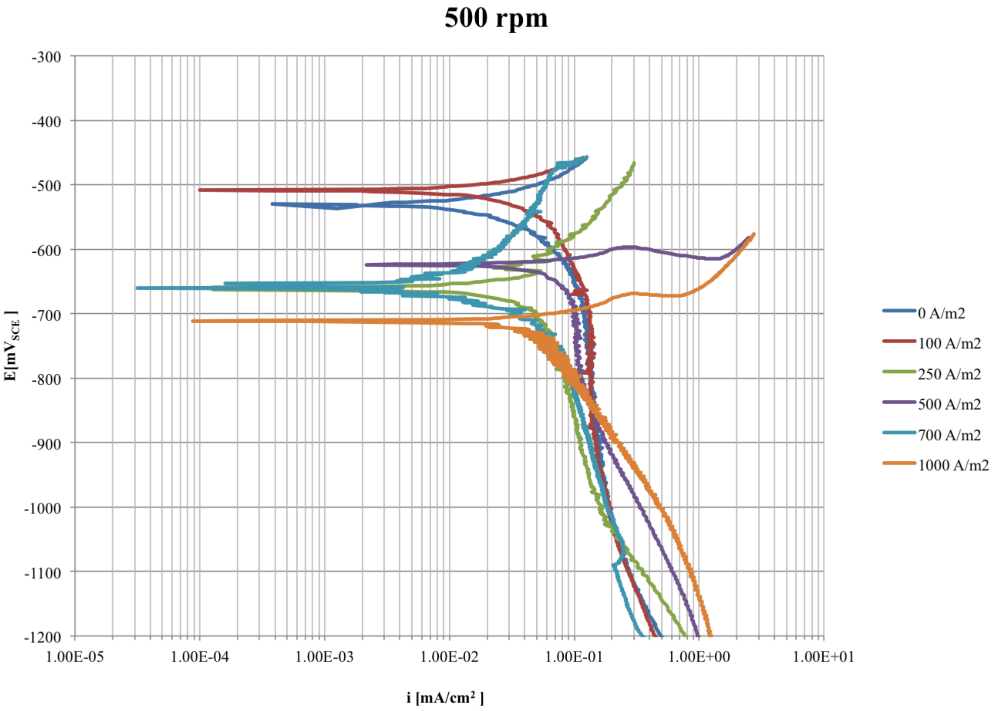

Figure D.3: *Polarization curves, 500 rpm*

Table D.3: *Curves were corrected for IR-drop in the electrolyte (R-value in table) and i_{lim}. b_c was corrected to only represent hydrogen reduction.*

Polarization data, 500 rpm				
$i_{AC}[A/m^2]$	E_{corr} [mV]	$R[\Omega]$	$i_{lim}[mA/cm^2]$	$b_c[mV/dec]$
0	–532	12	0.12	107
100	-514	10	0.12	108
250	-667	9	0.10	100
500	-627	8	0.10	169
700	-665	9	-	148
1000	-715	7	-	192

D.1 Correction for IR-drop - polarization curves

The polarization curves gathered through potentiodynamic scans needed to be corrected for IR-drop in the electrolyte. This conclusion is drawn by looking at the anodic and cathodic slopes. If they are not linear, corrections need to be made. The corrected value is given in equation D.1. All parameters are known except the resistance, R. The value of R is roughly adjusted using engineering judgement until the curves appear linear.

$$E_{corrected} = E_{measured} - IR \tag{D.1}$$

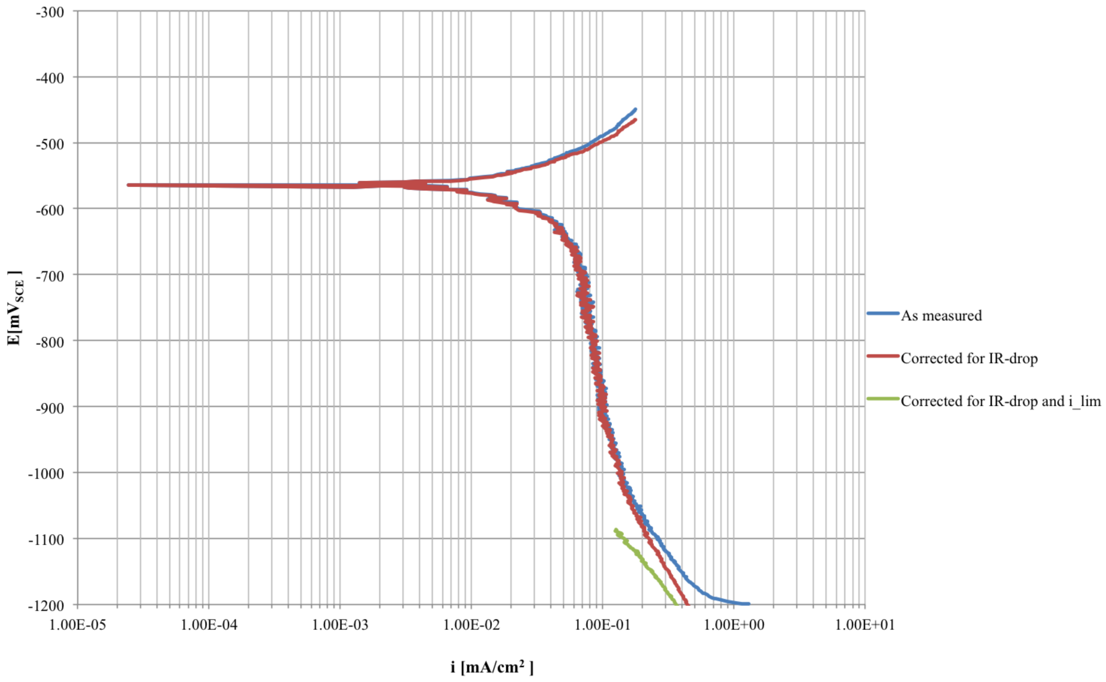

Figure D.4: *Correction for IR-drop and* i_{lim}.